

Electromagnetic Field Modeling for the Charging Pads of a 50 kW IPT System and Mechanical De- sign for the Pad's Casings

MSc. Thesis

C.F. de la Garza
Cuevas

Electromagnetic Field Modeling for the Charging Pads of a 50 kW IPT System and Mechanical Design for the Pad's Casings

MSc. Thesis

by

C.F. de la Garza Cuevas

to obtain the degree of Master of Science
at the Delft University of Technology,
to be defended publicly on Tuesday August 23, 2022 at 10:00 AM.

Student number: 5245133
Project duration: November 29, 2021 – August 23, 2022
Thesis committee: Prof. dr. P. Bauer, TU Delft
Prof. dr. A. Smets, TU Delft
Dr. J. Dong, TU Delft, supervisor
Dr. ir. M. Ghaffarian, TU Delft, supervisor

An electronic version of this thesis is available at <http://repository.tudelft.nl/>.

Acknowledgements

This work is dedicated to my parents, Roberto and Carmen, whose support was especially important during this stage of my life. Being away from home was not easy at some points, but you still managed to make me feel close to you. Thank you for the comforting words, mainly during the difficult times I faced, I found in your voice a safe place to calm my mind and keep moving forward.

To my brother Roberto, who, as always, played the role of life mentor during these two years in The Netherlands, your advice was the reason I had a smooth integration into this country and its lifestyle, but, above all, the best was to be together again after such a long time, I will always be thankful for that.

To Calvin, who daily supervised my work, and who very patiently solved all my doubts and lead me through the correct path. Know that I always felt supported by you and that I hope you enjoyed this process as much as I did.

To my supervisors, Prof. Jianning and Prof. Mohamad, who also supervised my work, and who allow me to work at the DCE&S research group. I couldn't have done this work without your guidance and experience. Also to Prof. Bauer and Prof. Smets, who agreed to be part of my thesis committee.

To all my friends, especially to Fabian, Mohool, Thor and Ashwin, who shared with me amazing moments, and also the most stressful periods of this journey. I was very lucky to meet you all, and I am very excited to think about all the adventures that await for us in the future.

To Ghislaine, I was very fortunate to cross paths with you. Cycling to your house and resting in your arms was the best reward after a long day of work. Thanks a lot for being so sweet.

To Harry Olsthoorn, who supported me and Calvin on the lab work from this thesis. Your experience and knowledge made our work possible.

*C.F. de la Garza Cuevas
Delft, August 2022*

Abstract

Wireless charging technology, in particular, Inductive Power Transfer (IPT), has been evolving during the last decades, and it's starting to become attractive for electric mobility applications. The working principle of the IPT technology is based on two coils separated by an air gap and magnetically coupled together; since the medium to transfer the energy is the air between the coils, the magnetic circuit of this system becomes remarkably important, as the magnetic flux need to be constrained as much as possible for the sake of securing the magnetic linkage between the coils. In this thesis, the design process of the casing of the coils is presented, such casing will ensure that the coils are always kept fixed according to their design.

From this point, the first goal of this thesis arises: Design an accurate and modular casing for the coils of a 50 kW IPT system that will fix such elements in the correct position, and which will allow for easy changes/upgrades in the coil if required. The design process of such casing was to first do the CAD model of the coils, and then do the CAD model of the casing, by considering the following criteria: accurate dimensions, easy and fast to manufacture and assemble, modular-designed, light, adequately cooled, and robust. The result of such design was a casing that was actually manufactured and assembled, and that is currently being used to test a 50 kW IPT prototype system.

Besides procuring an efficient coil design for the IPT systems, it's important to understand the dynamic behavior of the IPT electric system. One of the elements that could potentially influence the electric behavior of such system is known as *parasitic capacitance*. From here, the second objective of this thesis arises: Derive the parasitic capacitance of the coils in order to perform a better circuit modeling and to predict a possible over-voltage across such capacitance.

The methodology to derive the parasitic capacitance of the coils was first to perform an electromagnetic fields FEM simulation on the coils in order to obtain a set of parameters such as the coils impedance, resonance frequency and inductance. With these parameters and a set of equations, it was possible then to derive the parasitic capacitance of each coil. Finally, with this information, it was possible to build a (virtual) equivalent circuit of the IPT system and evaluate the voltage across the parasitic capacitance. It was concluded from this thesis that the parasitic capacitance at the standard operating frequency (85 kHz) does not represent a risk of over-voltage, but as the frequency goes close to the resonance frequency (1.46 MHz), the electric field across the capacitor could reach values up to 14 kV/mm.

C.F. de la Garza Cuevas
Delft, August 2022

Preface

This thesis about "Electromagnetic Field Modeling for the Charging Pads of a 50 kW IPT System and Mechanical Design for the Pad's Casings" has been written to obtain the MSc degree in Sustainable Energy Technology at the Delft University of Technology. The work was performed at the DC Systems, Energy Conversion and Storage (DCE&S) research group from TU Delft.

This thesis has been written with the goal to contribute to the current efforts to promote the electric mobility as a mean of transportation, especially in the public transportation sector. This report has been written for anyone who seeks to have a better understanding of a Finite Element Method (FEM) analysis applied to a wireless charging system for electric vehicles (EVs), and also for anyone who is interested in the 3D design process of the casing for prototype wireless charging systems for EVs.

Readers that are interested in the design of a casing for the charging pads of an EV wireless charger prototype can refer to the chapter 3, while readers who are interested in electromagnetic FEM simulations applied to the wireless charging systems for EVs can refer to chapter 4.

*C.F. de la Garza Cuevas
Delft, August 2022*

Contents

Acknowledgements	iii
Abstract	v
Preface	vii
List of figures	xiii
List of tables	xv
Acronyms	xvii
1 Introduction	1
2 Overview of the IPT system	3
2.1 Working principle of Inductive Power Transfer (IPT)	3
2.2 Overall IPT system	3
2.3 Uncompensated IPT system	4
2.4 Compensated IPT system	6
2.5 Types of IPT systems	8
2.6 Main elements of the IPT charging pads	11
2.7 Equivalent circuit of the IPT system	12
3 IPT Pads Casing Desing	17
3.1 IPT pads dimensions and parameters.	17
3.2 IPT pads casing requirements	19
3.3 IPT pads design process.	19
3.3.1 CAD model of the active elements.	19
3.3.2 Cooling system assessment	25
3.3.3 CAD design of the casing	28
3.4 IPT charging pads casings assembly	32
4 COMSOL FEM Simulation	37
4.1 Parasitic capacitance fundamentals	37
4.2 Methodology for parasitic capacitance evaluation	41
4.3 COMSOL model setup	42
4.4 Module, interface and features selection for the COMSOL FEM simulation.	46
4.5 COMSOL model validation.	48
4.6 Electromagnetic Fields FEM simulation	57
4.7 Parasitic capacitance derivation	59
4.8 Voltage across parasitic capacitance and electric field strength evaluation	60
5 Conclusions & Future Work	67
Bibliography	72

List of Figures

2.1 Overall IPT system for battery charging [1, p. 12]	4
2.2 IPT coils basic representation [2, p. 293]	5
2.3 IPT coils simplified equivalent circuit [2, p. 293]	5
2.4 IPT Norton equivalent circuit [2, p. 294]	5
2.5 Example of layout for winding, ferrite cores and metal shields (Front view)	6
2.6 (a) Compensation capacitance in parallel, (b) Compensation capacitance in series [2, p. 296]	7
2.7 Compensation topologies [3, p. 86]	8
2.8 Coil topologies [4, p. 4]	10
2.9 (a) Tightly coupled system and (b) Loosely coupled system	10
2.10 Main elements of the IPT charging pads	11
2.11 Example of ferrite cores arrangement (Top view)	12
2.12 (a) IPT equivalent circuit, with transformation ratio $n=1$. (b) For general transformation ratio n . (c) For transformation ratio $n = k\sqrt{L_1/L_2}$, where leakage inductance is referred to the primary side [5, p. 22]	13
2.13 Series-series compensated IPT system [6, p. 367]	14
2.14 Series-series compensated IPT system [6, p. 368]	14
3.1 2D sketch of the 50 kW IPT primary coil	20
3.2 3D sketch of the 50 kW IPT primary coil	21
3.3 CAD model of the 50 kW IPT primary coil	21
3.4 Ferrite plate for the cores of the primary pad	22
3.5 Ferrite plates' layout for the cores of the primary pad	22
3.6 Ferrite core for the primary pad	23
3.7 Layout for coil and ferrite cores of primary 50 kW IPT pad	23
3.8 Metal shield for the primary pad	24
3.9 Virtual assembly of the active elements from the 50 kW IPT primary pad	24
3.10 Side view of active elements virtual assembly	25
3.11 IPT charging pad with cooling system from ETH Prototype [7, p.129]	26
3.12 Fan for primary IPT pad [8]	26
3.13 Fan for secondary IPT pad [9]	26
3.14 Primary IPT charging pad active elements with fans	28
3.15 Base and side walls of the primary IPT pad casing with cooling fans and metal shield	28
3.16 Primary IPT pad casing with cores supports	29
3.17 Primary IPT pad casing with cores and cores supports	29
3.18 Lid for the primary IPT pad casing with coil retainers (shown in red)	30
3.19 Lid for the primary IPT pad casing with coil retainers and coil	30
3.20 Final 3D design of the casing for the 50 kW primary IPT pad	31
3.21 Final 3D design of the casing for the 50 kW secondary IPT pad	31
3.22 Drawing example of the parts to be laser-cut at <i>Laserbeest</i>	32
3.23 Base and side walls assembly of the primary IPT pad casing, including fans	33
3.24 Base and side walls assembly of the primary IPT pad casing, including the core retainers	33
3.25 Base and side walls assembly of the primary IPT pad casing, including ferrite cores	34
3.26 Base and side walls assembly of the primary IPT pad casing, including coil retainers	34
3.27 Lid assembly for the primary IPT pad casing, including coil	35
3.28 Final assembly of the casing for the 50 kW IPT primary pad	35
4.1 Two conductors that are separated in space will balance each other with equal but opposite charges when brought up to some arbitrary potential, forming a capacitor [10]	38

4.2	Three turn inductor with parasitic capacitances between turns [11]	39
4.3	Distributed circuit model of an inductor with three turns [11]	39
4.4	(a) Equivalent circuit of a coil without parasitic capacitance. (b) Equivalent circuit of a coil with parasitic capacitance	40
4.5	Inductor model showing parallel R and L equivalents [12]	40
4.6	(a) Pair of Litz wires (front view). (b) Pair of Litz wires (top view)	42
4.7	COMSOL setup (geometry) for a 20 kW IPT charging pad	43
4.8	Primary coil meshing for the 20 kW COMSOL setup	44
4.9	Cores meshing for the 20 kW COMSOL setup	45
4.10	Metal shield meshing for the 20 kW COMSOL setup	45
4.11	Surround air meshing for the 20 kW COMSOL setup	46
4.12	Varying approaches over frequency for volumetric coils [13]	47
4.13	Lumped port graphic representation [14, p. 102]	48
4.14	Magnetic flux in simulation with Infine Elements surrounding	49
4.15	Magnetic flux in simulation with magnetically insulated sphere	49
4.16	Magnetic flux considering ferrite cores (without metal shielding)	50
4.17	Magnetic flux with metal shielding at resonance frequency (without cores)	50
4.18	Impedance bode plot for the 20 kW primary IPT pad	51
4.19	Coil inductance for the 20 kW primary IPT pad	52
4.20	Equivalent circuit of the 20 kW primary IPT coil with parameters (R_{AC} is taken at the resonance frequency).	53
4.21	Impedance bode plot for the 20 kW IPT system using equivalent circuit equations	53
4.22	Comparison between the FEM simulation bode plot and the bode plot obtained from equation Equation 4.5	54
4.23	Impedance bode plots for the 20 kW primary IPT pad measured by the VNA	54
4.24	20 kW primary IPT pad inductance measured by the VNA	55
4.25	20 kW primary IPT pad inductance measured by the VNA (Zoom-in)	55
4.26	Comparison of the impedance bode plots obtained from the FEM simulation and the VNA measurements	56
4.27	COMSOL model setup for the 50 kW IPT charging pads	57
4.28	COMSOL model setup for the 50 kW IPT charging pads (including the mesh)	57
4.29	Impedance bode plot for the 50 kW IPT primary pad obtained from the FEM simulation	58
4.30	Impedance bode plot for the 50 kW IPT secondary pad obtained from the FEM simulation	58
4.31	(a) Equivalent circuit of the 50 kW IPT primary coil. (b) Equivalent circuit of the 50 kW IPT secondary coil	59
4.32	Comparison between the FEM simulation bode plot and the bode plot obtained from equation Equation 4.5 for the primary 50 kW IPT coil	60
4.33	Comparison between the FEM simulation bode plot and the bode plot obtained from equation Equation 4.5 for the secondary 50 kW IPT coil	60
4.34	Circuit model built at <i>GeckoCircuits</i> for the overall 50 kW IPT system	61
4.35	Voltage across the coil terminals (without parasitic capacitance) for the 50 kW IPT system	62
4.36	Voltage across the coil terminals (with parasitic capacitance) for the 50 kW IPT system	62
4.37	Electric and magnetic energy comparison from the primary coil of the 50 kW IPT system, evaluated at 500 kHz	63
4.38	Electric field visualization between the coil and the terminal of the 50 kW IPT primary pad, evaluated at 500 kHz	63
4.39	Electric field [V/m] visualization in the plane between the coil and the terminal of the 50 kW IPT primary pad, evaluated at the resonance frequency (1.45 MHz)	64
4.40	Electric field visualization between the coil and the cores of the 50 kW IPT primary pad, evaluated at 500 kHz	64
4.41	Electric field visualization between the coil and the cores of the 50 kW IPT primary pad (transversal view)	65
5.1	Final design of the casing for the primary pad	67
5.2	Final design of the casing for the secondary pad	67

5.3	(a) Equivalent circuit of the 50 kW IPT primary coil. (b) Equivalent circuit of the 50 kW IPT secondary coil	68
5.4	Electric field visualization in the terminals of the 50 kW IPT primary pad, evaluated at 500 kHz	69
5.5	Electric field visualization between the coil and the cores of the 50 kW IPT primary pad, evaluated at 500 kHz	69

List of Tables

3.1	Optimization variables of a multi-objective optimization study for the charging pads of a 50 kW IPT system	18
3.2	Results of a multi-objective optimization study for the charging pads of a 50 kW IPT system	18
3.3	Technical specifications for the IPT fans	27
3.4	Typical values of the convective heat transfer coefficient (h) [15, p.2]	27
4.1	Results of a multi-objective optimization study for the charging pads of a 20 kW IPT system [19]	43
4.2	Electric and magnetic properties for the 20 kW setup materials	44
4.3	Electric and magnetic parameters for simulation with and without Infinite Elements surrounding	51
4.4	Results for the 20kW IPT primary coil FEM simulation taken at the resonance frequency	52
4.5	Comparisson between FEM simulation results and VNA measurements for the 20 kW IPT primary pad	56
4.6	Derived values for the primary and secondary coils taken at the resonance frequency .	59
4.7	Main parameters for 50 kW overall IPT circuit model	61
5.1	Derived values for the primary and secondary coils	68

Acronyms

CAD Computer-aided Design. 19

DCE&S DC Systems, Energy Conversion and Storage. vii, 1, 17, 60

ESP Electrical Sustainable Power. 32

EV Electric Vehicle. 1

FEM Finite Element Method. 20, 42

IE Infinite Elements. 48

IPT Inductive Power Transfer. ix, xi, xv, 1, 3–9, 11–13, 15, 17, 19, 25–28

kHz Kilohertz. 5

MF Magnetic Fields. 46

MOO Multi-objective Optimization. 1, 17

OC Open Circuit. 5

PE Power Electronics. 11

RF Radio Frequency. 46

SC Short Circuit. 5

SRF Self Resonance Frequency. 40

VA Volt-ampere. 5

VNA Vector Network Analyzer. 41, 54

WPT Wireless Power Transfer. 1, 3, 9

Introduction

Inductive Power Transfer (IPT) is a technology that has been evolving for around 30 years into an industry that currently worths more than one billion dollars [16]. The applications of this technology can vary within a broad range of options, going from power distribution in automation systems to dynamic charging in electric vehicles (EVs). The challenges encountered by IPT systems are quite complex, nevertheless, they offer a potential that no other technology could meet [16]. IPT systems are becoming remarkably important in the electric transportation industry, as a mean to achieve a safe "hands-free" and efficient charging mode for EVs.

The working principle of the IPT technology is based on two magnetically coupled coils: the transmitter coils is excited by an alternating current, which will create an alternating magnetic field; a portion of this magnetic field links the secondary coil and induces a voltage in it, as stated by Faraday's and Ampere's law; this voltage can be used to power an electric load connected to it [17]. This technology is considered a type of Wireless Power Transfer (WPT) technology since the two coils are not physically in contact. It's important to mention that the reluctance of the magnetic circuit between the coils is high, unlike conventional transformers, where the reluctance is substantially low due to the highly permeable magnetic core. If the reluctance of the mutual magnetic flux path is compared to the reluctance of the leakage flux path of the coils, we will find out that the first one is higher than the second one, meaning that the leakage flux can be considerably high, leading to a *loose* coupled coil.

Engineers have formulated different strategies to overcome the low coupling of the coils, one of these solutions is related to the design of an efficient magnetic circuit. In order to achieve this, a multi-objective optimization MOO was performed by engineers from the DC Systems, Energy Conversion and Storage (DCE&S) research group of TU Delft for the 50 kW IPT system that will be studied in this thesis. The results from the MOO study provide the optimal dimensions and shape of the coils (also known as charging pads) to obtain the best magnetic circuit with high power transfer efficiency and high power density. It is for this reason that a casing that holds the coils within the required dimensions is required. Besides this, the charging pads to be built are prone to future changes and upgrades, for this reason, the active elements of the pads (coils, ferrite cores and metal shields) need to be somehow accessible, this can be achieved by designing the casing in a modular way. Below, the research question and motivations for this task can be seen:

Research question 1

Why is it required to design an accurate and modular casing for the IPT charging pads?

Motivation:

1. If the dimensions of the active elements of the IPT charging pads (coils, ferrite cores and metal shields) to be built are as close as possible to the dimensions obtained from a multi-objective optimization (MOO) study, then the optimization objectives (criterion) outcome will be as expected.

2. A casing for the IPT charging pads will serve as a fixture to keep all the active elements of the pads in place.
3. A modular design of the casing for the IPT charging pads will allow us to: save time, money, and weight; and to easily implement future changes or upgrades in the pads.

The methodology to achieve a functional casing design was first to do the 3D design of the coils, then, with these models as reference, do the 3D designing of the casings, considering the following criteria: accurately dimensioned, easy and fast to manufacture and assemble, modular-designed, light, air-cooled, and robust. Besides the magnetic circuit aspect of the system, it is also extremely important to understand the electromagnetic nature of the coils. One of the factors that influence the behavior of the IPT electric system is known as parasitic capacitance, which is an inevitable and generally undesirable capacitance that occurs in electric circuits, and which is capable to change the self-resonant frequency of the coils, their impedance, quality factor, and efficiency; it's for this reason that is important to perform an assessment to know the magnitude of the parasitic capacitance in the system. Apart from this, by knowing the parasitic capacitance, it's possible to build an accurate virtual electric circuit of the IPT system, which will allow for a realistic circuit analysis. The results from such analysis could also anticipate a possible over-voltage across the parasitic capacitance in the system. Below, the research question and motivations for this task can be seen:

Research question 2

How does the parasitic capacitance affects the dynamic behavior of the IPT electric system, and what are the risks associated with the parasitic capacitance?

Motivation:

1. Knowing the parasitic capacitance of the IPT coils will allow us to understand and replicate the dynamic behavior of the system, for better circuit modeling.
2. Knowing the parasitic capacitance will provide information regarding a potential over-voltage between the coil terminals, the coil turns, and the coil and the cores/shield.
3. The developed methodology to evaluate the parasitic capacitance can also be used to determine the equivalent circuit of the charging pads, which can be used to test the system under different conditions.

The methodology used to derive the value of the parasitic capacitance and its effects can be reduced in the following steps: doing an electromagnetic fields FEM simulation of the IPT system, this will provide the main electric and magnetic parameters of the system, which can be used to derive the value of the parasitic capacitance with the aid of some equations. These values can then be introduced as inputs into a (virtual) equivalent circuit, which will provide important data such as the voltage across the parasitic capacitors. This information will finally be used to evaluate potential risks such as over-voltage at some regions of the coils. In chapter 1, a brief introduction to the fundamentals of IPT technology will be provided. Then, the IPT casings design process will be addressed in chapter 3. The parasitic capacitance evaluation will be described in chapter 4, and finally, the discussion and conclusions will be presented in chapter 5.

2

Overview of the IPT system

In this chapter, the fundamentals of Inductive Power Transfer (IPT) will be described.

2.1. Working principle of Inductive Power Transfer (IPT)

The underlying working principle of the IPT technology is based on two (or more) magnetically coupled coils that operate at resonance for an efficient power transfer: it is said that coils are magnetically coupled when the magnetic field created by a current in the transmitter coil induces a voltage in the receiver coil, as stated by Faraday's and Ampere's law; this voltage can be used to power an electric appliance (or load) connected to the receiver coil [17]. It is important to mention that the IPT process is merely 'wireless', meaning that the two coils are not physically in contact, and thus, the power transfer is done through the air gap in between them; this is why the IPT systems are considered to be a type of Wireless Power Transfer (WPT) technology. Since the medium to transfer the energy is air, the power transfer is not affected by chemicals, dirt or weather. Besides this, wireless charging eliminates the need for exposed contacts and wiring, and thus, it possesses a great advantage for some special environments such as the mining industry, clean factories, and underwater operations.

As mentioned in chapter 1, the leakage inductance in IPT systems can be considerably high, and so, the power transfer levels are limited. One way engineers have formulated to overcome this concern is with the so-called *compensation capacitance*; this concept will be the one implemented for the IPT system to be studied in this thesis, and its working principle will be further explained in section 2.3 and section 2.4. There are also a series of standards, such as the SAE J2954, ISO 19363, and IEC 61980-1, which address the main regulations used for WPT in EVs that intend to warrant both magnetic and electric interoperability between the coils fabricated by different manufacturers and with different topologies. To achieve this, for instance, SAE J2954 established a nominal operating frequency of 85 kHz for the IPT charging systems in EVs [18].

2.2. Overall IPT system

The overall equivalent circuit of an IPT system for battery charging can be seen in Figure 2.1. From this diagram, the power transfer efficiency from the transmitter side DC-link ($U_{1,dc}$) to the receiver side DC-link ($U_{2,dc}$) can be calculated. The first power conversion phase occurs at the DC-AC high-frequency inverter, with efficiency η_{inv} ; the second phase occurs at the AC-AC magnetic coupling, with η_{mag} efficiency; and the third phase occurs at the AC-DC rectifier with η_{rec} efficiency [19]. The total power transmission efficiency (η_T) can then be expressed as in Equation 2.1.

$$\eta_T = \eta_{inv}\eta_{mag}\eta_{rec} \quad (2.1)$$

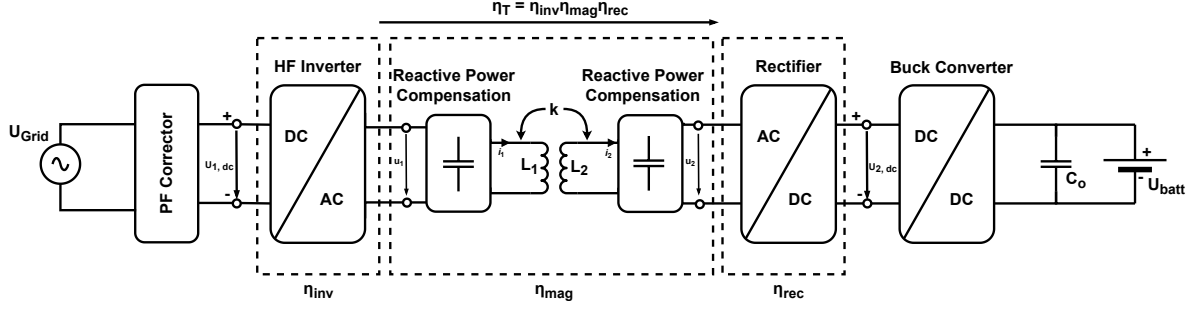


Figure 2.1: Overall IPT system for battery charging [1, p. 12]

If we assume that the current i_1 and the voltage u_1 are in phase, and i_2 and u_2 are also in phase (due to the reactive power compensation shown in Figure 2.1), the AC voltages u_1 and u_2 at the terminals of the coils from Figure 2.1 can be expressed as in Equation 2.2 and Equation 2.3. The inverters used for IPT systems are usually operated using a phase shift modulation scheme, thus, the fundamental voltage at the inverter output can then also be expressed as in Equation 2.4, where α is the phase shift between the inverter legs, and $U_{1,dc}$ is the primary side DC voltage. The same can be applied to the secondary side, resulting in Equation 2.5 [20].

$$u_1 = -j\omega M i_2 \quad (2.2)$$

$$u_2 = -j\omega M i_1 \quad (2.3)$$

$$u_1 = \frac{2\sqrt{2}}{\pi} U_{1,dc} \sin\left(\frac{\alpha}{2}\right) \quad (2.4)$$

$$u_2 = j \frac{2\sqrt{2}}{\pi} U_{2,dc} \sin\left(\frac{\beta}{2}\right) \quad (2.5)$$

The power can be controlled by the variation of the primary and secondary side voltages ($U_{1,dc}$ and $U_{2,dc}$) by using equation Equation 2.6, where P_{out} represents the power to be withdrawn by the battery, ω the angular frequency of the system and M the mutual inductance of the coils. The duty cycles (or α and β) of the voltage waveforms can be also varied to control the amount of power transferred [2], while the DC voltage at the receiver side ($U_{2,dc}$) can be controlled by a DC-DC converter placed before the battery [1].

$$P_{out} = \Re\{u_2 i_2^*\} = \frac{8}{\pi^2} \frac{U_{1,dc} U_{2,dc}}{\omega M} \sin\left(\frac{\alpha}{2}\right) \sin\left(\frac{\beta}{2}\right) \quad (2.6)$$

2.3. Uncompensated IPT system

The basic representation of the coils of an IPT system is shown in Figure 2.2, while the simplified equivalent circuit of this system is shown in Figure 2.3. As mentioned in section 2.1, and in accordance to Ampere's law, the current in the primary coil (I_P) creates a magnetic field around the coil. A portion of the magnetic flux that links both the primary and secondary coils is denoted as ϕ_M in Figure 2.2, while the portion of magnetic flux that only links one of the coils, is denoted as ϕ_{LKi} in Figure 2.2, where i can be either P or S , depending on if it is in the primary or secondary coil respectively. According to Faraday's law, the alternating magnetic field produced by I_P that links the secondary coil induces a voltage in it, which causes the alternating current I_S to flow if the coil is connected, for instance, to a resistive load R_L [2]. In Figure 2.3, the leakage inductances are represented by the self-inductances L_P and L_S , while M is the mutual inductance. The induced voltages at the windings are represented by V_{PR} and V_S , and are derived as follows:

$$V_{PR} = -j\omega MI_S \quad (2.7)$$

$$V_S = j\omega MI_P \quad (2.8)$$

Where ω is the operation angular frequency in [rad/s]. The receiver side of the circuit can also be represented by the Norton equivalent circuit [2], shown in Figure 2.4. If the open circuit (OC) induced voltage in the secondary coil by I_P is expressed as in Equation 2.9, then, the short circuit (SC) current I_{SC} , which depends on the secondary coil open circuit (OC) voltage and impedance, can be expressed as in Equation 2.10.

$$V_{OC} = V_{S,max} = j\omega MI_P \quad (2.9)$$

$$I_{SC} = \frac{V_{OC}}{j\omega L_S} = \frac{j\omega MI_P}{j\omega L_S} = \frac{MI_P}{L_S} \quad (2.10)$$

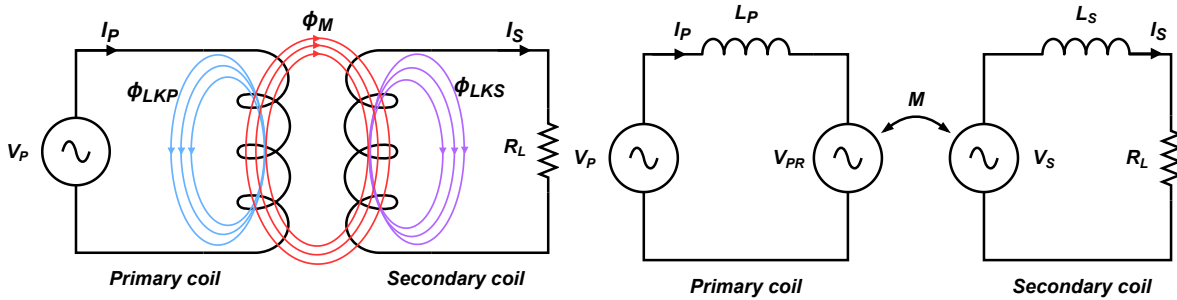


Figure 2.2: IPT coils basic representation [2, p. 293]

Figure 2.3: IPT coils simplified equivalent circuit [2, p. 293]

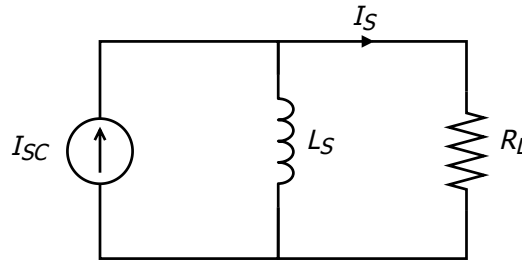


Figure 2.4: IPT Norton equivalent circuit [2, p. 294]

If we have a resistive load (R_L) across the terminals of the receiver side, then the rated VA (Volt-ampere or Apparent power) value of the secondary side can be expressed as in Equation 2.11 [2], where S_u stands for the uncompensated (without compensation capacitance) apparent power. Then, the maximum power that can be drawn by the load ($P_{u,max}$), still in the uncompensated condition, is $S_u/2$ [16], shown in Equation 2.12.

$$S_u = |V_{OC} I_{SC}| = \frac{\omega M^2 I_P^2}{L_S} \quad (2.11)$$

$$P_{u,max} = \frac{S_u}{2} = \frac{1}{2} \frac{\omega M^2 I_P^2}{L_S} \quad (2.12)$$

The addition of compensation capacitors could be used to counteract the inductive reactance of the system, and thus, an increase in the power transfer could be reached. The amount of compensation capacitance is calculated in a way that the system resonates near the standardized operation frequency for IPT in EV applications, which is 85 kHz [21]. These compensation capacitors can be either applied

in series or parallel to the winding terminals, more details about the compensation topologies will be presented in section 2.4. It can be seen from Equation 2.12 that, if ω , I_p or the M^2/L_S ratio are increased, then the power transfer can be optimized [2]. Nevertheless, modifying the value of any of these parameters implies a trade-off in the system, for instance, if the system is operated at higher frequencies, the switching losses will increase, and, as a consequence, the operating temperature; this can be counteracted by the use of proper thermal insulation and heat dissipation techniques, but the overall cost of the system will increase [2]. A high operation frequency can also increase the winding losses due to skin and proximity effect, which could be mitigated with the use of *Litz wire*¹, at the expense of increasing the overall cost as well. Increasing I_p implies an increase in the temperature of the coils due to joule effect, so the current becomes constrained by the temperature ratings of the wire's insulation [2]. Increasing the M^2/L_S ratio entails increasing the mutual flux between the two coils and reducing the leakage fluxes, nevertheless, accomplishing this is not an easy task: first, due to the layout and geometry of the coils (one on top of the other), the magnetic flux created by the primary coil needs to be increased in the upward direction, and reduced in any other direction [2]; in order to achieve this, ferrite cores are placed below and on top of the primary and secondary coils respectively, as shown in Figure 2.5, in this way, the magnetic coupling is enhanced; nevertheless, if the distance between the coils increases, then the reactive power drawn from the supply also needs to increase in order to make sure that the flux linkage to the secondary coil remains constant. Another issue is related to the potential misalignment between the two coils, which can even lead to zero power transfer when there is no flux linkage to the receiver coil, thus, tolerance to misalignment (controlled mainly by the shape of the coils) is very important for the system design [2]. Besides optimizing the arrangement of the cores and the shape of the coils, it is also important to design a proper compensation circuit to maximize the power transfer. In the next section this topic will be addressed.

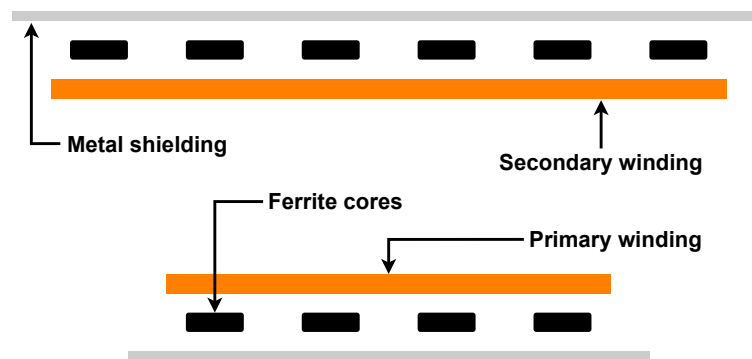


Figure 2.5: Example of layout for winding, ferrite cores and metal shields (Front view)

2.4. Compensated IPT system

Since we are dealing with coils with low magnetic coupling, the amount of energy stored in the uncoupled magnetic flux will cause the reactive power to be always considerably larger than the active power, which will result in a poor power transfer and efficiency, this, of course, in the uncompensated scenario. As can be seen in Equation 2.12, the power transfer can be increased by raising the M^2/L_S ratio, nevertheless, this option is often complex due to the large air gap that exists between the coils. Another option to increase the power transfer is by compensating the inductive reactance with the addition of capacitive reactance in the system. The compensation can be either added in parallel or in series to the coil circuit, as can be seen in Figure 2.6. Figure 2.6(a) shows the IPT coils with parallel compensation, while Figure 2.6(b) shows the series compensation. In these circuits, C_P and C_S are chosen to resonate with L_P and L_S respectively at the standardized operating frequency. If, for instance, the analysis is focused on the output side (secondary side) of the parallel compensation, a voltage rise by a factor of Q across the parallel circuits develops when operating at the resonance frequency [2], giving:

¹*Litz wire* is a type of conductor made up of multiple individually insulated strands twisted or woven together, whose main purpose is to reduce the losses in the windings created by the skin-effect and proximity-effect [22]

$$V_S = j\omega_0 M I_P Q \quad (2.13)$$

Where Q in this case is the loaded quality factor of the secondary circuit with a tuning capacitor (hence, operating at resonance frequency) [17], and ω_0 is the resonance angular frequency. Q and ω_0 can be expressed as in Equation 2.14 and Equation 2.15, where R_{AC_S} is the intrinsic AC resistance of the wire in the secondary coil at the operating frequency [17]. It is important to note that Equation 2.14 and Equation 2.15 can be applied to both the secondary and primary sides. Then, the maximum power that can be supplied to the secondary circuit in the compensated condition can be expressed by the product of Equation 2.10 and Equation 2.16, shown in Equation 2.17. If Equation 2.12 and Equation 2.17 are compared, it can be seen that the gain in the compensated output power is by a factor of $2Q$, suggesting that this value should be maximized as much as possible [2].

$$Q = \frac{\omega_0 L_S}{R_{AC_S}} \quad (2.14)$$

$$\omega_0 = \frac{1}{\sqrt{L_S C_S}} \quad (2.15)$$

$$V_{OC} = V_{S,max} = j\omega_0 M I_P Q \quad (2.16)$$

$$P_{c,max} = |V_{OC} I_{SC}| = \frac{\omega_0 M^2 I_P^2 Q}{L_S} \quad (2.17)$$

If Equation 2.17 is rewritten in terms of magnetic and electric quality factors, and considering that the magnetic coupling coefficient can be expressed as $k = M/\sqrt{L_P L_S}$, we get the following equation [17]:

$$P_{c,max} = \omega_0 L_P I_P^2 \frac{M^2}{L_P L_S} Q = V_P I_P k^2 Q \quad (2.18)$$

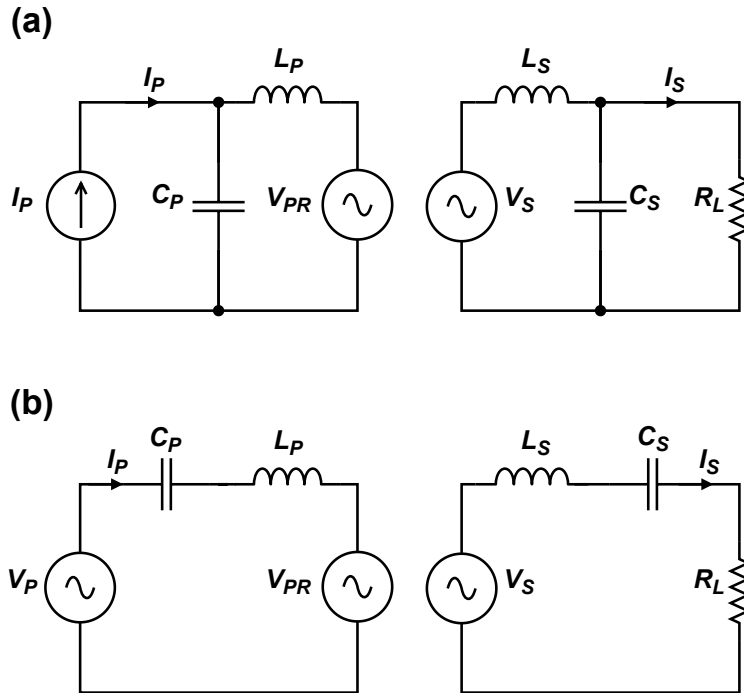


Figure 2.6: (a) Compensation capacitance in parallel, (b) Compensation capacitance in series [2, p. 296]

If the resonance capacitor in the secondary side is now connected in series to the circuit, as shown in the right side of Figure 2.6(b), the capacitors C_P and C_S will resonate with L_P and L_S respectively, where the increment in the Q factor means an increase in the current proportional to Q ; if this increased current at the secondary side is multiplied by the voltage across the load, the increase in power results the same as in the parallel connection scenario [2]; if the series compensation is also applied in the primary side, some benefits, like the reduction in reactive power drawn by the source, can be obtained. Figure 2.7 shows the different compensation topologies that can be found in IPT charging pads; for the purpose of this thesis, the study will be focused only on the series compensation.

Secondary \ Primary	Uncompensated	Series compensated	Parallel compensated
Uncompensated			
Series compensated			
Parallel compensated			

Figure 2.7: Compensation topologies [3, p. 86]

2.5. Types of IPT systems

Due to the vast variety of applications for the IPT systems, these can be classified in different ways. The overall system's constraints often determine which type of IPT configuration to use; at any case, the objective is usually to maximize the magnetic coupling coefficient (k) between the two parts [23]. Here, two different classifications will be presented. The first one, determined by the coil topology, and the second one, by the strength of the magnetic coupling.

1. by Coil topology: For this case, many different layouts for the coils can be built depending on the system's constraints, for instance: the available space, available material, expected coils misalignment, among others. Many studies have been carried out in order to identify the performance of the different the coil topologies, which result in a series of pros and cons for each one of them; then, depending on the specific application, these results can be weighted in order to come up with the optimal coil topology. Figure 2.8 show 16 different types of coil topologies. Below, the advantages of some of the main topologies are presented:

- (i) The circular topology has the largest coupling coefficient (k), only under the condition where the area enclosed by the circular coil is the same as that of the rectangular coil [19].
- (ii) If the actual available space for the IPT pads is considered, the rectangular coil would be able to cover a larger area, imposing an advantage over the circular coil in this sense [19].
- (iii) The circular and rectangular coils have the largest efficiency only under the condition where the area power density (α [W/m^2]) is the same among the compared coils, followed by the DD-DD and DD-DDQ configurations [19].

- (iv) Circular couplers use the largest amount of ferrite and the least amount of copper for the same performance [1].
- (v) The circular and rectangular topologies surpass the DD-DD and DD-DDQ topologies in terms of area power density (α [W/m²]) and transmission efficiency by values of around 1% to 4% [1].
- (vi) In misaligned conditions, the DD-DDQ configuration overcome the other topologies, meaning that it has the lower misalignment difference for the same α [W/m²] [1].
- (vii) Rectangular and circular couplers have lower stray flux densities if compared to the DD-DD and DD-DDQ couplers [1].

In this thesis, the IPT system to be studied will have a *rectangular* topology, the main reasons being points (ii), (iii), (v) and (vii) from the previous list, in addition to simplicity that entails fabricating a rectangular coil. It's important to mention that point (ii) is especially relevant in EV applications since the available area for the charging pads is limited by the size of the vehicle.

2. by Strength of magnetic coupling: Magnetic coupling is defined as the phenomenon that occurs when two conductors (namely two coils) are configured in such a way that a current flowing through one of them induces a voltage at the terminals of the other one due to electromagnetic induction. The coupling coefficient is a parameter that allows knowing the level of coupling between two coils, and it can be calculated as shown in Equation 2.19, where L_1 is the self-inductance of the first coil, L_2 is the self-inductance of the second coil, and M is the mutual inductance. The two types of IPT systems within this category are: (1) *Tightly coupled* and (2) *Loosely coupled*. For the tightly coupled IPT systems, the coupling coefficient between the two coils is high, which means that the leakage inductance is very low compared to the mutual inductance of the coils. These types of systems are largely used in the power sector where transformers of all types serve as links between the power lines [3]. On the other hand, loosely coupled systems have a very low coupling coefficient, meaning that the leakage inductance can be larger than the mutual inductance of the coils. These systems are mainly used for WPT applications, where the receiver coils should be free to move with respect to the transmitter coil, thus physical contact between both coils is avoided. For these cases, the high reactive power created by the leakage inductance is compensated by the addition of *compensation capacitors*, which will counteract the effect of the inductive reactance, and increase the efficiency and power transfer capability [23], as mentioned in section 2.4. Figure 2.9 shows a graphic representation of a tightly and loosely coupled IPT systems, where the addition of capacitive compensation can be seen for the loosely coupled case. In this thesis, we will study a loosely coupled system.

$$k = \frac{M}{\sqrt{L_1 L_2}} \quad (2.19)$$

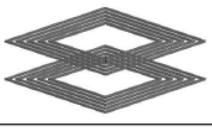
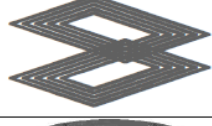
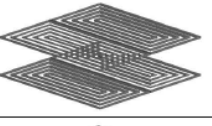
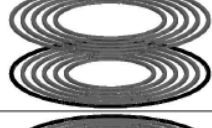
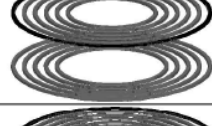
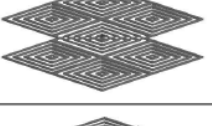
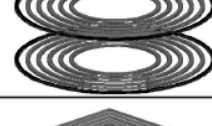
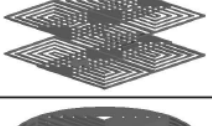
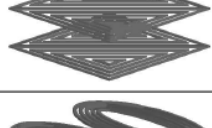
Circular		DD Overlapped	
Square		DDQ	
Rectangular		Two Squares	
Compensation Winding Primary		Two Squares Overlapped	
Compensation Winding Secondary		Four Squares	
Compensation Winding Both-Sided		Four Squares Overlapped	
Triangular		Circular Quartered	
DD		Circular Quartered Overlapped	

Figure 2.8: Coil topologies [4, p. 4]

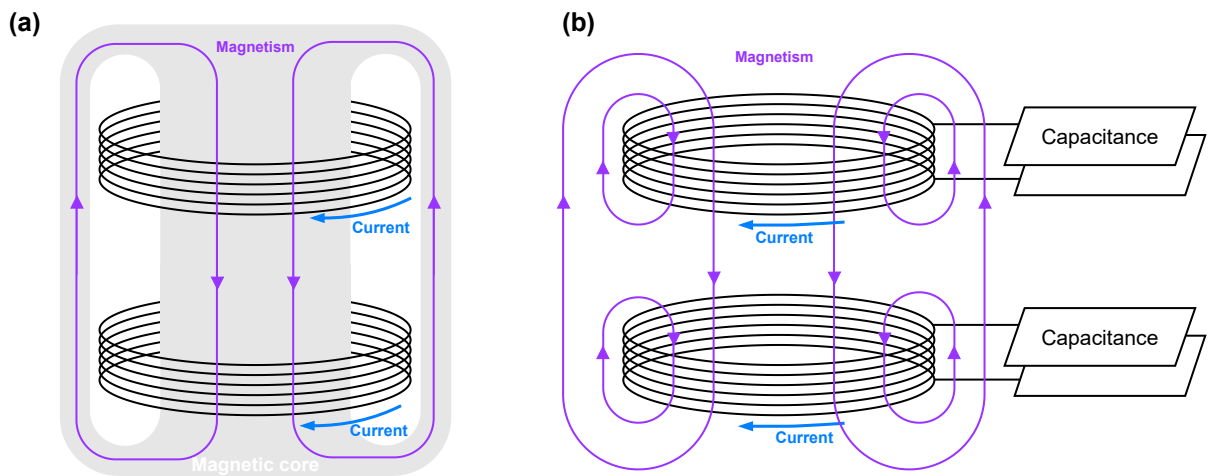


Figure 2.9: (a) Tightly coupled system and (b) Loosely coupled system

2.6. Main elements of the IPT charging pads

A basic IPT system must have at least the following elements:

1. *Power supply + Power Electronics (PE)*: Energy will be taken from either a battery or an utility, and the PE will adjust the transferred energy according to the IPT system requirements.
2. *Transmitter pad*: Which will be excited with an AC current to create the alternating magnetic field.
3. *Receiver pad*: Which will link with a portion of the magnetic field created by the transmitter pad.
4. *Power electronics + Electric load*: PE will adjust the transferred energy according to the electric load requirements.

Even though there are many different types of power supply configurations, all of them are usually capable to achieve the same power output, with different frequencies, reliability and efficiencies; nevertheless, it is becoming more common to focus on power suppliers that prioritizes current control, with unity power factor and controlled frequency [17]. For the purpose of this thesis, the research will be focused mainly in the second and third elements of the list previously shown, which are the transmitter and receiver pads. The main elements of the IPT pads are shown in Figure 2.10.

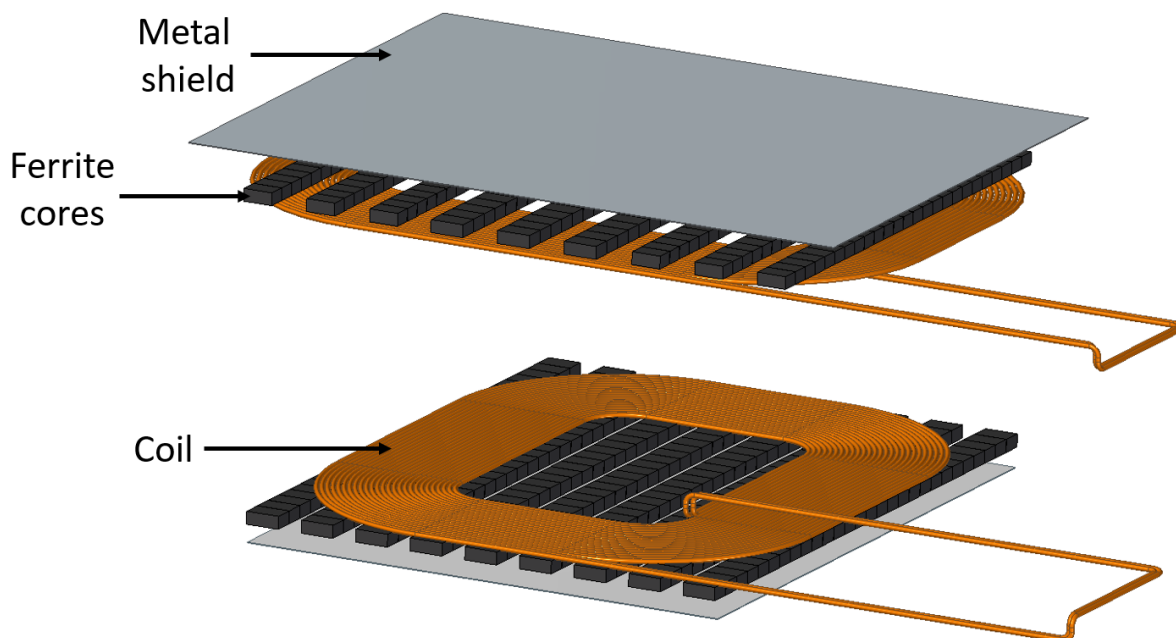


Figure 2.10: Main elements of the IPT charging pads

It can be seen from Figure 2.10 that the three main elements of the IPT pads are: (1) the coils, (2) the metal shields, and (3) the ferrite cores. With respect to the coils, some important information about the topologies has already been mentioned in section 2.5, but another important aspect of the coils is the emerging use of *Litz wire*. This type of wire is becoming popular to build the coupler's coils, for several important reasons that include, but are not limited to the following [24]:

1. Reduced AC losses in high-frequency windings, due to mitigation of skin and proximity effect
2. Increased efficiency
3. Lower operating temperatures
4. Substantial weight reduction

It is important to mention as well that the current, wiring and operation frequency are progressively becoming subjected to international standards, but still, a great flexibility in the design of the coils is possible, mainly in terms of the magnetic circuit, controllers, protection, electrical circuitry and Q -factor, of which the magnetic circuit is the most flexible of all [17]. IPT systems for wireless charging are loosely coupled, with coupling coefficients (k) ranging from around 0.01 to 0.5; increasing k tends to be an important criterion for designing an IPT system, and for this matter, ferrite cores are used, as these elements give the capability to considerably improve the flux path to increase the magnetic coupling and reduce the leakage flux. In regards to the metal shield, which is usually made out of copper or aluminum, its main purpose is to reduce the magnetic stray fields [19], this is achieved because the eddy currents induced in the metal shield decrease the H-field penetration since they oppose the magnetic field created by the coils as per Lenz's law [1]. As mentioned in section 2.5, the IPT coil studied in this thesis has a rectangular shape, and the ferrite cores are arranged as shown in Figure 2.11.

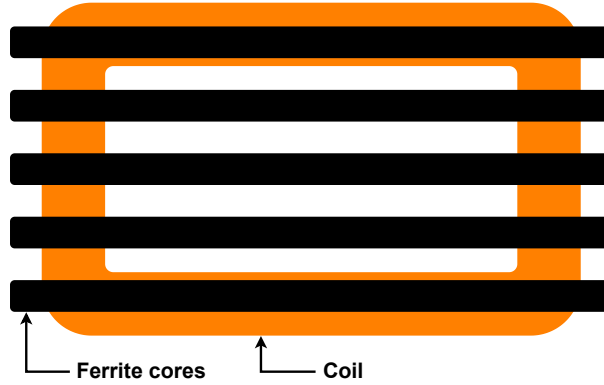


Figure 2.11: Example of ferrite cores arrangement (Top view)

2.7. Equivalent circuit of the IPT system

In order to develop the equations of the equivalent circuit of the IPT coils, Figure 2.12 can be used as reference, where the subscripts 1 and 2 refer to the primary and secondary sides respectively. The differential equations that describe the circuit from Figure 2.12(a) can be represented as in Equation 2.20 and Equation 2.21, where L is the self-inductance and M the mutual inductance [5].

$$u_1 = L_1 \frac{di_1}{dt} - M \frac{di_2}{dt} \quad (2.20)$$

$$u_2 = M \frac{di_1}{dt} - L_2 \frac{di_2}{dt} \quad (2.21)$$

u_1 and u_2 represent the voltage at the coil's terminals, and i_1 and i_2 the currents at each coil. When the turns ratio n is equal to 1, the circuit can be represented as in Figure 2.12(a). If the turns ratio is now different from 1, the circuit can be represented as in Figure 2.12(b), as long as the terminals' behavior stay unaffected [5]. This transformation ratio can be defined in a way that facilitates further calculations, such as in Equation 2.22, where k is the magnetic coupling coefficient, represented in Equation 2.19. This allows the omission of the second inductance in series, as shown in Figure 2.12(c).

$$n = k \sqrt{\frac{L_1}{L_2}} \quad (2.22)$$

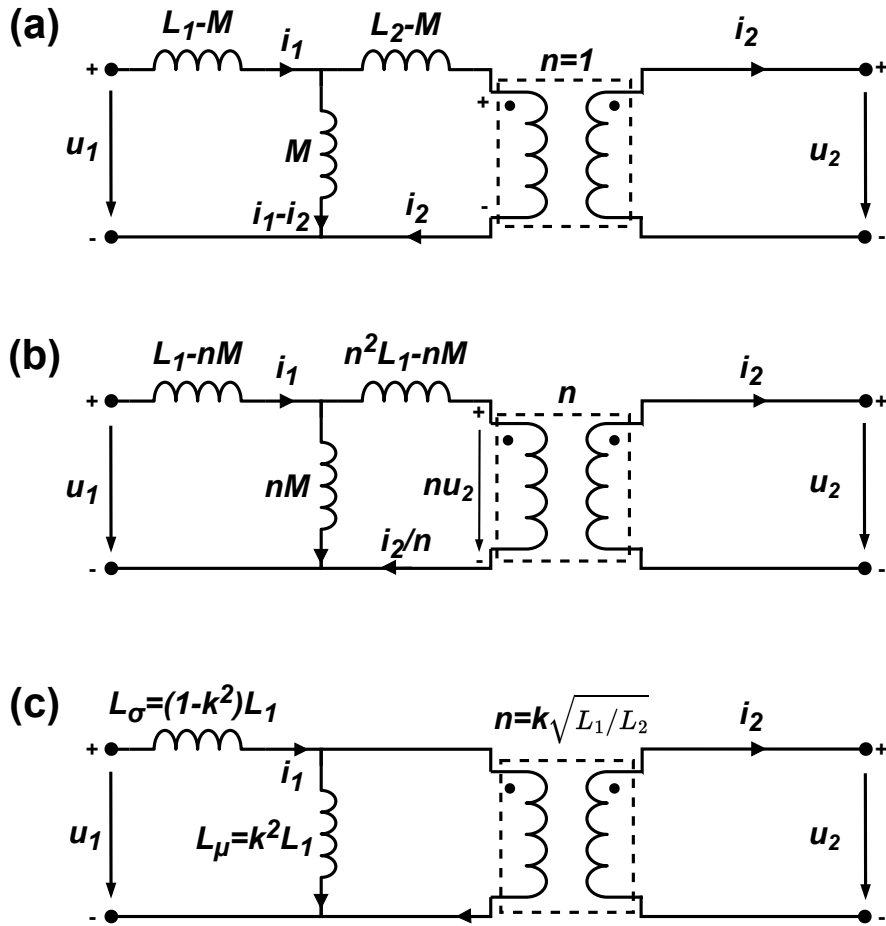


Figure 2.12: (a) IPT equivalent circuit, with transformation ratio $n=1$. (b) For general transformation ratio n . (c) For transformation ratio $n = k\sqrt{L_1/L_2}$, where leakage inductance is referred to the primary side [5, p. 22]

From this point, three different measurements can be done to obtain the values of L_σ , L_μ and n . First, the receiver coil has to be shorted, so $u_2 = 0$, if then, a sinusoidal excitation voltage u_1 with an angular frequency ω is applied to the transmitter coil, we can calculate L_σ as shown in Equation 2.23. Then, L_μ can be calculated as shown Equation 2.24, where the receiver coil is left as an open circuit ($i_2 = 0$). Finally, n can be calculated by connecting the voltage source to the receiver side, and then measuring the transmitter side voltage; the ratio between those two values is n , as shown in Equation 2.25.

$$L_\sigma = \frac{\hat{U}_1}{\omega \hat{I}_1} \Big|_{u_2=0} \quad (2.23)$$

$$L_\mu = \frac{\hat{U}_2}{\omega \hat{I}_1} \Big|_{i_2=0} \quad (2.24)$$

$$n = \frac{\hat{U}_1}{\hat{U}_2} \Big|_{i_1=0} \quad (2.25)$$

If the circuit analysis is now applied to the series-series compensated IPT system (shown in Figure 2.13), by applying Kirchhoff's voltage law, the equations for the transmitter and receiver sides can be derived, as seen in Equation 2.26 and Equation 2.27 [6]. The mutual inductance M is derived using Equation 2.19, and the equivalent load resistance (R_{ac}) can be calculated as in Equation 2.28, where R_L is the equivalent load resistance after the rectifying [6], as shown in Figure 2.14.

$$V_{AB} = (R_1 + j\omega L_1 + \frac{1}{j\omega C_1})I_1 + j\omega M I_2 \quad (2.26)$$

$$0 = j\omega M I_1 + (R_2 + R_{ac} + j\omega L_2 + \frac{1}{j\omega C_2})I_2 \quad (2.27)$$

$$R_{ac} = \frac{8}{\pi^2} R_L \quad (2.28)$$

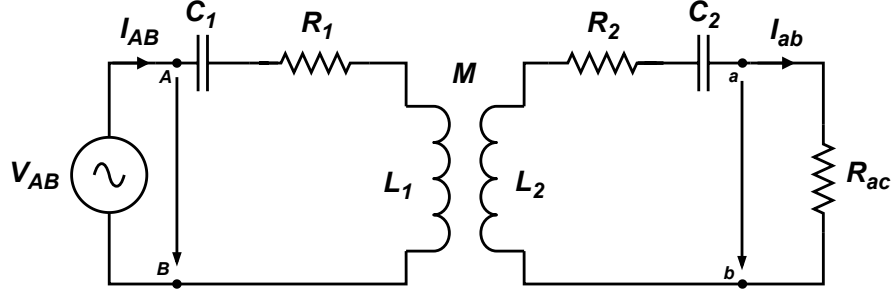


Figure 2.13: Series-series compensated IPT system [6, p. 367]

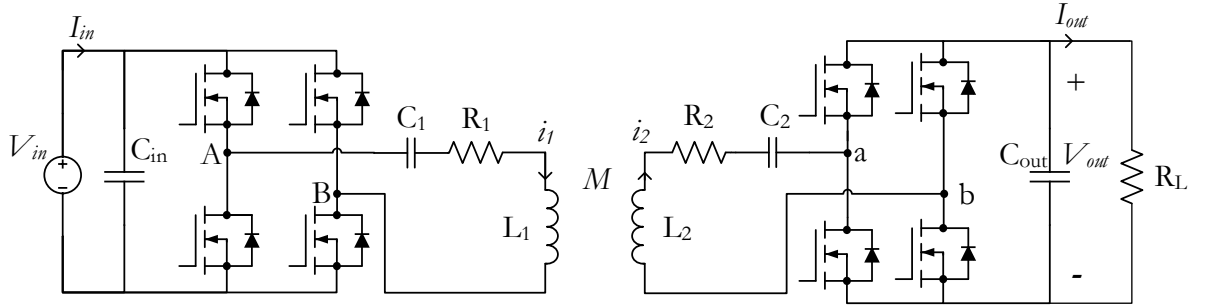


Figure 2.14: Series-series compensated IPT system [6, p. 368]

It is important to mention that Equation 2.26, Equation 2.27 and Equation 2.28 can only be used as frequency analysis of the equivalent circuit shown in Figure 2.13 for its different operating points. Since the behavior of these operating points in terms of the output power and efficiency is influenced by the inverter, the performance of these operating points must not be done with these equations only, but rather with the circuit shown in Figure 2.14 [6].

By using an optimal load impedance matching algorithm together with dual-side control that will result in a maximum power transfer efficiency for a specific operating condition, and by taking into consideration that the primary and secondary coils are asymmetric, the equivalent load (R_L) can be represented as in Equation 2.29, where r_{acT} and r_{acR} are the AC resistances of the transmitter and receiver coils and $R_{L,eq}$ is the effective equivalent load resistance of the receiver circuit [1]; the derivation for this formula can be found in [1, p.5427].

$$R_{L,eq} \approx \omega M \sqrt{\frac{r_{acR}}{r_{acT}}} \quad (2.29)$$

Subsequently, the reference receiver DC voltage ($U_{2,dc}^*$) during load impedance matching is calculated using Equation 2.30. Accordingly, $U_{2,dc}^*$ is used as set point to secure the maximum power transfer efficiency [1]; then, the value of $U_{1,dc}^*$ is calculated based on the reference value of $U_{2,dc}^*$. Due to possible coils misalignment, the mutual inductance of the coils (M) may vary, which will lead to a change in the value of $U_{2,dc}^*$. In such case, active impedance matching can be carried out in real-time with the estimation of the new coupling coefficient (k'), thus, the new reference voltage at the receiver side can be expressed as in Equation 2.31. The estimation of k' or M can be derived by measuring the currents and voltages at the primary and secondary pads [1].

$$U_{2,dc}^{*2} \approx \frac{\pi^2}{8} \eta_{rec} \omega M P_{out} \sqrt{\frac{r_{acR}}{r_{acT}}} \quad (2.30)$$

$$U_{2,dc}'^* = U_{2,dc}^* \sqrt{\frac{k'}{k}} \quad (2.31)$$

3

IPT Pads Casing Desing

In this chapter, the design and assembly process of the casings for the charging pads of a 50 kW IPT system will be addressed.

Research question:

Why is it required to design an accurate and modular casing for the IPT charging pads?

Motivation:

1. If the dimensions of the active elements of the IPT charging pads (coils, ferrite cores and metal shields) to be built are as close as possible to the dimensions obtained from a multi-objective optimization (MOO) study, then the optimization objectives (criterion) outcome will be as expected.
2. A casing for the IPT charging pads will serve as a fixture to keep all the active elements of the pads in place.
3. A modular design of the casing for the IPT charging pads will allow us to: save time, money, and weight; and to easily implement future changes or upgrades in the pads.

3.1. IPT pads dimensions and parameters

A MOO study for the charging pads of a 50 kW IPT system was performed at the DC Systems, Energy Conversion and Storage (DCE&S) research group from TU Delft in order to enhance the power transfer levels between the two coils. The followings were the optimization targets for such study [1]:

i) Maximize: Power transmission efficiency (aligned condition) [%]

$$\eta_T = \frac{P_{out}}{P_{in}}$$

ii) Maximize: Gravimetric power density [W/kg]

$$\gamma = \frac{P_{out}}{m_{sys}}$$

iii) Maximize: Area power density [W/m²]

$$\alpha = \frac{P_{out}}{A_{rec}}$$

Where P_{out} and P_{in} are the input and output powers at the terminals of the coils, A_{rec} is the area of the receiver coil, and m_{sys} is the mass of the active elements of the IPT charging pads [1]. The optimization

variables and the results from the optimization study can be seen in Table 3.1 and Table 3.2 respectively. It is important to mention that, if the casing design is not accurate enough, the performance of the optimization objectives will be negatively affected; for instance, a change in the wire's and ferrite cores layout can affect the mutual inductance of the coils, leading to a different optimal load impedance (see Equation 2.29). A variation in the pads active elements layout can also lead to a compensation capacitance different to the expected one since the self-inductance of the coils would be affected by such variation (see Equation 2.15). Another example of the relevance of maintaining an accurate coil layout is the influence of the gap between coil turns on the proximity effect; this effect can be defined as the increase in the effective AC resistance of a wire due to an overcrowding of the current distribution caused by the electromagnetic induction of adjacent conductors. For this reason, the design, manufacturing and assembly process of the casing should be accurate, and at the same time robust, in order for the active elements of the IPT charging pads to remain in the proper position during the operation of the system.

Table 3.1: Optimization variables of a multi-objective optimization study for the charging pads of a 50 kW IPT system

Optimization variables	
Outer coil length	Core height
Outer coil width	Number of cores
Inner coil length	Gap between cores
Inner coil width	Shield length
Gap between turns	Shield width
Core length	Gap between coil and cores
Core width	Gap between cores and shield

Table 3.2: Results of a multi-objective optimization study for the charging pads of a 50 kW IPT system

Primary coil			Secondary coil		
Parameter	Value	Unit	Parameter	Value	Unit
Outer coil length	76.976	cm	Outer coil length	87.81	cm
Outer coil width	63.988	cm	Outer coil width	65.823	cm
Inner coil length	42.56	cm	Inner coil length	55.654	cm
Inner coil width	29.572	cm	Inner coil width	33.666	cm
Gap between turns	1.8288	mm	Gap between turns	2.5648	mm
Core length	78.12	cm	Inner core length	64.17	cm
Core width	4.32	cm	Inner core width	4.32	cm
Core height	1.64	cm	Inner core height	1.64	cm
Number of cores	9	–	Outer core length	63.5	cm
Gap between cores	3.11	cm	Outer core width	3.81	cm
Shield length	76.976	cm	Outer core height	1.62	cm
Shield width	63.988	cm	Number of inner cores	3	–
Gap between coil and cores	0.303	mm	Number of outer cores	6	–
Gap between cores and shield	2.39	cm	Gap between cores	4.74	cm
Coil turns	13	–	Shield length	87.81	cm
			Shield width	65.823	cm
			Gap between coil and cores	3.24	mm
			Gap between cores and shield	4.88	cm
			Coil turns	11	–

3.2. IPT pads casing requirements

The main design requirements for the casings of the IPT pads can be summarized as follows:

1. Accurately dimensioned

As mentioned before, this is required in order to procure that the multi-objective optimization targets perform as expected. In order to achieve this, the casing model should be done in a 3D CAD program. This will allow having precise dimensions, having easy maneuverability and visualization of the design, having a CAD file that allows for easy manufacturing, and having a proper CAD file that allows for future changes or upgrades.

2. Easy and fast to manufacture

Since the whole 50 kW IPT charging system prototype needs to be completed in a limited amount of time, the manufacturing of the casings needs to be as quick as possible. For this reason, it was decided to proceed with a design that is able to be laser-cut, instead of being 3D printed, CNC machined, or molded.

3. Easily and fast to assemble

The casing design should be done in a way that allows an easy and fast assembly process of the laser-cut parts.

4. Modular-designed

The casing design should be modular, meaning that, once the casing is assembled, the parts that conform the casing should be prone to be easily removed in order to have access to the active elements of the IPT charging pads. Access to these elements is needed so future changes or upgrades could be implemented on them.

5. Light

It is required to have light casings since the active elements of the charging pads are already considerably heavy. Reducing the mass of the casing as much as possible will allow easy manipulation of the charging pads, mainly for testings, such as in the aligned/misaligned scenarios. Also, the material needs to have good mechanical properties and be able to be laser-cut. For this reason, it was decided to use acrylic as the material for the casing.

6. Adequately cooled

The hysteresis losses in the ferrite cores [25] and AC losses in the windings and metal shields lead to a temperature rise in such elements; besides this, the Litz wire and ferrite cores must remain below their rated temperatures, which are 180 °C and 100 °C respectively ¹. For this reason, a cooling system needs to be able to be mounted in the casings for the IPT pads.

7. Robust

The casing needs to be robust enough to make sure the active elements remain in place during the casing manipulation and pad operation.

3.3. IPT pads design process

After the design requirements are settled up, the CAD design could begin. In the following subsections, the design process will be described.

3.3.1. CAD model of the active elements

The first step is to do the precise CAD model of the active elements. For this matter, the CAD program *Solid Edge 2021* was used. It is important to mention that the design strategy will be the same for

¹It is recommended to maintain the ferrite cores under 100 °C since above this temperature the specific power losses [W/m³] begin to considerably increase. In the other hand, the working temperature of the Litz wire is limited to 180 °C due to its H-class insulation. The data sheets of the ferrite cores and the Litz wire can be found in [26] and [27] respectively.

both the primary and secondary coil, so, for simplicity reasons, only the design process of the primary coil will be addressed in this thesis, nevertheless, the final result for both casings will be shown. The first elements to be designed are the coils. Using as reference the dimensions from Table 3.2, and also taking into consideration that the Litz wire to be used ² has a diameter of 4.86 mm, with an initial bend radius of 55 mm from the inner side of the turn, it was possible to do the 2D and 3D sketches of the coils' centerline path (See Figure 3.1 and Figure 3.2). With the sketch ready, a sweep through the centerlines could be done in order to generate the 3D model. It can be seen in Figure 3.3 that the coils' paths form a closed loop, this will be useful for the Finite Element Method (FEM) electromagnetic simulation that will be described in chapter 4.

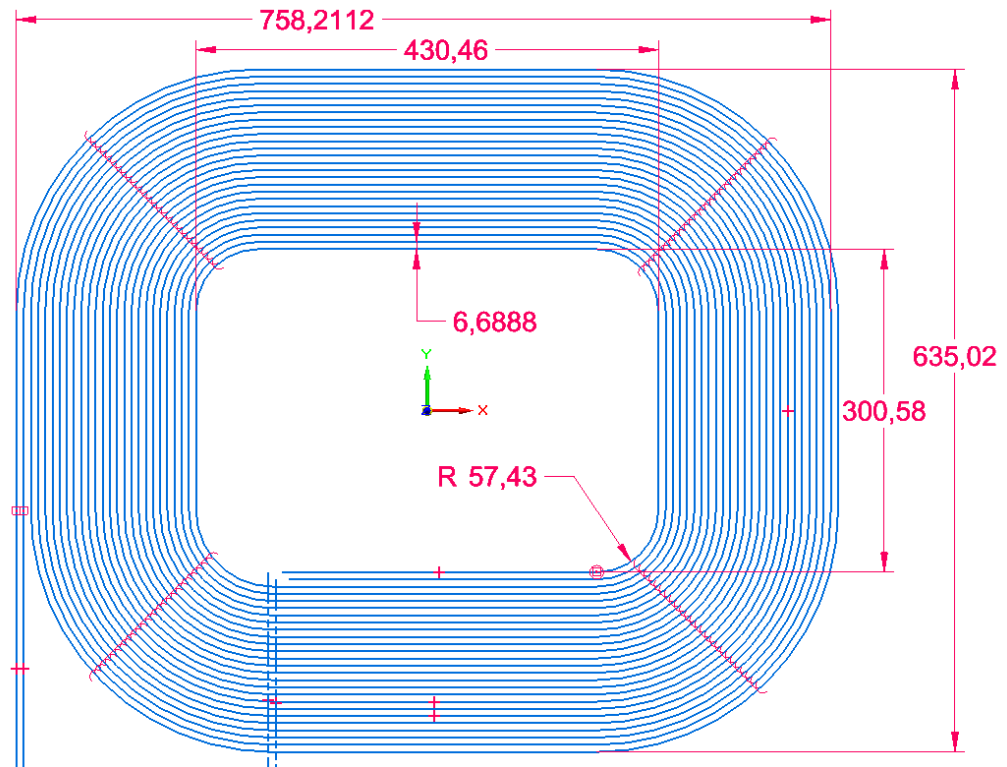


Figure 3.1: 2D sketch of the 50 kW IPT primary coil

²The Litz wire chosen for this project was manufactured by *Elektrisola*. It has a nominal diameter of 4.86 mm, 2205 copper strands individually isolated, and a strand diameter of 71 μm .

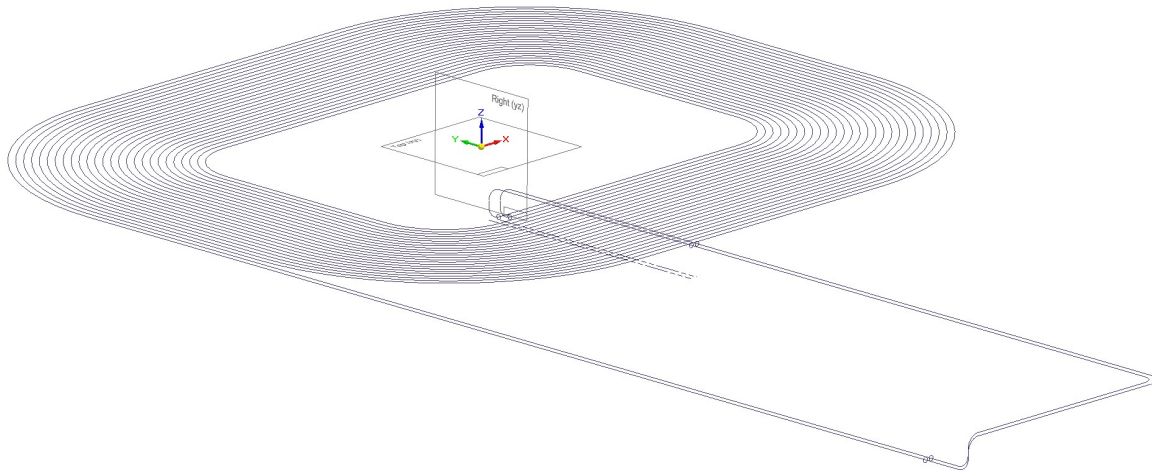


Figure 3.2: 3D sketch of the 50 kW IPT primary coil

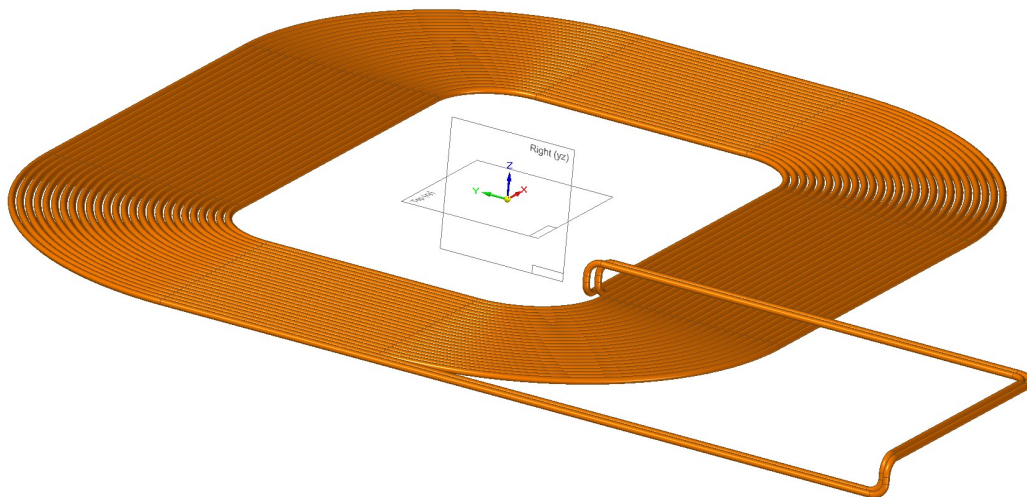


Figure 3.3: CAD model of the 50 kW IPT primary coil

It can also be seen from Figure 3.3 that the coil has a double-wire configuration, which means that the current flow is split into two wires; the purpose of this is to improve the rated current density of the coils. The next step is the CAD design of the ferrite cores, where the dimensions from Table 3.2 were also used. The ferrite cores are conformed by a series of small ferrite plates manufactured by *Ferroxcube*; the purpose of using these small ferrite plates was to make sure that the final dimensions of the cores were as close as possible to the multi-objective optimization study. The dimensions of each of these small plates are 43.2mmx27.9mmx4.1mm (see Figure 3.4), which means that, in order to get to the final core dimensions, four of these plates should be stacked on top of each other, and then 28 of these stacks should be placed next to each other, like shown in Figure 3.5. The final CAD design of a single ferrite core can be seen in Figure 3.6. After completing the ferrite cores design, the virtual assembly can begin. The ferrite cores should be positioned in a symmetric location with respect to the coil as shown in Figure 3.7.

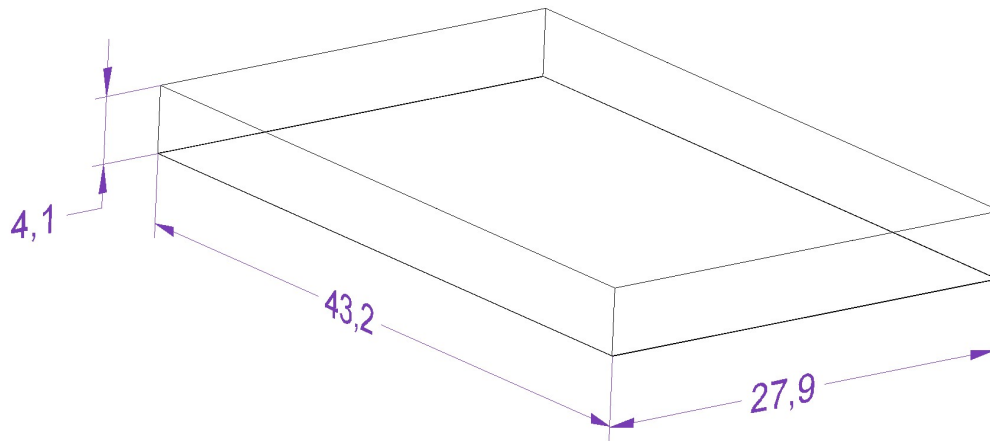


Figure 3.4: Ferrite plate for the cores of the primary pad

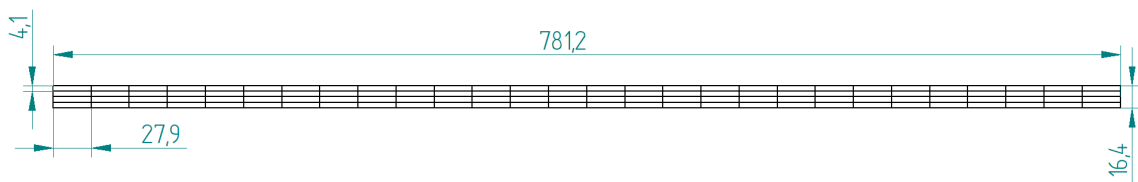


Figure 3.5: Ferrite plates' layout for the cores of the primary pad

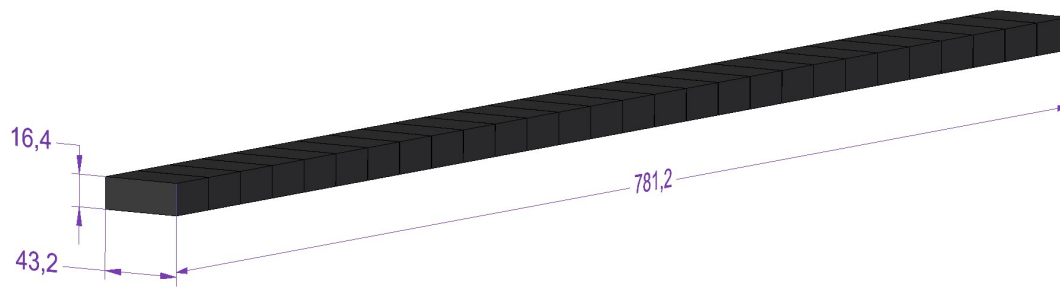


Figure 3.6: Ferrite core for the primary pad

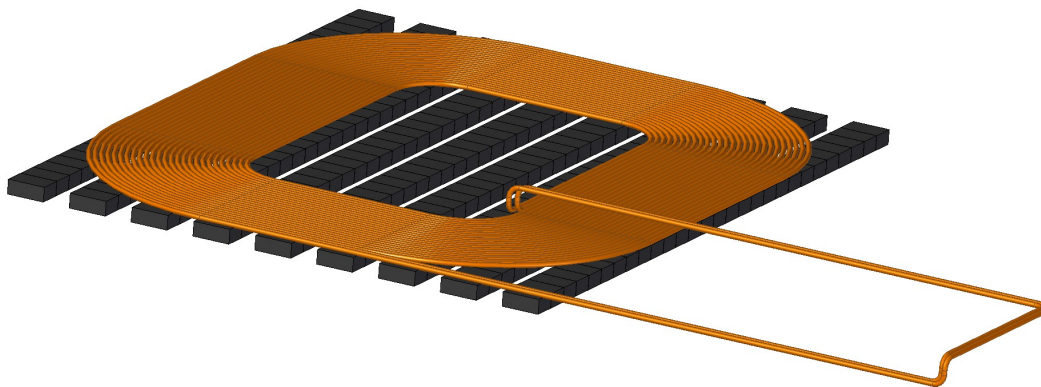


Figure 3.7: Layout for coil and ferrite cores of primary 50 kW IPT pad

The last active element to be designed is the metal shield. The material to be used for this element is copper, with a thickness of 1 mm. The design can be seen in Figure 3.8, where the dimensions from Table 3.2 are also appreciated. Finally, the virtual assembly of the active elements can be completed. In Figure 3.9, the assembly of the active elements can be seen, while Figure 3.10 shows the gaps between the shield and the cores, between the cores and the coil, and between each core.

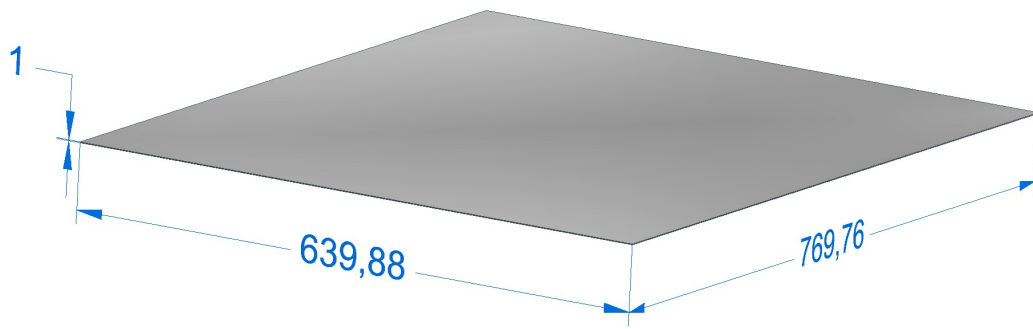


Figure 3.8: Metal shield for the primary pad

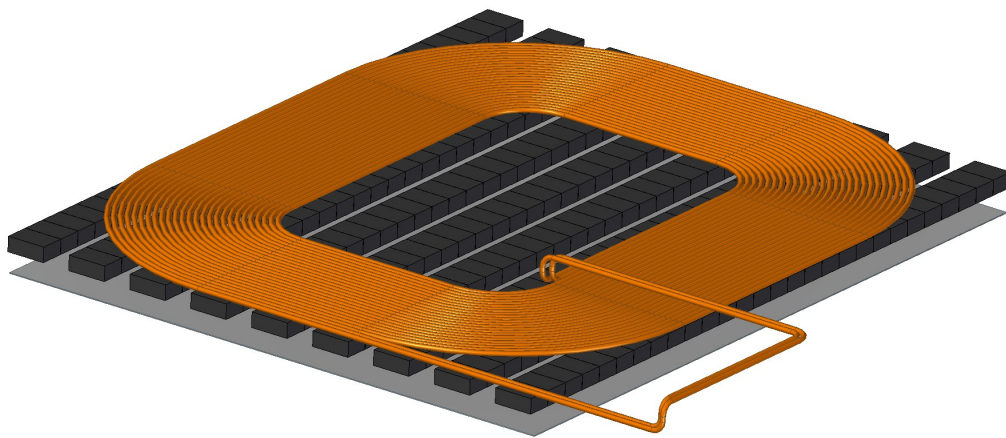


Figure 3.9: Virtual assembly of the active elements from the 50 kW IPT primary pad

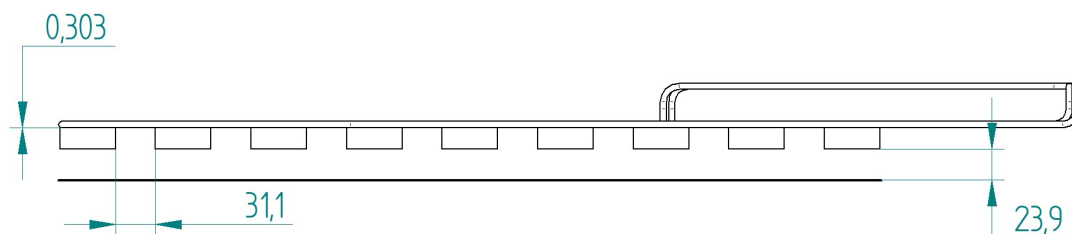


Figure 3.10: Side view of active elements virtual assembly

3.3.2. Cooling system assessment

Due to the power losses in the ferrite cores, coils and metal shields³, it was decided to implement an air-cooling system on the IPT charging pads to prevent an excessive temperature rise in such elements. The cooling system described in [5, p.129] (see Figure 3.11) was used as a reference to design the cooling system for the charging pads of the 50 kW IPT system. The first design requirement to take into consideration was the dimensions of the fan, which had to be no larger than the gaps between each core. Within the different options that complied with this requirement, the one with the highest airflow to power ratio $\left[\frac{m^3/s}{W}\right]$ was selected. The selected fans for the primary and secondary fans can be seen in Figure 3.12 and Figure 3.13 respectively, while their technical specifications can be seen in Table 3.3.

³Taking as a reference the 20 kW IPT system described in [19], the losses in the windings, ferrite cores, and metal shields are around 100, 50 and 150 Watts respectively, which represent the 20%, 10% and 30% respectively of the total losses of the overall IPT system during the aligned condition [19].

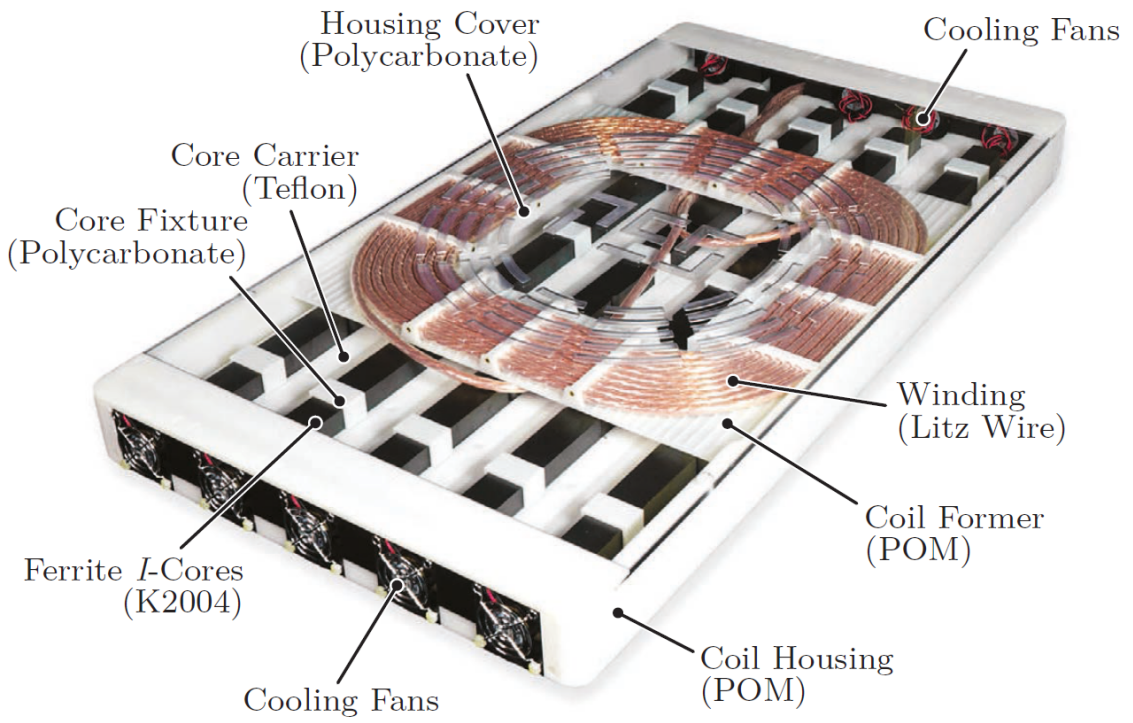


Figure 3.11: IPT charging pad with cooling system from ETH Prototype [7, p.129]



Figure 3.12: Fan for primary IPT pad [8]



Figure 3.13: Fan for secondary IPT pad [9]

Table 3.3: Technical specifications for the IPT fans

	Primary fan		Secondary fan	
Manufacturer	Sanyo Denki America Inc.		Delta Electronics	
Series	San Ace 36		AUC0512	
Model	9GV3612G301		DB-AF00	
Voltage	12	[VDC]	12	[VDC]
Voltage range	7-13.2	[VDC]	10.8-13.2	[VDC]
Size	36x36 (LxH)	[mm]	50x50 (LxH)	[mm]
Width	28	[mm]	15	[mm]
Air flow	0.395	[m ³ /min]	0.566	[m ³ /min]
Power	4.08	[W]	2.16	[W]
RPM	14,000		7,400	
Current rating	0.34	[A]	0.18	[A]
Noise	52	[dB(A)]	38.5	[dB(A)]

Once the selection of the fans was completed, a quick thermal assessment was performed in order to estimate the surface temperature (T_w) of the heat sources in the charging pads (winding, ferrite cores and metal shield). For this matter, the convective heat transfer formulas shown in Equation 3.1 and Equation 3.2 were used, where \dot{Q} are the heat losses, h is the convective heat transfer coefficient, A is the surface area of the heat sources, and ΔT is the temperature difference between the surface of the heat sources (T_w) and the ambient temperature (T_∞).

$$\Delta T = \frac{\dot{Q}}{hA} \quad (3.1)$$

$$\Delta T = T_w - T_\infty \quad (3.2)$$

Since the estimated heat losses of the IPT system are known (53.825 Watts for the primary pad and 35.629 Watts for the secondary pad), and the typical convective heat transfer coefficient values under *Air, forced* condition are also known (see Table 3.4), it was possible to make a broad estimation of T_w , resulting in 22.08 °C for the primary pad elements and 21.39 °C for the secondary pad elements, considering an ambient temperature of 20 °C. It is important to mention that these values were calculated under the worst condition of heat transfer where ($h = 10$), and considering that all the heat sources are at the same temperature, which is not necessarily true. It can be seen that the temperature rise in the heat sources is not high, meaning that it might be possible to prescind from some of the fans.

Table 3.4: Typical values of the convective heat transfer coefficient (h) [15, p.2]

Type of convection	Convective heat transfer coefficient (h) W/(m ² K)
Air, free	2.5 - 25
Air, forced	10 - 500
Liquids, forced	100 - 15,000
Boiling water	2,500 - 25,000
Condensing water vapor	5,000 - 100,000

After the thermal assessment was done, the next step was to include the 3D models of the fans in the assembly. For both types of fans, it was possible to download the *.stp* file (3D CAD files) from the manufacturers' web page. With these 3D models, the assembly of the active elements of the IPT pads together with the cooling fans was completed, as seen in Figure 3.14. From this point, it was possible to begin with the 3D design of the casings for the IPT charging pads.

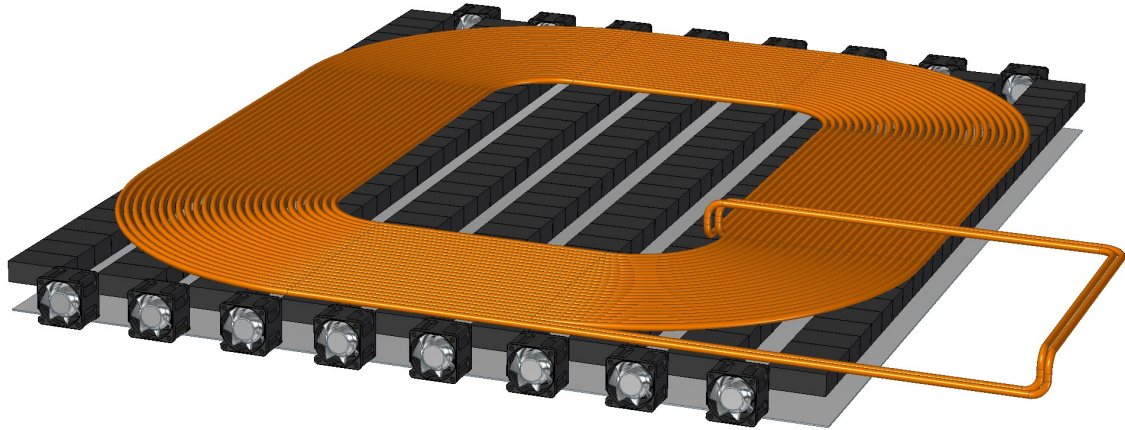


Figure 3.14: Primary IPT charging pad active elements with fans

3.3.3. CAD design of the casing

Once the active elements and the fans of the IPT charging pads were in place, the casings' 3D design could begin. As mentioned in section 3.2, the casings need to be modular and laser-cut. The company chosen for the laser-cutting task was *Laserbeest*, and the available thicknesses they have for the acrylic plates are: 1mm, 2mm, 3mm, 4mm, 5mm, and 8mm [28]. It was important to take this information into consideration while designing the charging pads' casings. Figure 3.15 shows the base and 4 side walls of the casing for the primary IPT charging pad, together with the cooling fans and metal shield.

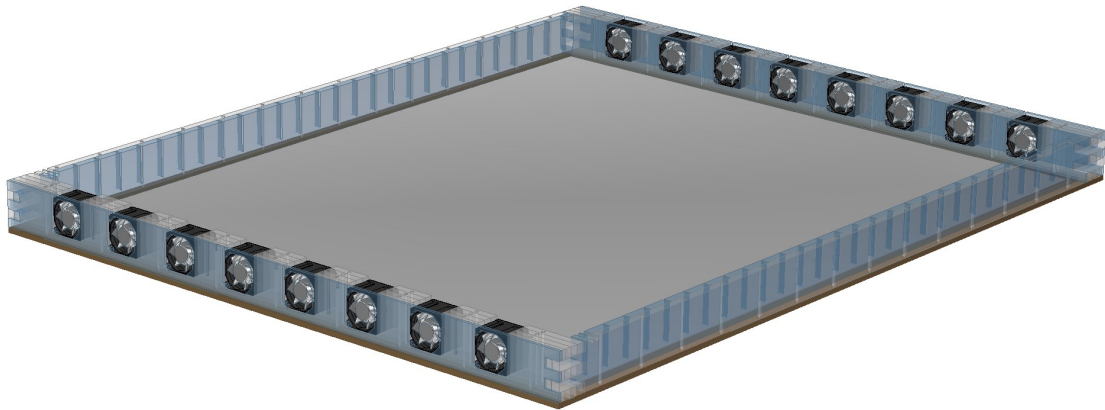


Figure 3.15: Base and side walls of the primary IPT pad casing with cooling fans and metal shield

The next step was to model the ferrite cores' supports. For this matter, thin acrylic structures (shown in yellow in Figure 3.16) were designed, it can be seen that there is one support per each one of the core segments shown in Figure 3.6. Figure 3.17 shows the assembly including the cores.

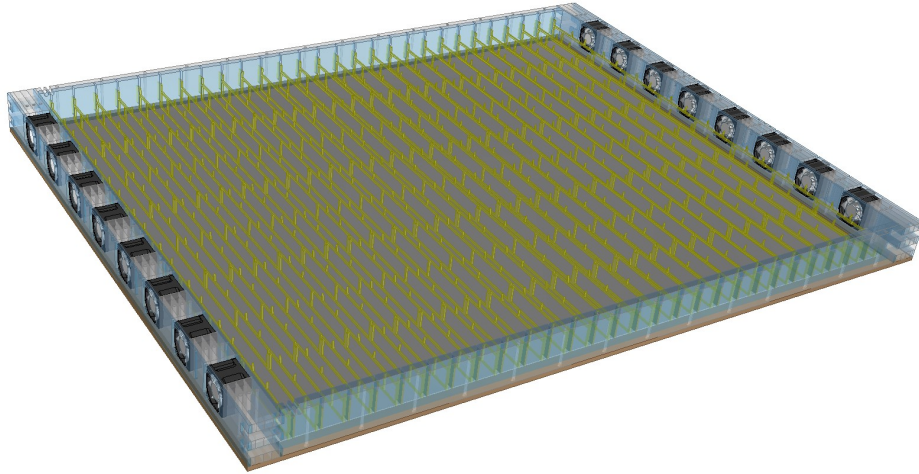


Figure 3.16: Primary IPT pad casing with cores supports

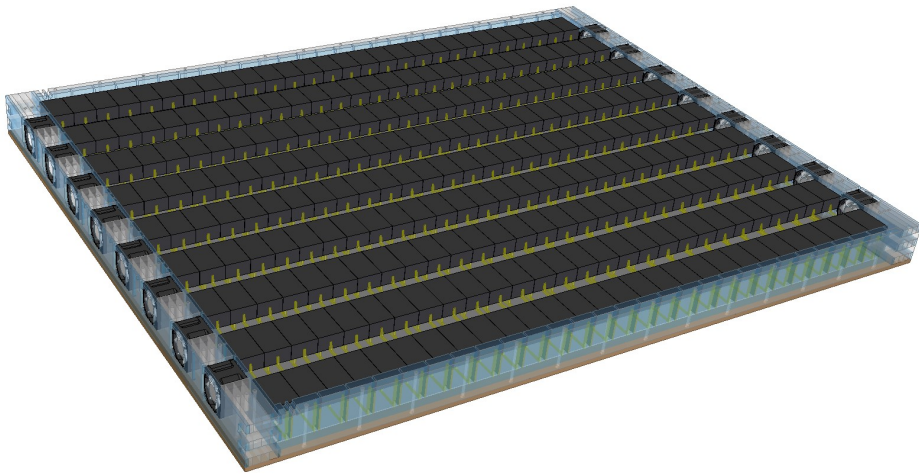


Figure 3.17: Primary IPT pad casing with cores and cores supports

The final step for the casing design was to model the lid of the casing, which will hold the coil. The lid consists of three acrylic layers, that are used to keep the coil retainers (show in red in Figure 3.18) in place. Figure 3.19 shows the lid of the casing for the primary charging pad, including the coil.

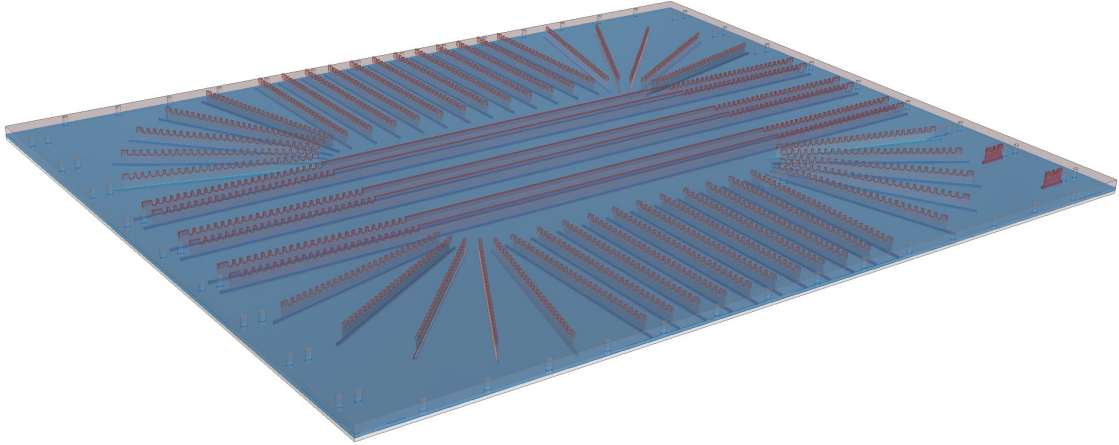


Figure 3.18: Lid for the primary IPT pad casind with coil retainers (shown in red)

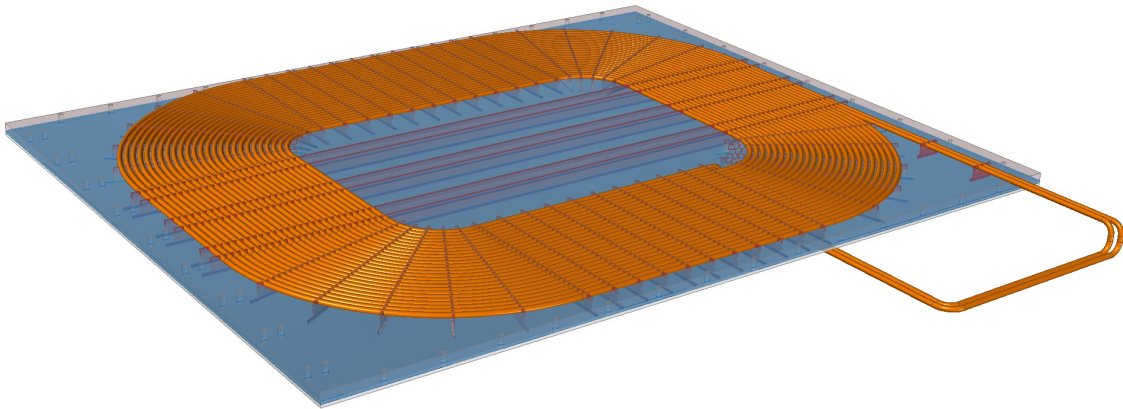


Figure 3.19: Lid for the primary IPT pad casing with coil retainers and coil

The final 3D assembly consists of joining together the lid shown in Figure 3.19 with the sub-assembly shown in Figure 3.17. The final design of the casing for the primary side, including the active elements, can be seen in Figure 3.20, while the final design for the secondary side can be seen in Figure 3.21.

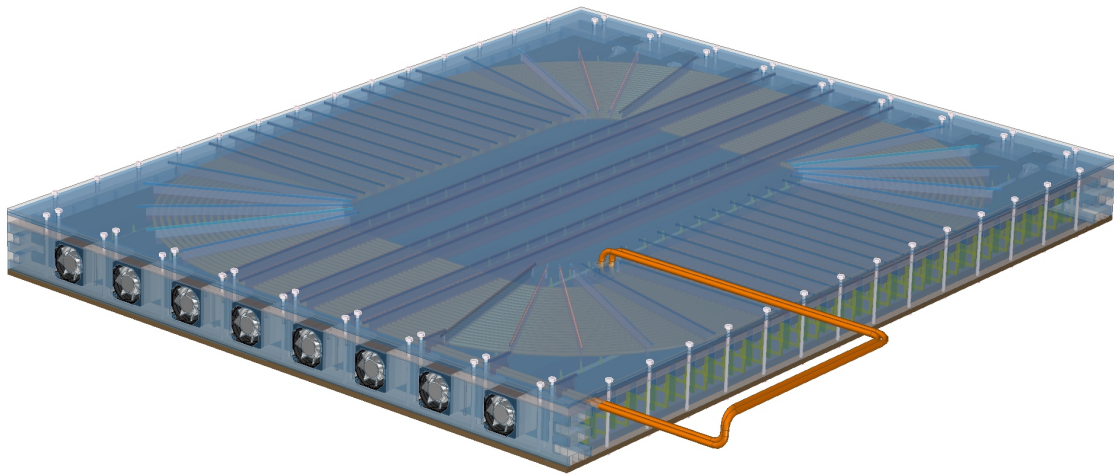


Figure 3.20: Final 3D design of the casing for the 50 kW primary IPT pad

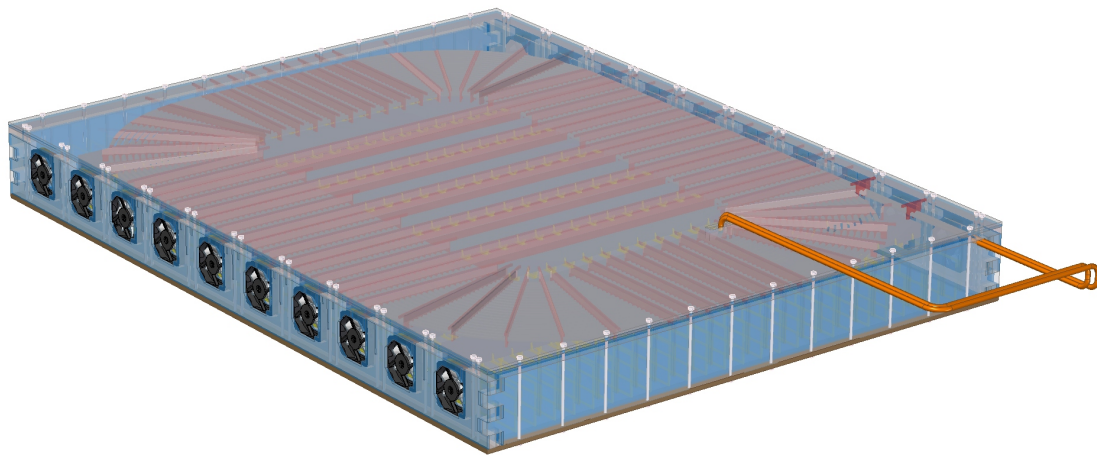


Figure 3.21: Final 3D design of the casing for the 50 kW secondary IPT pad

Once the design was completed, the laser-cutting was done by the company *Laserbeest*. For this matter, they requested drawings of all the casing elements, specifying the thicknesses, dimensions, and color of the acrylic plates. An example of one of the drawings can be seen in Figure 3.22.

PLAAT#: 01
 1200x900mm
 MATERIAAL: Acrylaat (Ondoorzichtig wit)
 DIKTE: 8mm

- 1) Primary_Fan_Walls (6)
- 2) Primary_Side_Walls (2)
- 3) Primary_Side_Walls2 (2)
- 4) Primary_Top_Plate (1)

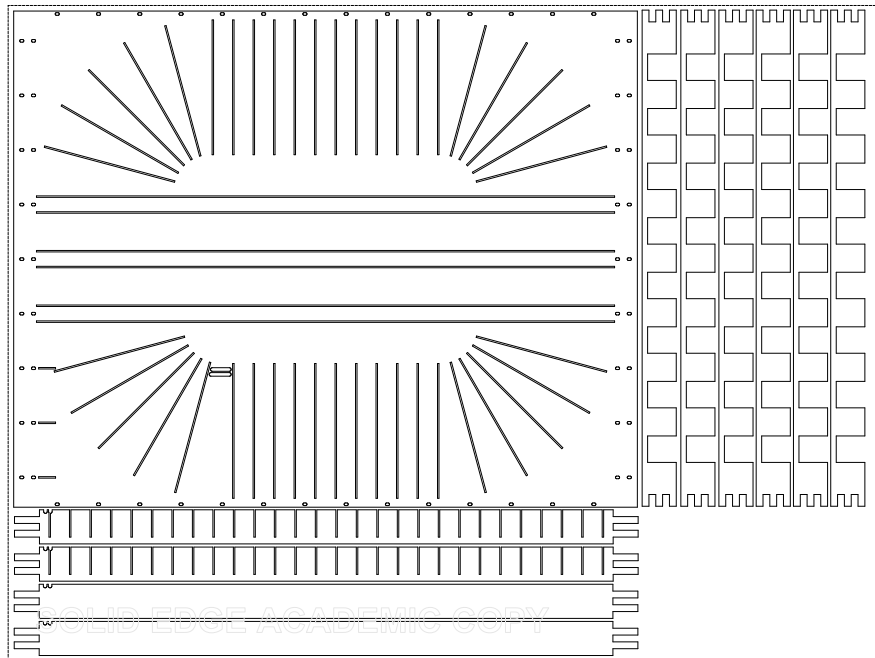


Figure 3.22: Drawing example of the parts to be laser-cut at *Laserbeest*

3.4. IPT charging pads casings assembly

Once the parts were laser-cut and delivered to the Electrical Sustainable Power (ESP) Lab, the assembly process of the IPT pads' casings began. An assembly manual was elaborated in order to join all the parts in the correct way. The main steps of the assembly process can be seen below, where the final assembly of the casing for the primary IPT charging pad can be seen in Figure 3.28.

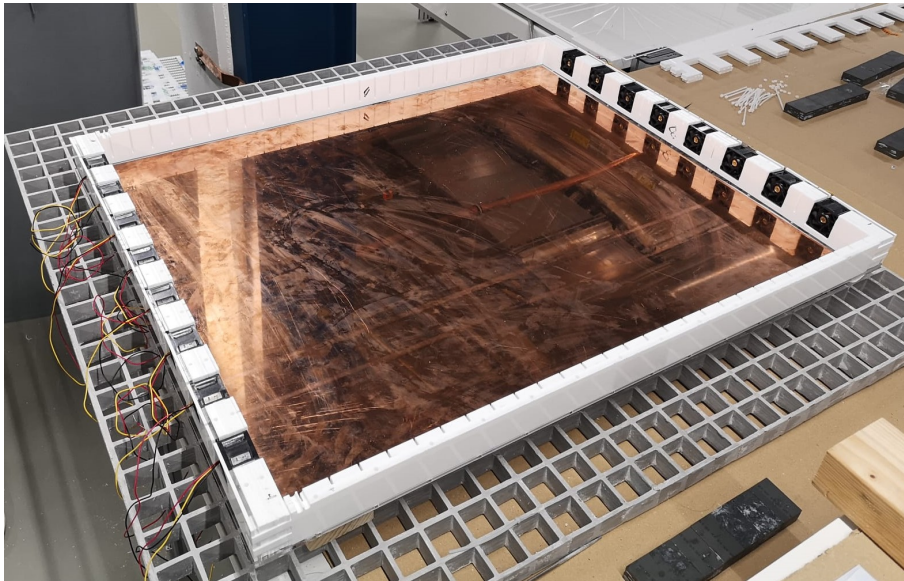


Figure 3.23: Base and side walls assembly of the primary IPT pad casing, including fans

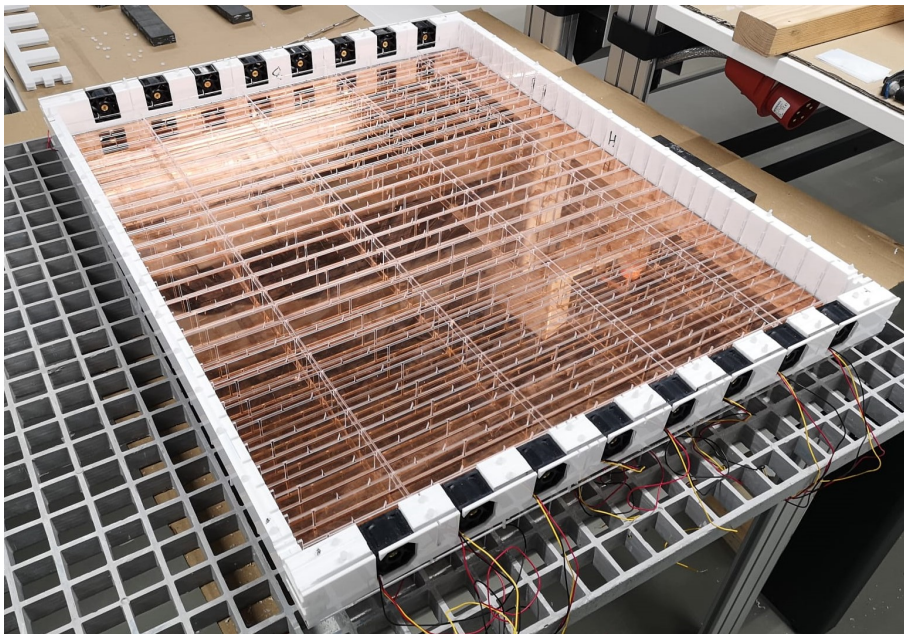


Figure 3.24: Base and side walls assembly of the primary IPT pad casing, including the core retainers

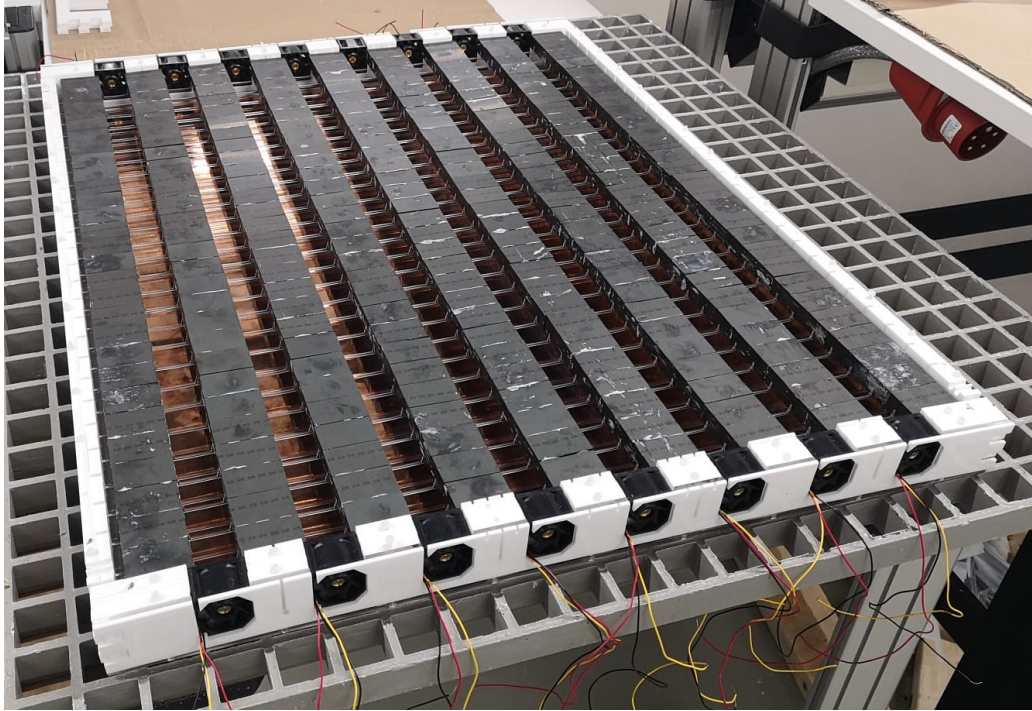


Figure 3.25: Base and side walls assembly of the primary IPT pad casing, including ferrite cores



Figure 3.26: Base and side walls assembly of the primary IPT pad casing, including coil retainers

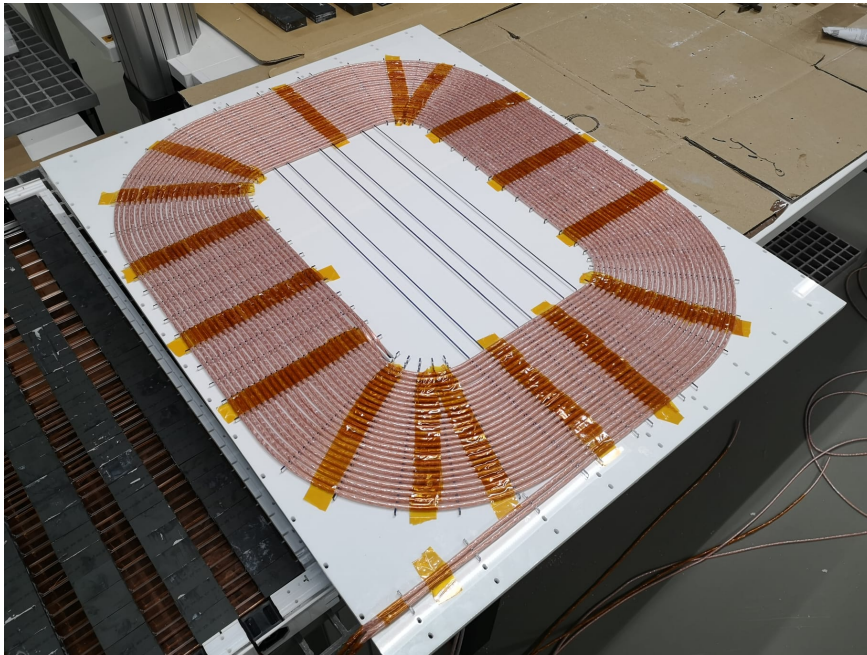


Figure 3.27: Lid assembly for the primary IPT pad casing, including coil

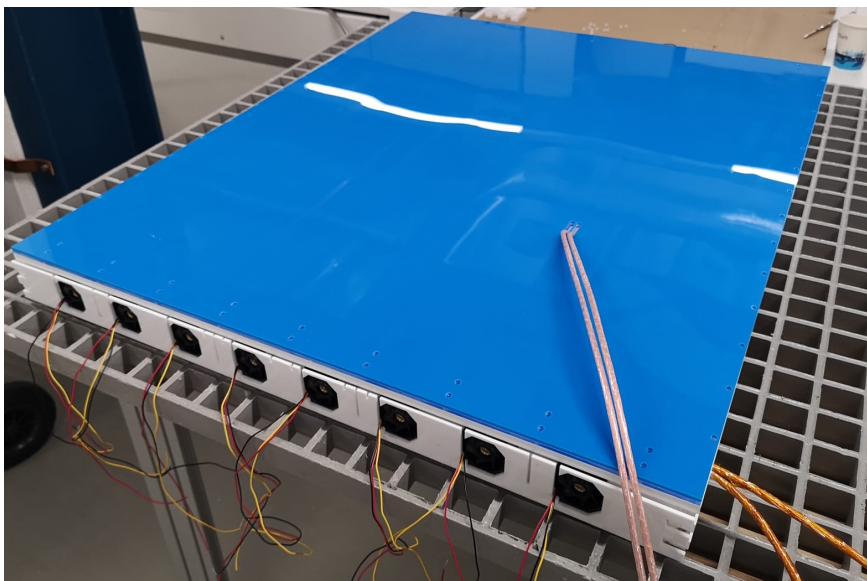
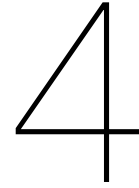


Figure 3.28: Final assembly of the casing for the 50 kW IPT primary pad



COMSOL FEM Simulation

In this chapter, the electromagnetic FEM simulation of the 50 kW IPT charging pads is performed, in order to evaluate the parasitic capacitance in the pads.

Research question:

How does the parasitic capacitance affect the dynamic behavior of the IPT electric system, and what are the risks associated with the parasitic capacitance?

Motivation:

1. Knowing the parasitic capacitance of the IPT coils will allow us to understand and replicate the dynamic behavior of the system, for better circuit modeling.
2. Knowing the parasitic capacitance will provide information regarding a potential over-voltage between the coil terminals, the coil turns, and the coil and the cores/shield.
3. The developed methodology to evaluate the parasitic capacitance can also be used to determine the equivalent circuit of the charging pads, which can be used to test the system under different conditions.

4.1. Parasitic capacitance fundamentals

Parasitic capacitance is an inevitable and generally undesirable capacitance that occurs in electric circuits [29]. When two conductive elements in an electric circuit are in close proximity to each other, there is a possibility to have a capacitance effect, known as parasitic or stray capacitance, between them. It is easier to understand the concept of parasitic capacitance if the working principle of capacitors is known. A capacitor is an electronic device used to store energy in an electric field; it is made up of two conductive elements in close proximity and insulated from each other. When both conductors are driven by a different electric potential, positive charges ($+Q$) will collect in one end and negative charges ($-Q$) will collect in the other end [30] (see Figure 4.1); energy will then be stored in the electric field developed between the oppositely charged conductors. The charge that builds up is expressed as capacitance by Equation 4.1, where C is the capacitance, Q is the total charge stored at one of the conductors (the two conductors of a capacitor will balance each other with equal but opposite charges), and V is the voltage across the conductors of the capacitor [10].

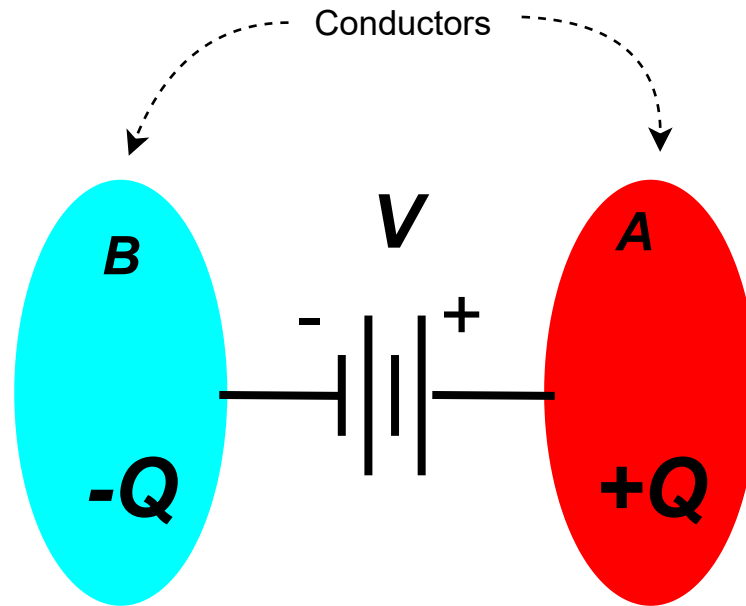


Figure 4.1: Two conductors that are separated in space will balance each other with equal but opposite charges when brought up to some arbitrary potential, forming a capacitor [10]

$$C = \frac{Q}{V} \quad (4.1)$$

Taking this definition into consideration, parasitic capacitance can then develop between two pads, two conductors, a conductor and an adjacent ground, or between any two elements that fulfill the criteria to build up charges [10]. Parasitic capacitance, or stray capacitance (C_s), impacts the self-resonant frequency (f_0) of a coil, above which the coil will not behave as an inductor anymore [31], but as a capacitor. Parasitic capacitance in coils can have adverse effects such as a change in the coil's impedance, a reduction of the quality factor, and a reduction in efficiency [32]. Knowing the value of the parasitic capacitance will allow predicting a more accurate compensation capacitance, predicting a potential over-voltage across the parasitic capacitor, and also knowing which would be the minimum required gap between terminals or if it is necessary to improve the electrical insulation of the wires.

A graphic representation of a three turns coil with parasitic capacitance can be seen in Figure 4.2; this model is not only considering the inductive effects, but also the capacitive effects that arise between the conductive elements. Taking Equation 4.2 as reference, where C is the capacitance, ϵ_0 is the permittivity of free space, ϵ_r the permittivity of the material between the conductors of the capacitor, A the area of the facing conductors, and d the distance between the conductors, we can state that the parasitic capacitances are heavily dependent on the geometry of the conductors and the distance between them; the value of the parasitic capacitance can be considerably high if the distance between the turns is short, or the area of the facing conductors is large [11]. Parasitic capacitances then create an electric connection between turns that are at different voltage levels [11]. Figure 4.3 shows the distributed model of the same three turns coil, including the parasitic capacitances. It can be seen from this circuit that, as happens with the coupled inductances L_{ij} , there are also coupled parasitic capacitances C_{ij} , nevertheless, the capacitances that will have the greater influence on the resonance frequency are the ones located in adjacent turns because of the dependence of the capacitance magnitude to the distance between the conductors [11]. Besides this, by looking at Equation 4.3 and Equation 4.4, where U_E is the electric energy stored at the capacitor's electric field, if the voltage across the parasitic capacitors is high enough, then the dielectric breakdown voltage of the wire's electric insulation could be reached, leading to the formation of electric arches or to electric discharges.

$$C = \frac{\epsilon_0 \epsilon_r A}{d} \quad (4.2)$$

$$U_E = \frac{1}{2}CV^2 \tag{4.3}$$

$$U_E = \frac{1}{2}QV \tag{4.4}$$

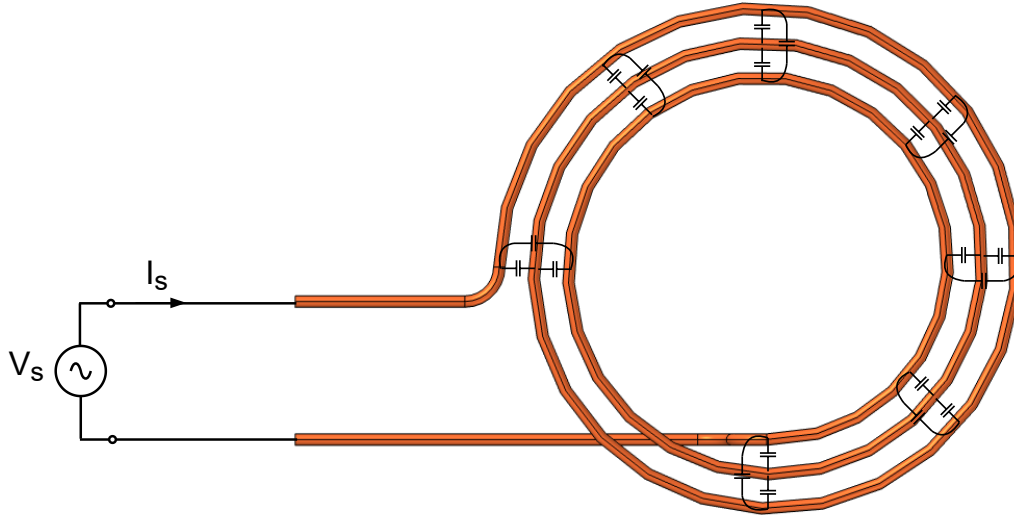


Figure 4.2: Three turn inductor with parasitic capacitances between turns [11]

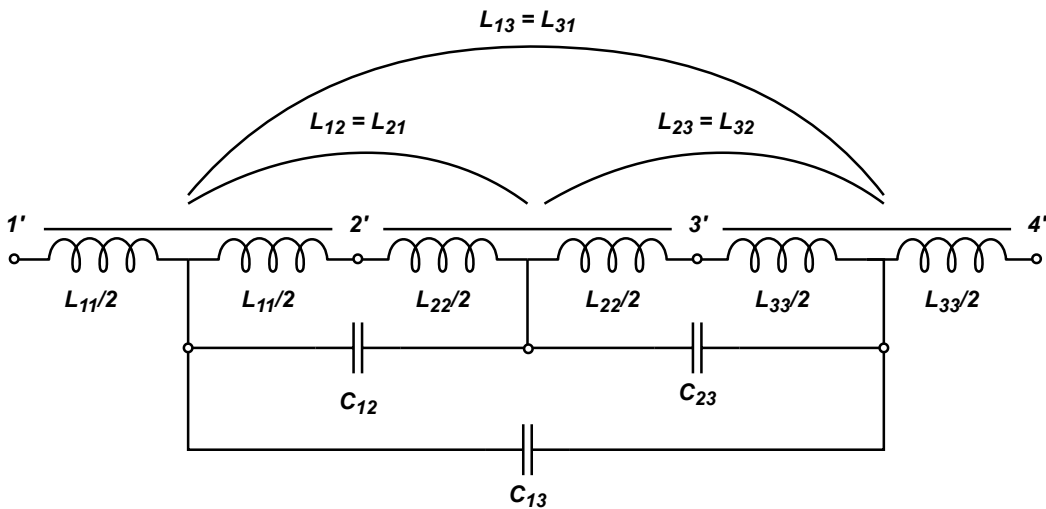


Figure 4.3: Distributed circuit model of an inductor with three turns [11]

The equivalent circuit of an IPT coil without parasitic capacitance can be expressed as in Figure 4.4(a), while the equivalent circuit of a coil considering the parasitic capacitance can be expressed as in Figure 4.4(b), where V_{coil} is the voltage at the coil's terminals, R is the resistance of the coil, L is the self-inductance of the coil, and C_s is the parasitic capacitance of the coil. The impedance (Z) of the circuit in Figure 4.4(b) can be expressed as in Equation 4.5, while the impedance phase angle (θ) for the same circuit can be expressed as in Equation 4.6, where X is the reactance of the coil.

$$Z = \frac{X_C(R + X_L)}{X_C + R + X_L} = \frac{\frac{1}{j\omega C_s}(R + j\omega L)}{\frac{1}{j\omega C_s} + R + j\omega L} = \frac{R + j\omega L}{1 + j\omega RC_s - \omega^2 LC_s} \tag{4.5}$$

$$\theta = \arcsin\left(\frac{X}{|Z|}\right) \quad (4.6)$$

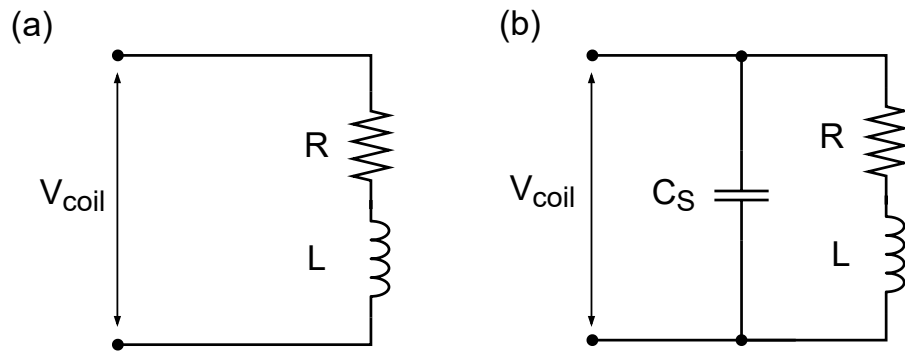


Figure 4.4: (a) Equivalent circuit of a coil without parasitic capacitance. (b) Equivalent circuit of a coil with parasitic capacitance

The self-resonance frequency (SRF) of an inductor is defined as the frequency at which resonance between the parasitic capacitance and the inductance takes place. In order to calculate the self-resonance frequency, also known only as resonance frequency (f_0), is possible to remodel the circuit in Figure 4.4(b) into the circuit shown in Figure 4.5. For this equivalent circuit, R_P and X_{L_P} can be expressed as in Equation 4.7 and Equation 4.8 [12].

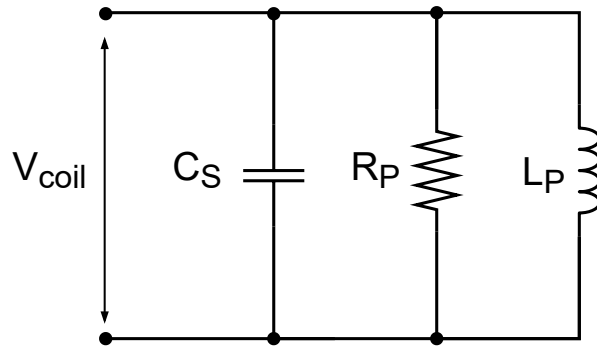


Figure 4.5: Inductor model showing parallel R and L equivalents [12]

$$R_P = \frac{R^2 + X_L^2}{R} \quad (4.7)$$

$$X_{L_P} = \frac{R^2 + X_L^2}{X_L} \quad (4.8)$$

In the equivalent circuit from Figure 4.5, the resonance happens when:

$$X_{C_S} = X_{L_P} \quad (4.9)$$

$$X_{C_S} = \frac{R^2 + X_L^2}{X_L} \quad (4.10)$$

$$\frac{1}{\omega C_S} = \frac{R^2 + (\omega L)^2}{\omega L} \quad (4.11)$$

$$\frac{L}{C_S} = R^2 + (\omega L)^2 \quad (4.12)$$

If we know that $\omega_0 = 2\pi f_0$, then, we can solve for f_0 as follows [33]:

$$\omega_0 = \sqrt{\frac{1}{LC_S} - \frac{R^2}{L^2}} \quad (4.13)$$

$$f_0 = \frac{1}{2\pi} \sqrt{\frac{1}{LC_S} - \frac{R^2}{L^2}} \quad (4.14)$$

Finally, the impedance at the resonance frequency (Z_0), that is, when $Z \angle 0$, can be expressed as follows:

$$Z_0 = \frac{L}{RC_S} \quad (4.15)$$

4.2. Methodology for parasitic capacitance evaluation

The methodology to evaluate the parasitic capacitance of the IPT coils can be summarized as follows:

1. Build the COMSOL setup (geometries, materials and mesh) of the active elements of the IPT charging pads.
2. Define the module, interface and features to be used for the COMSOL FEM simulation.
3. Run the FEM simulation and validate its results by comparing them with the measurements obtained by a Vector Network Analyzer (VNA) taken from a (real) prototype coil.
4. Once the COMSOL setup has been validated, obtain the impedance bode plots of the charging pads, by means of a COMSOL Electromagnetic Fields FEM simulation.
5. Obtain the values of the self-resonance frequency (f_0) and resonance impedance (Z_0) of the coils from the impedance bode plots.
6. Obtain the self-inductance (L) of the coils at the resonance frequency by means of a COMSOL Magnetic Fields FEM simulation.
7. From Equation 4.14 and Equation 4.15, solve for the AC resistance (R_{AC}) at the resonance frequency and the parasitic capacitance (C_S) of the coils.
8. With Equation 4.5 and Equation 4.6, obtain the impedance bode plots, and compare them with the ones obtained from the FEM simulation.
9. With *GeckoCircuits*, build the (virtual) equivalent circuit of the overall IPT charging system, including power electronics and compensation capacitance.
10. Obtain the voltage across the parasitic capacitors and the electric field strength, and evaluate for a potential over-voltage.
11. Perform an Electromagnetic Fields FEM simulation to analyze the location of the potential over-voltage.

The value of the parasitic capacitance can also be calculated analytically with Equation 4.2, nevertheless, this formula has to be modified since it also needs to account for the curvature of the wire, in other words, the formula can be rewritten as in Equation 4.16, where l is the length of the coil, r is the radius of the Litz wire, and $g(\theta)$ is the gap between the wires as a function of the angle θ (see Figure 4.6).

$$C = \frac{\epsilon_0 \epsilon_r A}{g} = 2 \int_0^{\frac{\pi}{2}} \frac{\epsilon_0 \epsilon_r}{g(\theta)} dA = 2 \int_0^{\frac{\pi}{2}} \frac{\epsilon_0 \epsilon_r l r}{g(\theta)} d\theta \quad (4.16)$$

$$g(\theta) = D + 2(r - r \cos(\theta)) \quad (4.17)$$

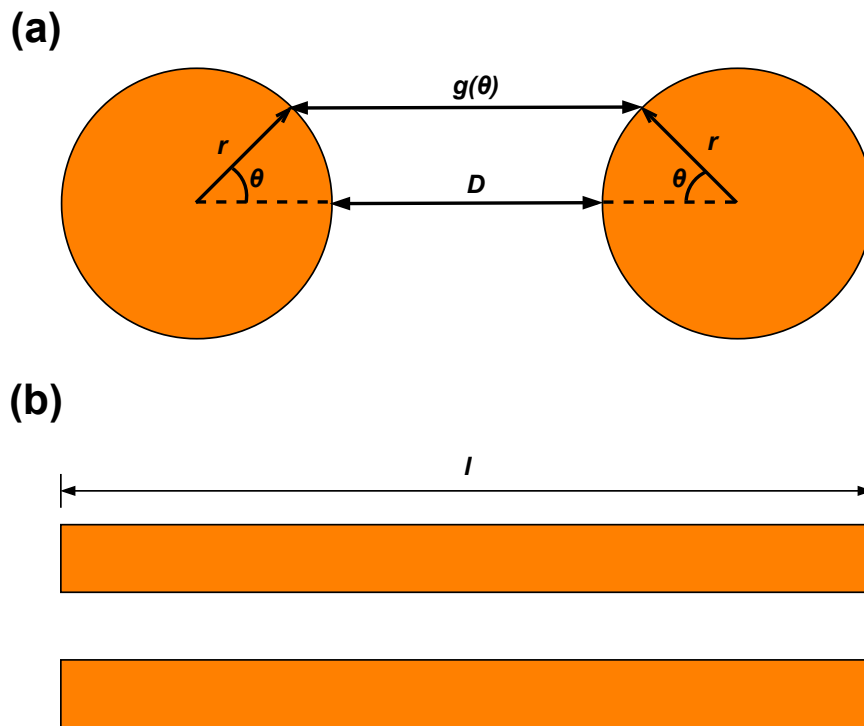


Figure 4.6: (a) Pair of Litz wires (front view). (b) Pair of Litz wires (top view)

4.3. COMSOL model setup

The setup for the FEM analysis was done at *COMSOL Multiphysics 5.6*. Since the FEM simulations to be done need to be validated by comparing the electromagnetic behavior of the simulated coil with the electromagnetic behavior of a real coil, the first COMSOL FEM simulation that was performed was that of the primary coil of the 20 kW IPT system described in [19], as this charging pad has already been physically built and is ready to be tested. The 3D model of that coil was created in *Solid Edge* (by using the same methodology shown in subsection 3.3.1), and then imported to COMSOL. The dimensions of the primary coil for the 20 kW IPT system can be seen in Table 4.1, which were also obtained from a multi-objective optimization study.

Table 4.1: Results of a multi-objective optimization study for the charging pads of a 20 kW IPT system [19]

Primary coil dimensions for a 20 kW IPT system		
Parameter	Value	Unit
Outer coil length	55.56	cm
Outer coil width	55.17	cm
Inner coil length	22.08	cm
Inner coil width	18.47	cm
Gap between turns	2.44	mm
Core length	51.53	cm
Core width	2.77	cm
Core height	2.88	cm
Number of cores	7	–
Gap between cores	3.13	cm
Shield length	55.17	cm
Shield width	51.56	cm
Gap between coil and cores	3.94	mm
Gap between cores and shield	1.06	cm
Coil turns	23	–

The ferrite cores and copper shield were designed directly in COMSOL, by using the 3D modeling features available in this program. The result can be seen in Figure 4.7. In regards to the material assignment, the coil and shield were set as copper, the ferrite cores as 3C95 (full the data-sheet of 3C95 ferrite can be found in [27]), and the surrounding medium as air. The main properties of the materials selected for this model are shown in Table 4.2. The meshing of the model was set as user-controlled instead as physics-controlled (which is the default option, being usually a tetrahedral mesh), since a proper user-defined mesh allows for a better and more efficient FEM analysis. For the coil, a sweep mesh was used. For the ferrite cores and the metal shield, a quadrangular mesh together with a sweep mesh were used. Finally, for the surrounding air, which for this case was settled up as a sphere around the pad elements, a tetrahedral mesh was used. The meshed elements can be seen in Figure 4.8, Figure 4.9, Figure 4.10 and Figure 4.11.

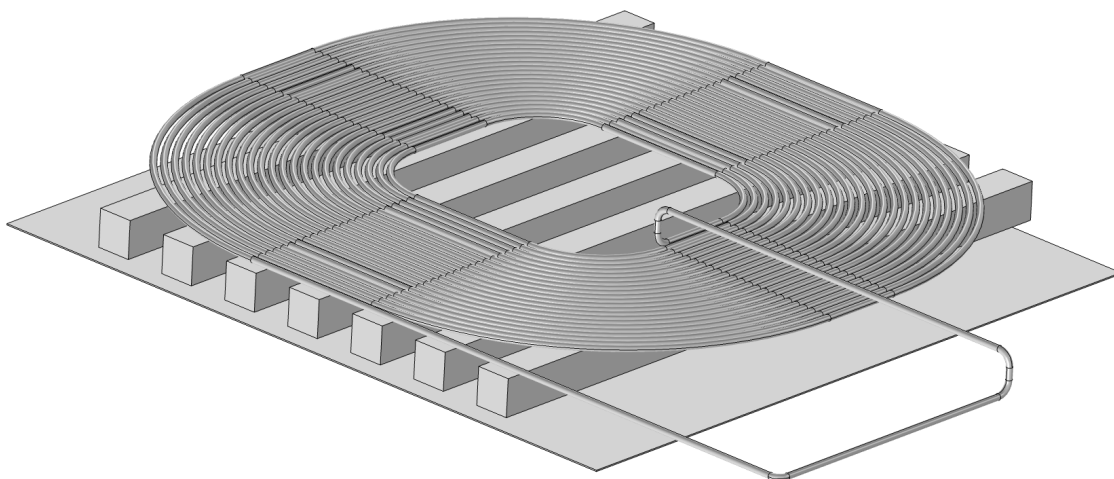


Figure 4.7: COMSOL setup (geometry) for a 20 kW IPT charging pad

Table 4.2: Electric and magnetic properties for the 20 kW setup materials

	Air	Copper	3C95	
Relative permeability	1	1	4500	–
Relative permittivity	1.0006	1	1	–
Electrical conductivity	5.6e-12	5.97e7	3.774	[S/m]

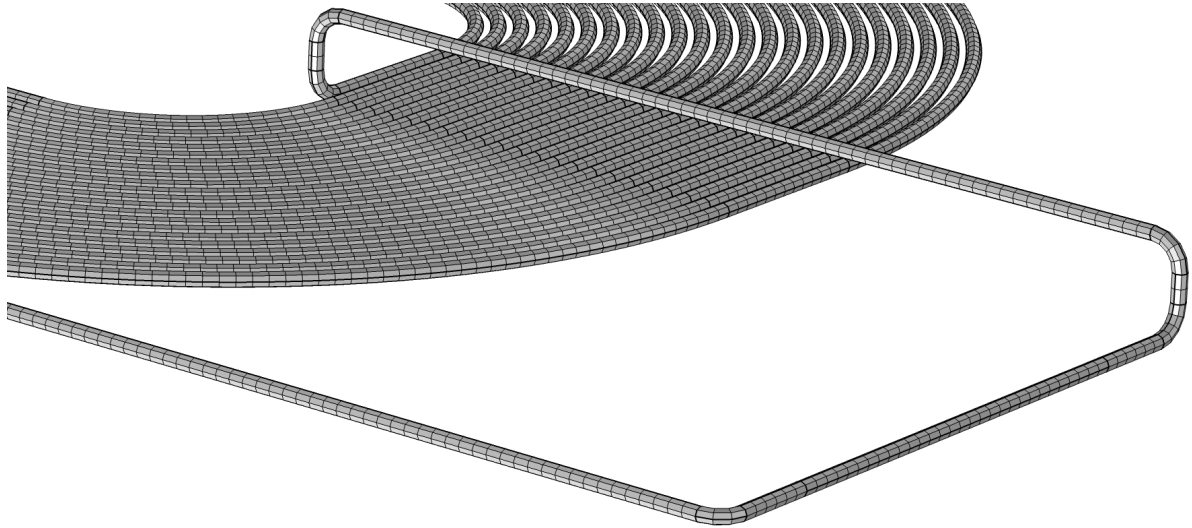


Figure 4.8: Primary coil meshing for the 20 kW COMSOL setup

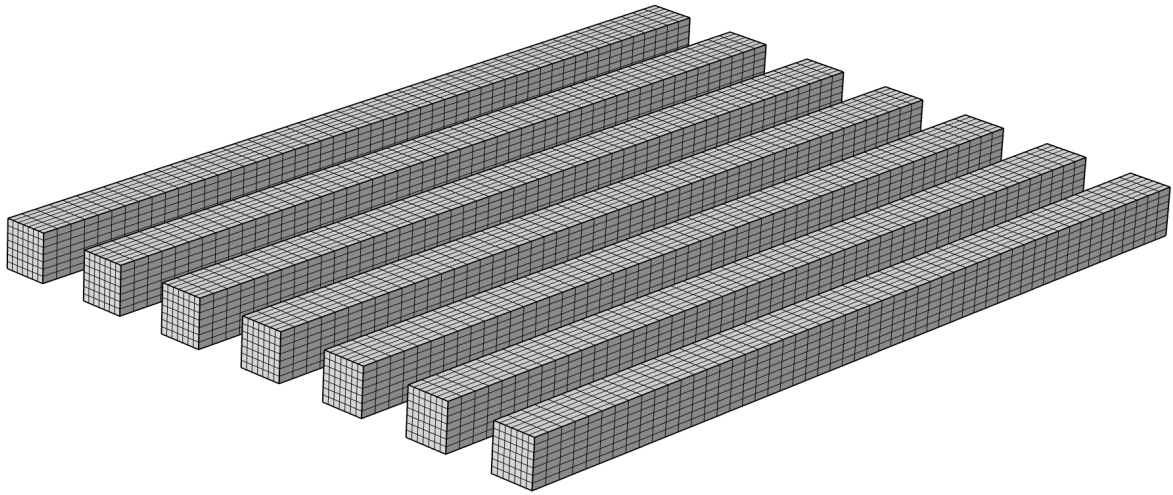


Figure 4.9: Cores meshing for the 20 kW COMSOL setup

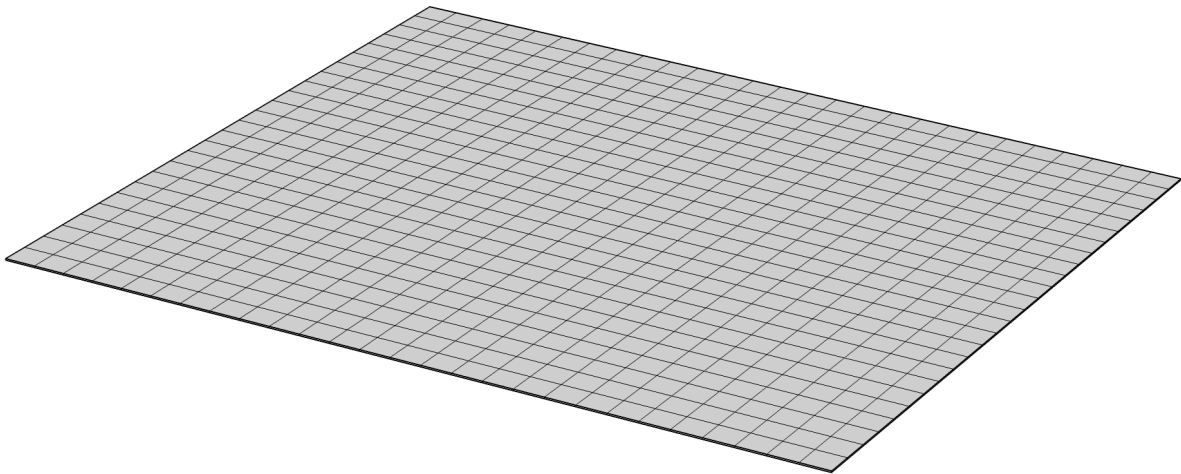


Figure 4.10: Metal shield meshing for the 20 kW COMSOL setup

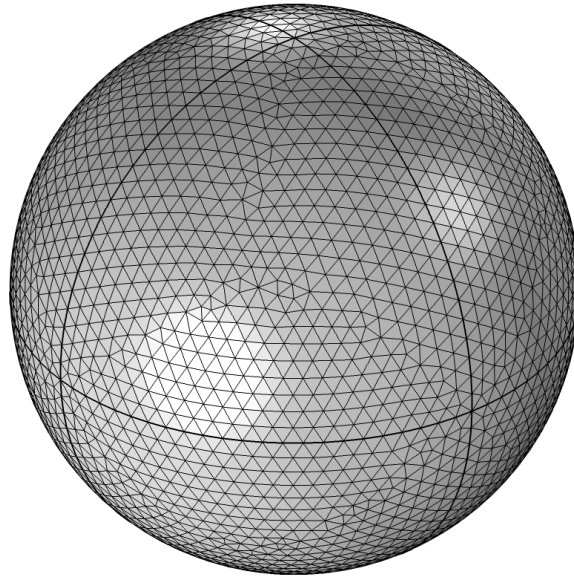


Figure 4.11: Surround air meshing for the 20 kW COMSOL setup

4.4. Module, interface and features selection for the COMSOL FEM simulation

Next step was selecting the module, interface and features to be used for a proper electromagnetic FEM simulation in COMSOL. For this matter, the diagram shown in Figure 4.12 was used. This diagram can be found in the *COMSOL Learning Center Resources* webpage, inside the *Modeling Electromagnetic Coils* section found in [34]. The required module to perform the electromagnetic modeling of a coil is the *AC/DC* module. Inside this module, as can be seen in Figure 4.12, the required interface is the *Magnetic Fields (MF)* interface, since we will be working in the resonating regime. The suggested features for the simulation are the *Lumped Port* and *Impedance Boundary*. The *Impedance Boundary* feature neglects the inner body of the wire, and instead considers only the surface of the wire for the simulation; this feature is used mainly for two reasons: (1) Because it is assumed that the current in the wire will only flow at the surface due to the skin effect present at high frequencies, and (2) Because this reduces the computational effort to run the simulation. Despite this, since we will be using Litz copper wire instead of a solid copper wire, the skin effect will be reduced (meaning that the skin depth (δ) will not be much lower (\ll) than the wire's radius (r)), and so, in the simulation, the inner body of the wire can not be neglected. For this reason, the *Impedance Boundary* feature will not be used. It is important to mention that we are also not supposed to use the *RF* (Radio Frequency) module since the coils are not considered to be in the radiating regime. By looking at Equation 4.18, where v is the speed of light, and f is the operation frequency (in this case, the resonance frequency (f_0)), we can estimate that the wavelength of the electromagnetic fields produced by the coils (assuming a resonance frequency of 10 MHz) is close to 30 meters; this value is way longer than the surrounding environment defined for the simulation. The reason the surrounding environment can be reduced to a relatively small space is because most of the electromagnetic flux will be contained by the ferrite cores and metal shields, this will be demonstrated in the next subsection.

$$\lambda = \frac{v}{f} \quad (4.18)$$

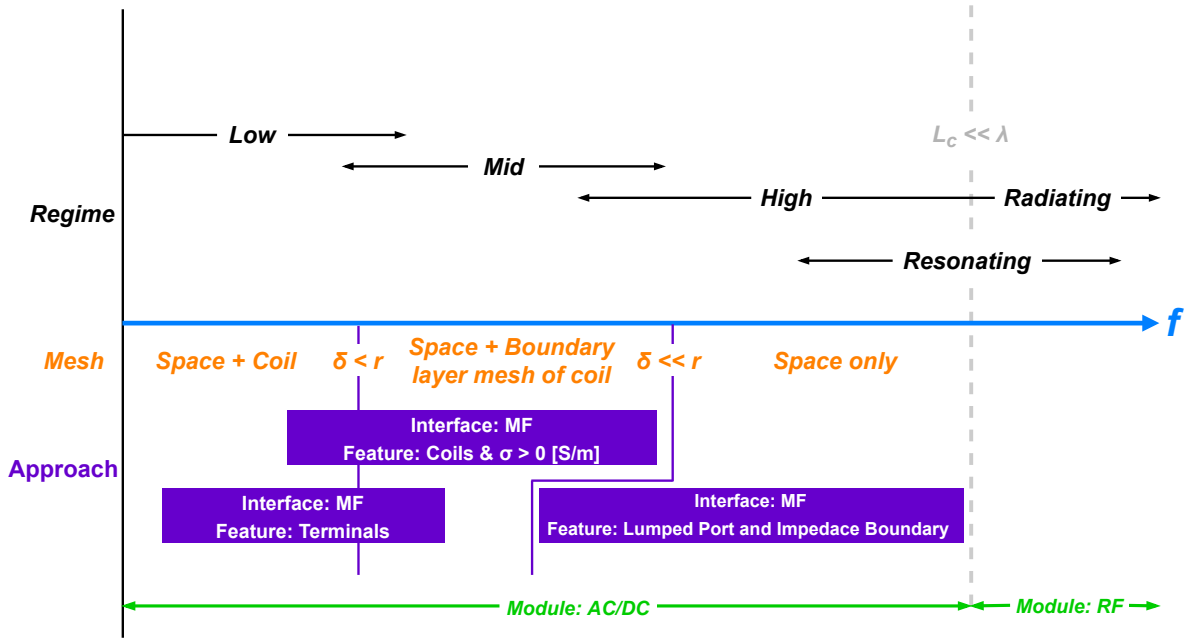


Figure 4.12: Varying approaches over frequency for volumetric coils [13]

A brief explanation of the *Lumped Port* feature will be given next: This feature is used to model a voltage or current source applied between two electrodes [14]. This port must be placed between two metallic boundaries that are separated by a distance much smaller than its electromagnetic wavelength. This port calculates the impedance (Z_{port}), given by Equation 4.19, where V_{port} is the voltage across the port terminals, and I_{port} is the averaged total current over all the cross-sections parallel to the port terminals [14]. The lumped port provides an interface between the voltages/currents and the electric/magnetic fields, so, the voltage is obtained from the electric field line integral between the terminals averaged over the whole port, as shown in Equation 4.20, where h is the distance between the terminals, a_h is the unity vector specifying the electric field direction, and E is the electric field (see Figure 4.13 for reference). On the other hand, the current can be expressed with a surface current (J_S) at the lumped port boundary opposite to the electric field direction. Equation 4.21 can be used to calculate the current from the current density, where the integration is done along the width (w) of the ports in the direction $a_h \times n$.

$$Z_{port} = \frac{V_{port}}{I_{port}} \quad (4.19)$$

$$V_{port} = \int_h E \cdot dl = \int_h (E \cdot a_h) dl \quad (4.20)$$

$$I_{port} = \int_w (n \times J_S) \cdot dl = - \int_w (J_S \cdot a_h) dl \quad (4.21)$$

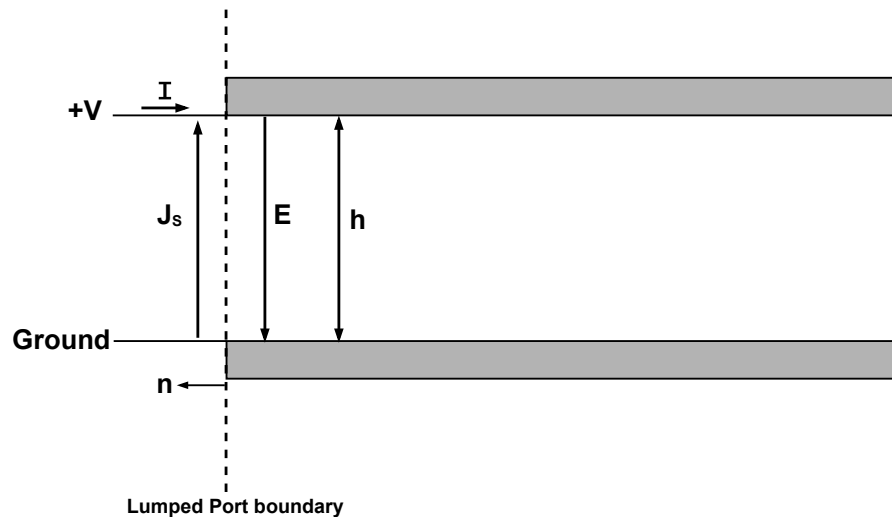


Figure 4.13: Lumped port graphic representation [14, p. 102]

It can be seen that the *Lumped Port* feature will allow us to calculate the impedance between the coil terminals, nonetheless, if we only need to calculate the inductance of the coil, the *Coil* feature can be used. This feature models a conductive body like a wire, a busbar, or another metallic conductor where the current flows freely due to the material's conductivity, and it can be used to simplify electromagnetic models [14]. Since the impedance is not calculated with this feature, it will only be used to obtain the inductance of the coils.

4.5. COMSOL model validation

Now that the underlying equations of the FEM simulation features are understood, it is possible to perform the simulations and then compare the results with the measurements taken from a real 20 kW IPT coil, but first, it is important to mention the following considerations:

- i. The mesh size used for the pad elements was coarse enough to have a simulation feasible to be performed, considering the available time and computational resources.
- ii. The *Infinite Elements* (IE) feature that allows simulating an infinite surrounding environment (highly recommended) was not used, since it demands very high computational resources; instead, a big enough sphere (that is magnetically insulated) that emulates the surrounding air was used. It will be demonstrated that both the IE and the sphere show similar results, mainly because the electromagnetic flux is contained by the ferrite cores and metal shields.
- iii. The wires in the simulation will experience a high skin effect, since it is not possible to model a Litz wire in COMSOL due to its high complexity. For this reason, the results may not be completely accurate. Modeling a Litz wire in COMSOL will be proposed as future work on this thesis.

With respect to point (ii) from the previous list, one simulation was done with the *IE* feature and another simulation was done with the magnetically insulated sphere. The magnetic flux in the stationary state (DC excitation) for both of these tests are shown in Figure 4.14 and Figure 4.15 respectively. Table 4.3 shows that the main magnetic and electric parameters are very similar in both cases, where the error is displayed at the right of the table. Besides this, as mentioned in point (ii) as well, it can be seen from Figure 4.16 and Figure 4.17 that most of the magnetic flux is actually contained inside of the ferrite cores, and also confined by the metal shields. For these reasons: the fact that the results don't differ considerably between the *IE* surrounding and the insulated sphere, the fact that the computational time is substantially lower without the *IE* feature, and the fact that most of the magnetic flux remains close

to the pad's elements, we will only consider the insulated sphere as the surrounding environment for the next experiments.

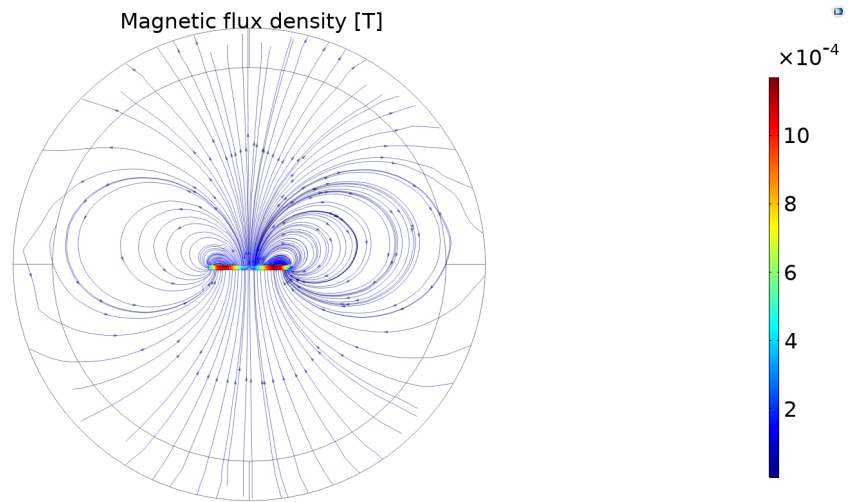


Figure 4.14: Magnetic flux in simulation with Infinite Elements surrounding

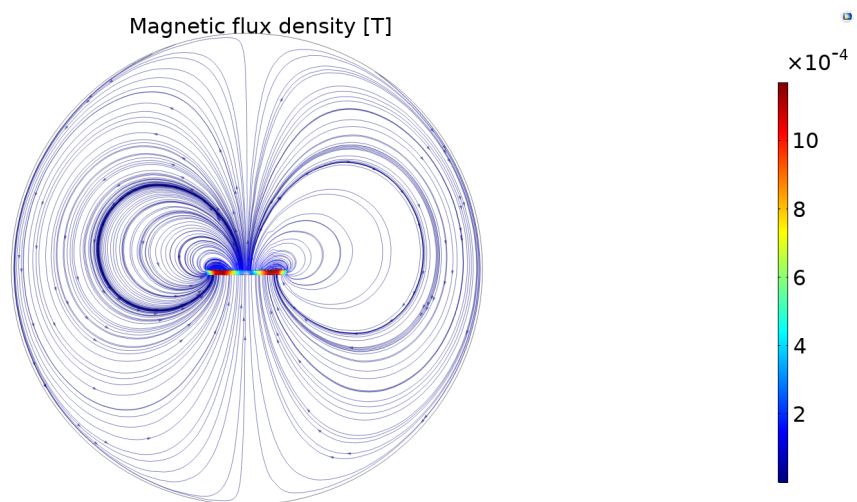


Figure 4.15: Magnetic flux in simulation with magnetically insulated sphere

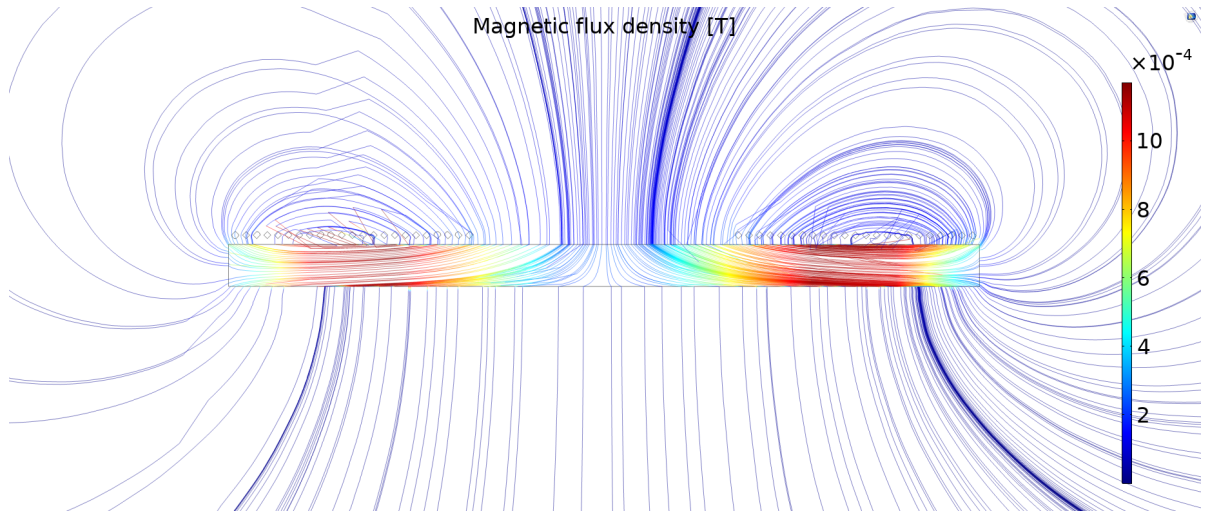


Figure 4.16: Magnetic flux considering ferrite cores (without metal shielding)

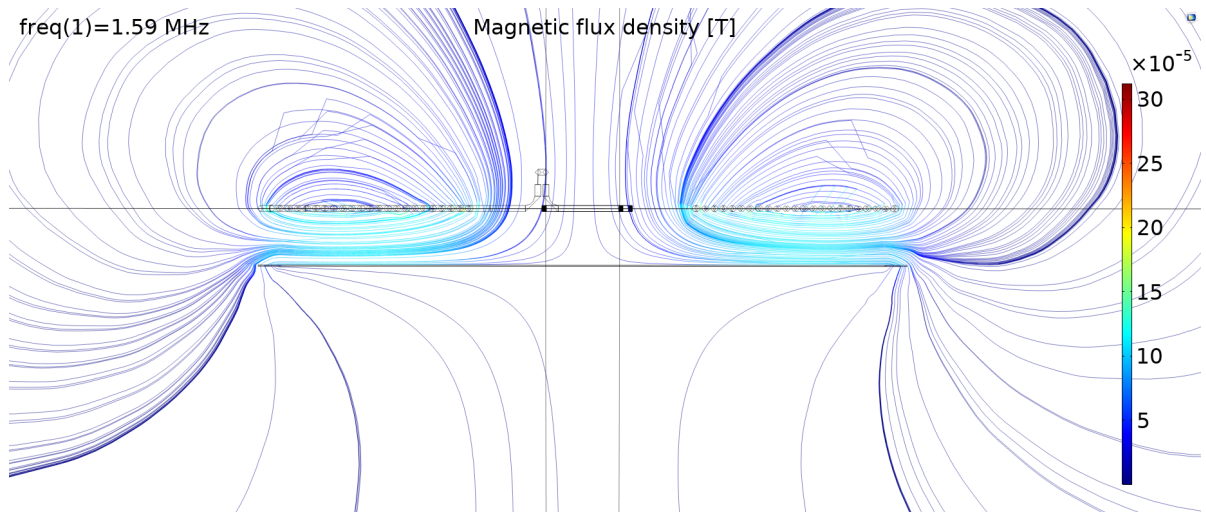


Figure 4.17: Magnetic flux with metal shielding at resonance frequency (without cores)

Table 4.3: Electric and magnetic parameters for simulation with and without Infinite Elements surrounding

	Without IE	With IE	Error
Inductance (L)	374.7 μH	386.3 μH	2.98 %
Coil resistance (R_{DC})	36 m Ω	35.9 m Ω	0.055 %
Voltage (V)	36 mV	35.9 mV	0.055 %
Electric energy (W_e)	2.67×10^{-21} J	2.66×10^{-21} J	0.052 %
Magnetic energy (W_f)	0.161 mJ	0.162 mJ	0.17 %

Now, it is possible to perform the simulations. In order to run the Electromagnetic Fields FEM simulation, the excitation at the lumped port was set at 1 A, in a frequency spectrum ranging from 1 to 5 MHz. It can be seen from Figure 4.18 that the resonance impedance (Z_0) is around 298.15 k Ω , and the self-resonance frequency (f_0) close to 1.6 MHz. Then, the self-inductance of the coil (L) is calculated with the *Coil* feature. This feature will account only for the inductive, and not the capacitive, effect of the coil (thus, this can be called a Magnetic Fields FEM simulation), and so the self-inductance values are provided directly by the COMSOL results. The self-inductance was evaluated in the same frequency span, where its value at the resonance frequency is around 306.86 μH , as seen in Figure 4.19.

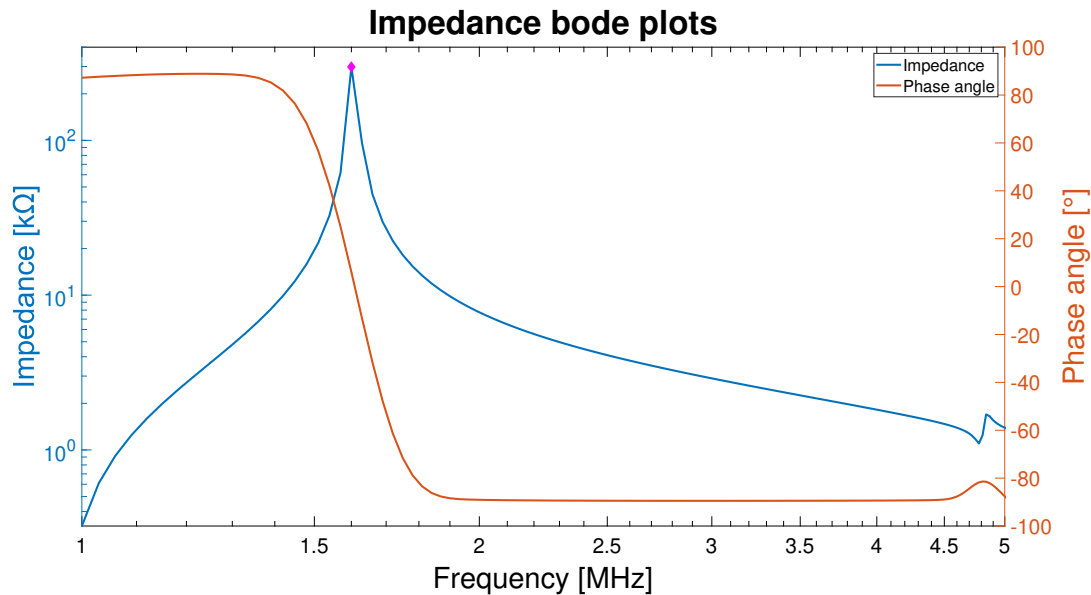


Figure 4.18: Impedance bode plot for the 20 kW primary IPT pad

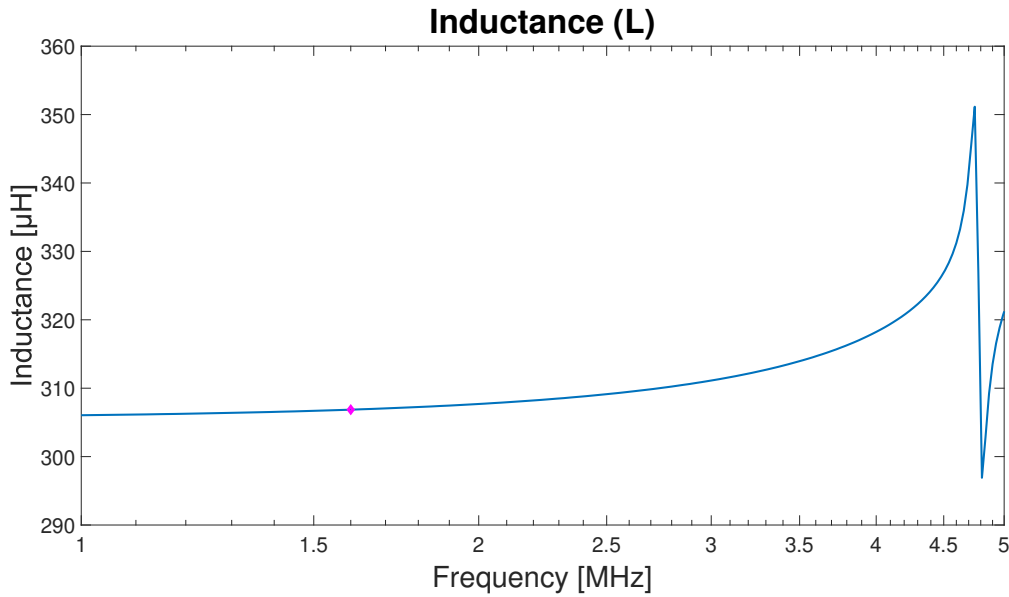


Figure 4.19: Coil inductance for the 20 kW primary IPT pad

After obtaining the resonance frequency (f_0), the resonance impedance (Z_0), and the coil inductance (L), it's also possible to obtain the AC resistance (R_{AC}) at the resonance frequency and the parasitic capacitance (C_S) of the coil by solving for those two parameters from Equation 4.14 and Equation 4.15. The solutions from solving such equations are 31.92Ω for the AC resistance at the resonance frequency and 32.24 pF for the parasitic capacitance. The values obtained from the FEM simulation and the equations can be seen in Table 4.4, and the equivalent circuit of the coil can be seen in Figure 4.20. The impedance bode plots can also be created by using these results in Equation 4.5 and Equation 4.6; the impedance bode plot obtained by this method can be seen in Figure 4.21, while the comparison between the FEM simulation bode plot and the bode plot obtained from Equation 4.5 can be seen in Figure 4.22.

Table 4.4: Results for the 20kW IPT primary coil FEM simulation taken at the resonance frequency

	Value	Unit
Resonance frequency (f_0)	1.6	MHz
Resonance impedance (Z_0)	298.15	k Ω
Coil inductance (L)	306.86	μH
AC resistance (R_{AC})	31.92	Ω
Parasitic capacitance (C_S)	32.24	pF

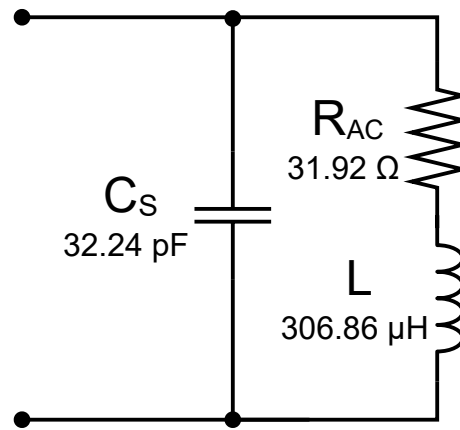


Figure 4.20: Equivalent circuit of the 20 kW primary IPT coil with parameters (R_{AC} is taken at the resonance frequency).

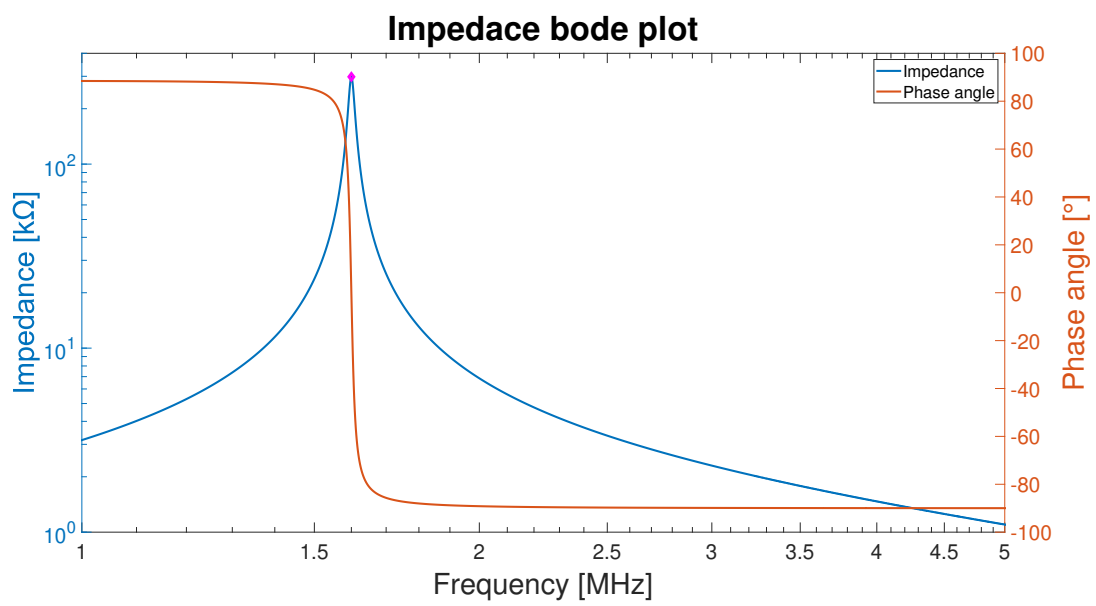


Figure 4.21: Impedance bode plot for the 20 kW IPT system using equivalent circuit equations

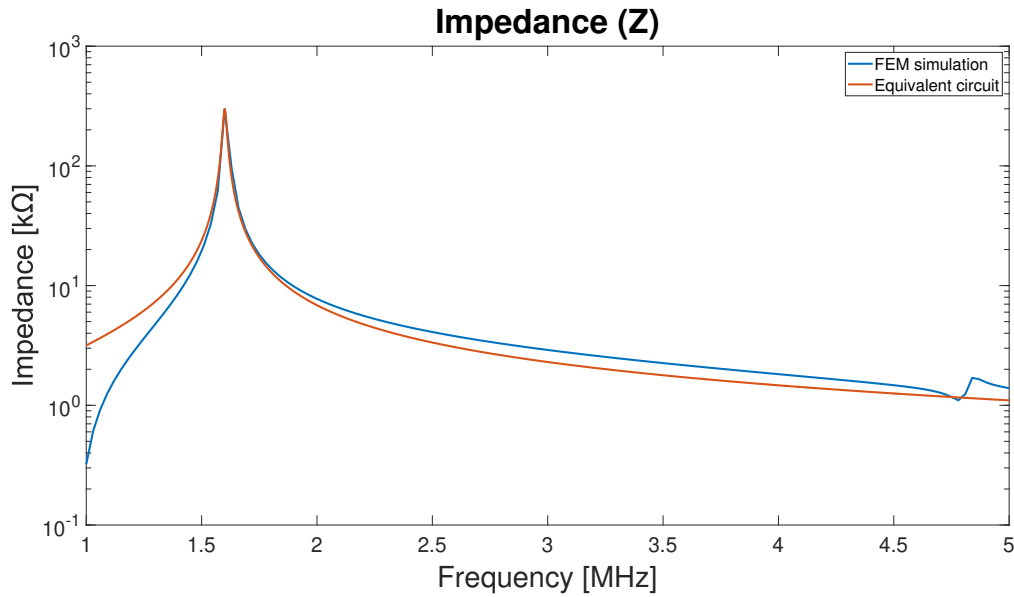


Figure 4.22: Comparison between the FEM simulation bode plot and the bode plot obtained from equation Equation 4.5

After obtaining the results from the FEM simulations, it is now required to do the measurements for the real 20 kW IPT primary coil described in [19] by means of a VNA tool. This tool measures, among many other parameters, the coil impedance (Z), the impedance phase angle (θ), and the inductance of the coil (L). These values can then be plotted with the aid of a *Matlab* code to obtain the impedance bode plots and the inductance of the coil in the frequency domain. The plots can be seen in Figure 4.23, Figure 4.24 and Figure 4.25. The VNA shows that the 20 kW IPT primary pad has a resonance impedance of around 208.07 kΩ, a resonance frequency of 1.275 MHz, and a coil inductance that can be rounded to a value close to 359 μ H. The values from the FEM simulation and the VNA measurements are compared in Table 4.5, and the impedance bode plots obtained from the FEM simulation and the VNA tool are compared in Figure 4.26.

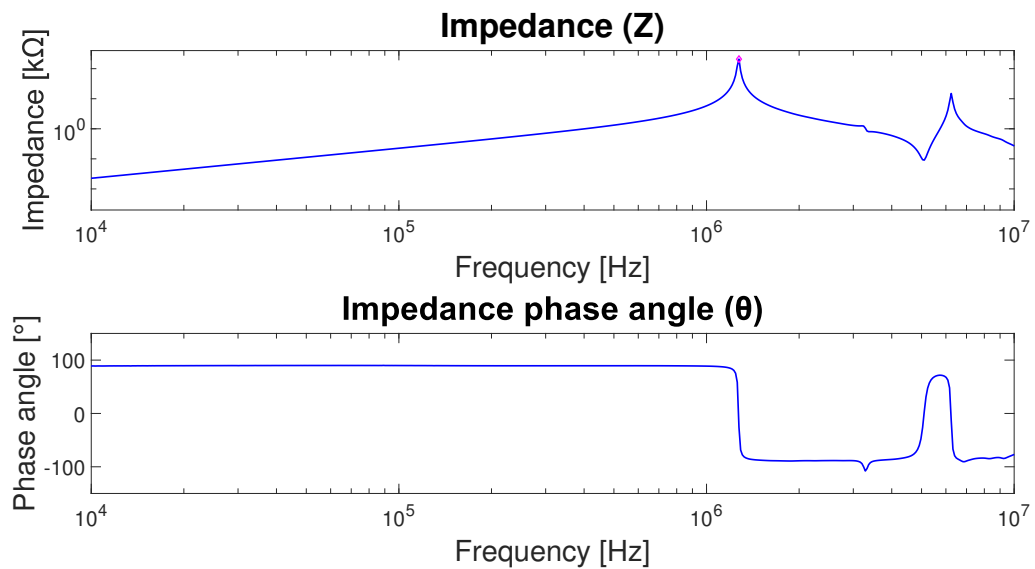


Figure 4.23: Impedance bode plots for the 20 kW primary IPT pad measured by the VNA

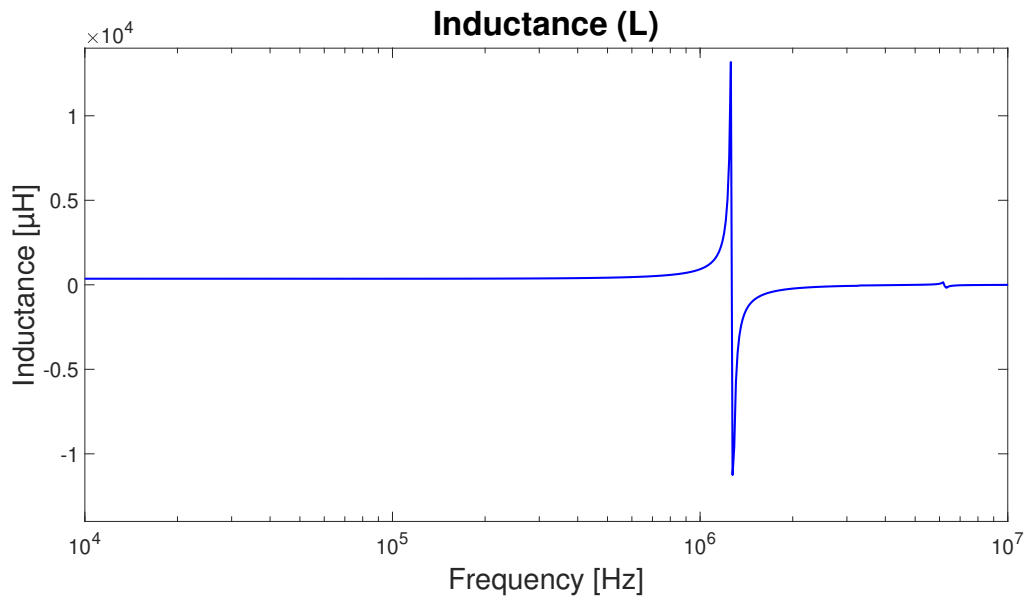


Figure 4.24: 20 kW primary IPT pad inductance measured by the VNA

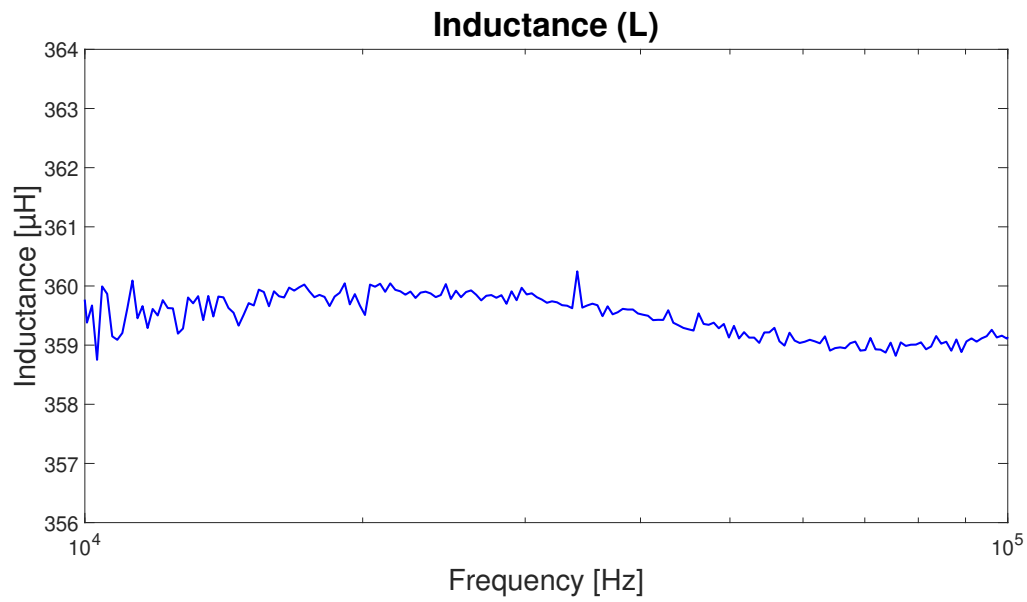


Figure 4.25: 20 kW primary IPT pad inductance measured by the VNA (Zoom-in)

Table 4.5: Comparison between FEM simulation results and VNA measurements for the 20 kW IPT primary pad

	VNA Measurement	FEM Simulation
Resonance impedance (Z_0)	208.06 k Ω	298.15 k Ω
Resonance frequency (f_0)	1.275 MHz	1.6 MHz
Coil inductance (L)	359 μ H	306.86 μ H
AC resistance (R_{AC})	39.76 Ω	31.92 Ω
Parasitic capacitance (C_S)	43.4 pF	32.24 pF

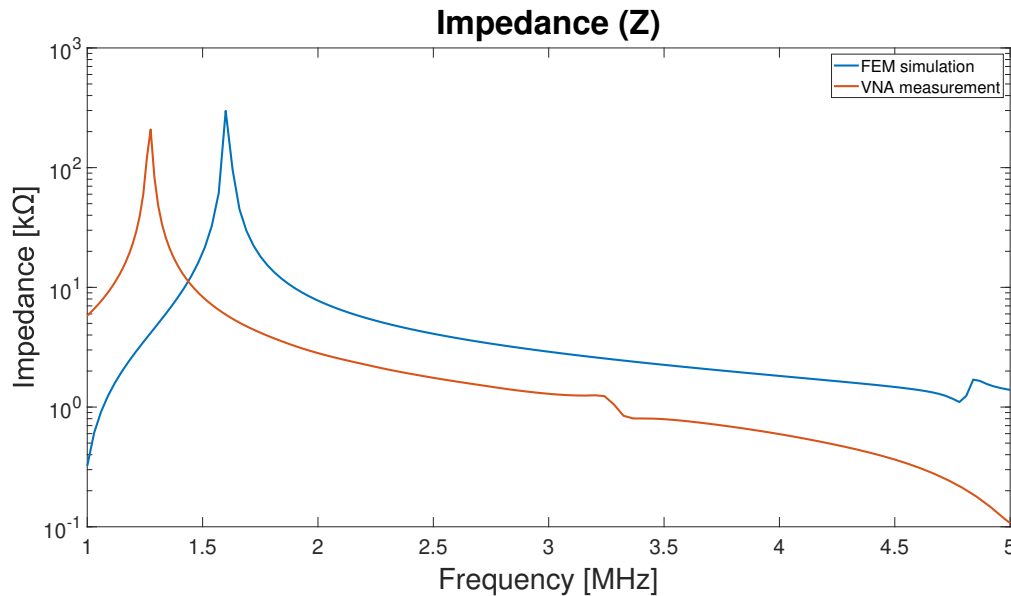


Figure 4.26: Comparison of the impedance bode plots obtained from the FEM simulation and the VNA measurements

It can be concluded from Table 4.5 that the results obtained from the FEM simulation are relatively similar to the ones obtained from the VNA measurements. The difference between these two sets of results exists due to a series of reasons, the main ones being:

- 1) The used mesh size is not fine enough to obtain the most accurate results from the FEM simulation.
- 2) The Litz wire has not been modeled in COMSOL, which changes the AC resistance of the wire and its inductance.
- 3) The magnetically isolated sphere that surrounds the IPT coil in the FEM simulation changes the real magnetic flux path, changing the actual inductance of the coil.
- 4) The frequency step used for the frequency domain FEM simulations is not small enough to reflect the exact results.
- 5) The ferrite cores real geometry and material properties are not entirely captured by the FEM simulation setup, these values are essentially idealized.
- 6) The actual geometry of the coil is not entirely captured by the FEM simulation setup, these values are essentially idealized.
- 7) The surrounding environment in the simulation differs from the surrounding where the real measurements were taken, the surrounding from the simulation is essentially idealized.

4.6. Electromagnetic Fields FEM simulation

Once the COMSOL setup has been validated, the next step is to make the simulation for the 50 kW IPT charging pads described in chapter 3. The methodology to build the COMSOL model setup is the same used for the 20 kW primary IPT pad described in section 4.3. The model setup can be seen in Figure 4.27 and Figure 4.28. It can be seen from these images that, for this case, both the primary and secondary coils were modeled in the program, with their respective ferrite cores and metal shields.

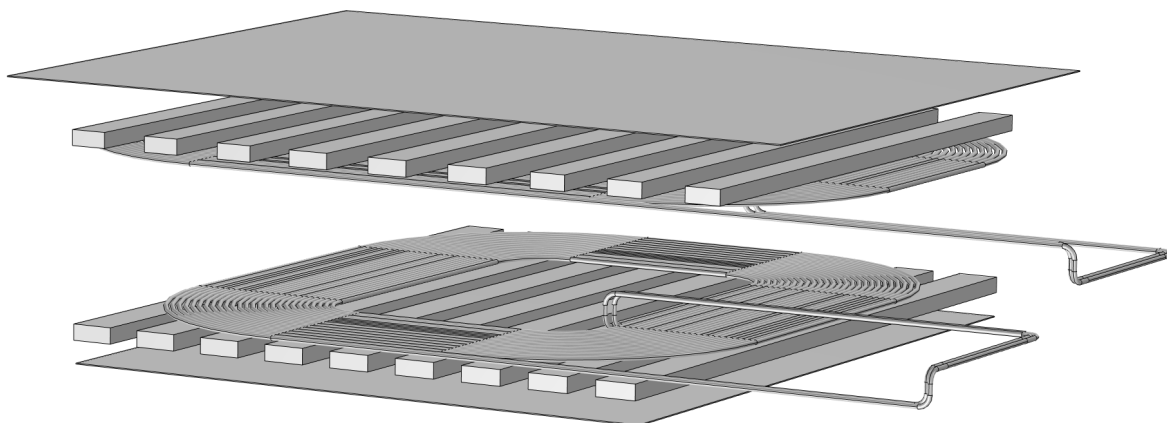


Figure 4.27: COMSOL model setup for the 50 kW IPT charging pads

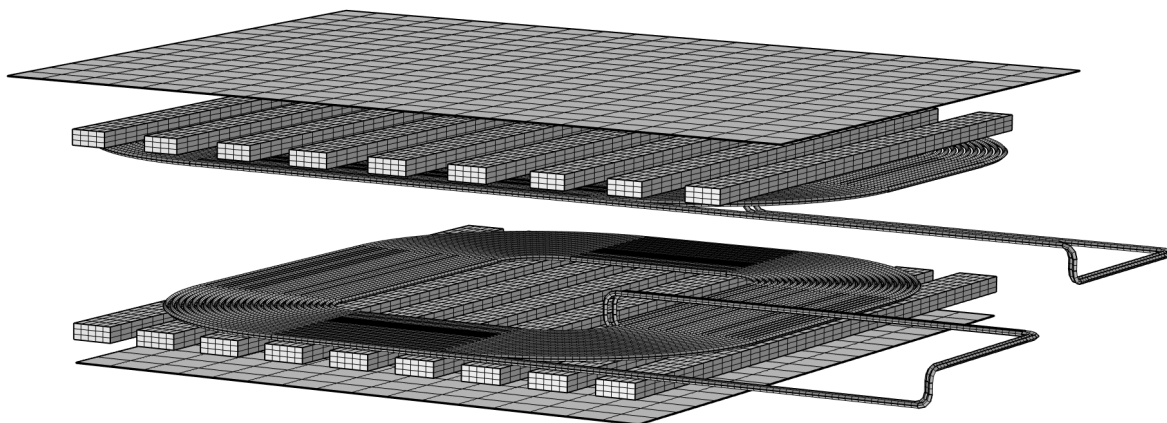


Figure 4.28: COMSOL model setup for the 50 kW IPT charging pads (including the mesh)

With the *Lumped Port* feature, the impedance bode plot for the 50 kW IPT primary and secondary charging pads were obtained. The results can be seen in Figure 4.29 and Figure 4.30 respectively. The (first) self-resonance frequency (f_0) for both the primary and secondary pads is 1.46 MHz, while their (first) resonance impedance (Z_0) are 287.94 k Ω and 191.62 k Ω respectively. It is important to note that, for the simulation of the 50 kW IPT system, we see two peaks in the bode plots, while we only see one peak in the simulation for the 20 kW IPT system, the reason for this is because, as mentioned before, both coils were included in the FEM simulation of the 50 kW system, while only one coil was modeled in the 20 kW system. With respect to the 50 kW IPT FEM simulation, when one of the coils is analyzed, the other one is left as an open circuit; still, the magnetic flux created by the analyzed coil will induce a voltage in the elements of the other coil (and so electric fields will manifest). This will be

evidenced as a second resonance frequency. The electric fields in the simulations will be depicted in section 4.8. For the simplicity of the analysis, in this thesis, we will focus only on the first resonance frequency.

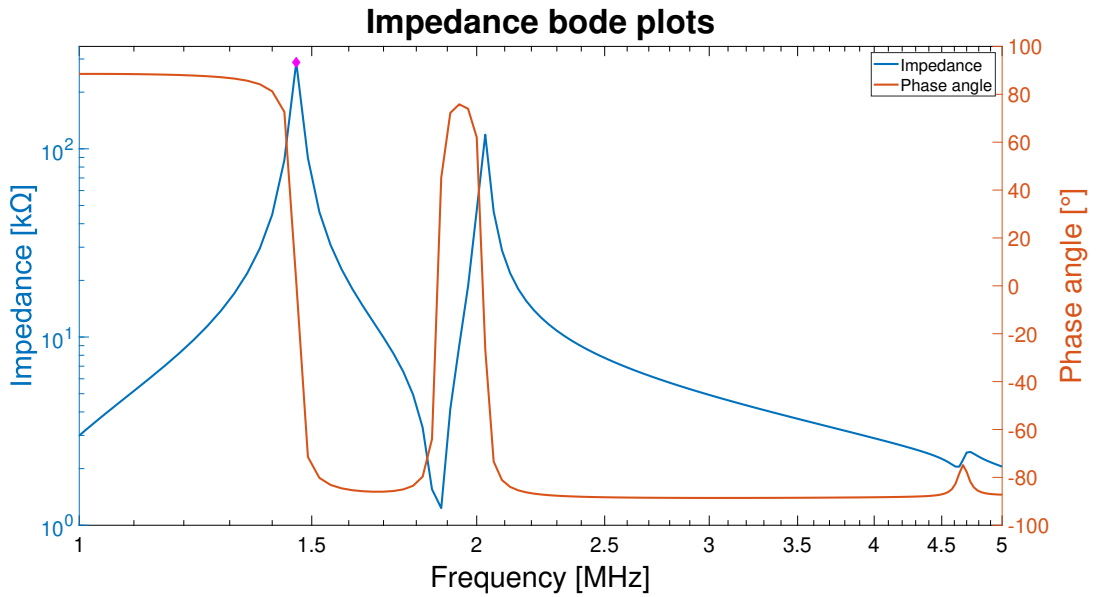


Figure 4.29: Impedance bode plot for the 50 kW IPT primary pad obtained from the FEM simulation

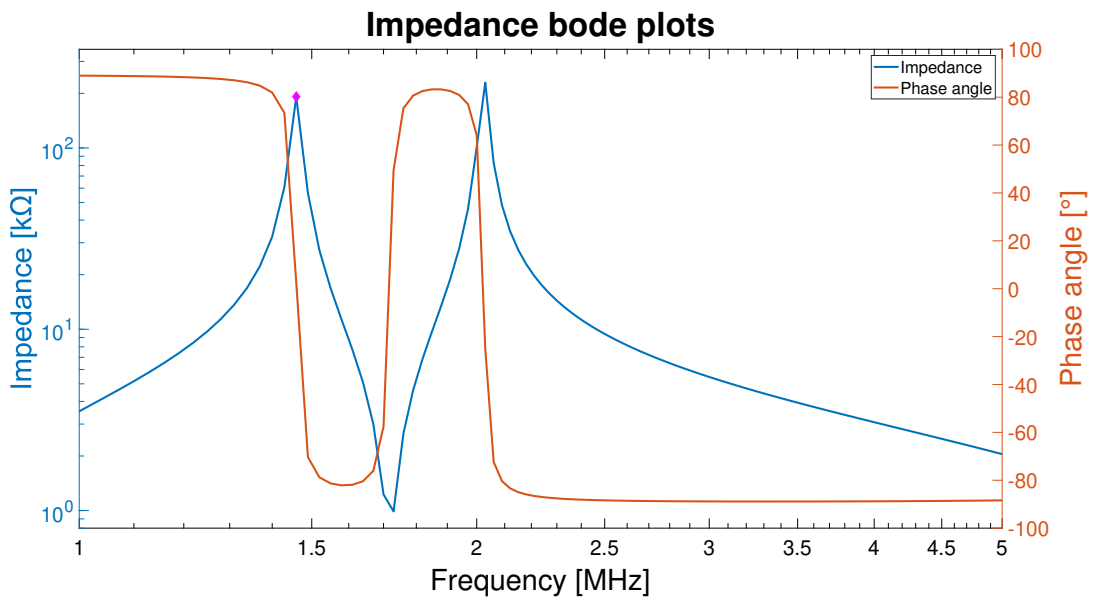


Figure 4.30: Impedance bode plot for the 50 kW IPT secondary pad obtained from the FEM simulation

After completing the Electromagnetic Fields FEM simulation for the 50 kW IPT pads, a Magnetic Fields FEM simulation was performed with the *Coil* feature in order to obtain the inductance (L) of the coils. The values for this parameter are $169.75 \mu\text{H}$ and $152.75 \mu\text{H}$ for the primary and secondary coils respectively.

4.7. Parasitic capacitance derivation

With the parameters calculated in the previous sections it is possible to solve for the AC resistance (R_{AC}) at the resonance frequency and the parasitic capacitance (C_S) of both circuits from Equation 4.14 and Equation 4.15. The AC resistances at the resonance frequency for the primary and secondary coils are 8.42Ω and 10.25Ω respectively, while their parasitic capacitances are 70 pF and 77.79 pF respectively. Table 4.6 shows the calculated parameters of both coils, while Figure 4.31 shows the equivalent circuits of the coils including their parasitic capacitances.

Table 4.6: Derived values for the primary and secondary coils taken at the resonance frequency

	Primary	Secondary
Resonance frequency (f_0)	1.46 MHz	1.46 MHz
Resonance impedance (Z_0)	287.94 k Ω	191.62 k Ω
Coil inductance (L)	169.75 μH	152.75 μH
AC resistance (R_{AC})	8.42 Ω	10.25 Ω
Parasitic capacitance (C_S)	70 pF	77.79 pF

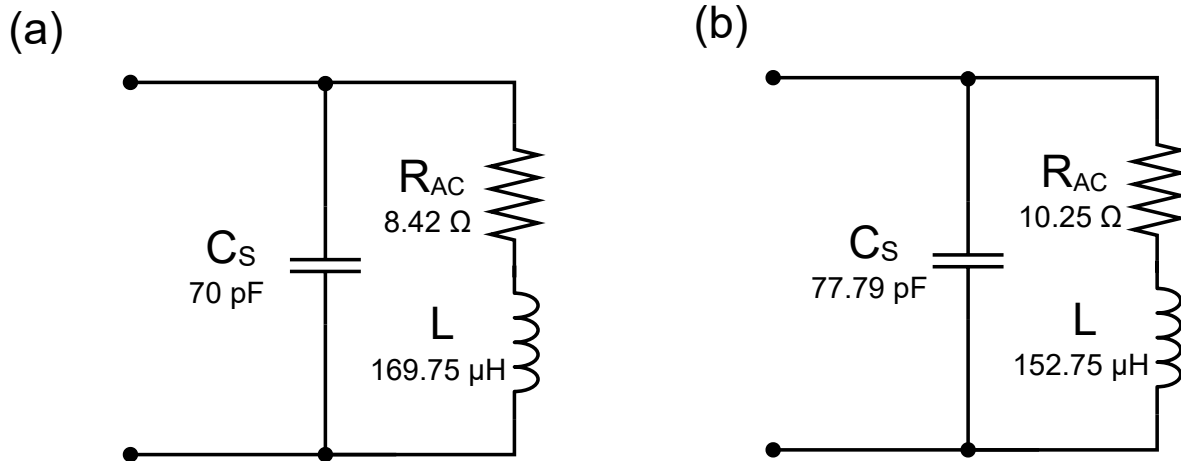


Figure 4.31: (a) Equivalent circuit of the 50 kW IPT primary coil. (b) Equivalent circuit of the 50 kW IPT secondary coil

With the inductance of the coils (L), the AC resistances (R_{AC}) at the resonance frequency, and the parasitic capacitance (C_S), it is now also possible to obtain the impedance bode plots by using Equation 4.5 and Equation 4.6. The comparison between the impedance bode plots obtained from the FEM simulation and the ones obtained from Equation 4.5 can be seen in Figure 4.32 and Figure 4.33 for the primary and secondary coils respectively. It is important to mention that the bode plots from the equivalent circuit were derived considering only the first resonance frequency.

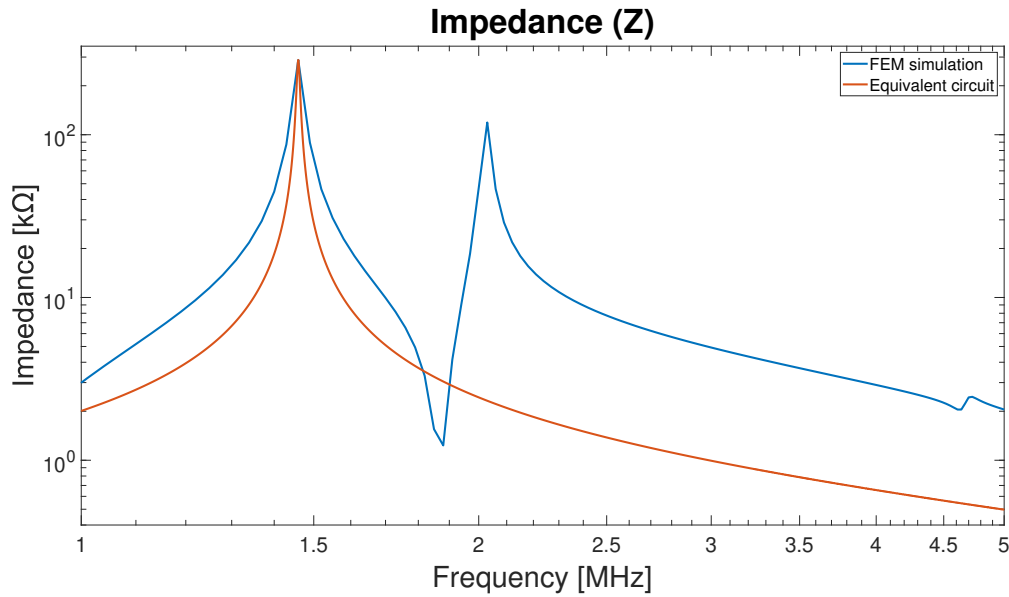


Figure 4.32: Comparison between the FEM simulation bode plot and the bode plot obtained from equation Equation 4.5 for the primary 50 kW IPT coil

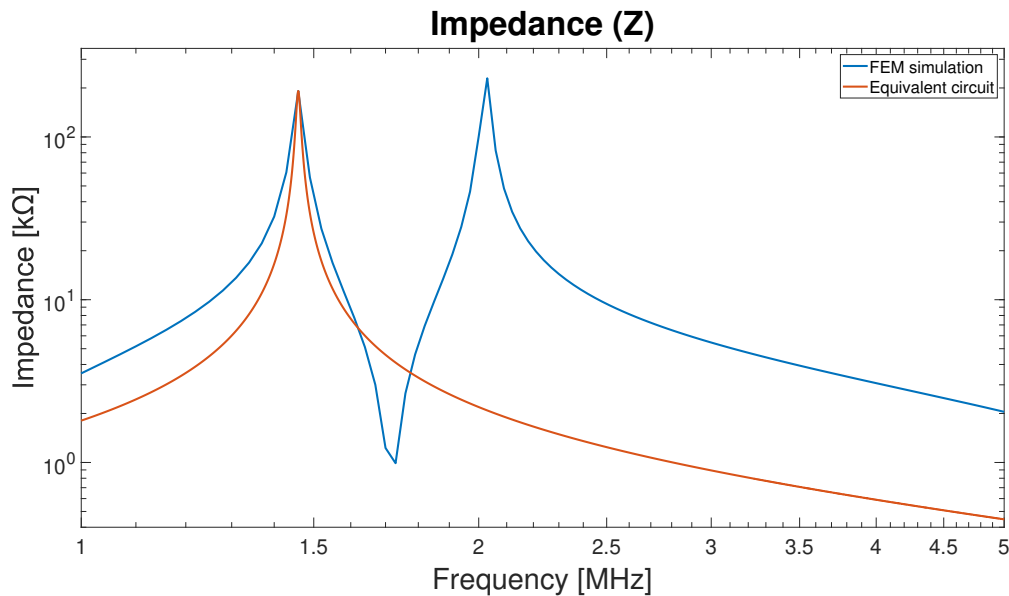


Figure 4.33: Comparison between the FEM simulation bode plot and the bode plot obtained from equation Equation 4.5 for the secondary 50 kW IPT coil

4.8. Voltage across parasitic capacitance and electric field strength evaluation

In order to obtain the voltage across the calculated parasitic capacitances, it was necessary to build the (virtual) equivalent circuit of the overall IPT system. This was done by using *GeckoCircuits*, where the calculated parameters were introduced as inputs in the circuit. It is important to mention that the power electronics side of the system was previously developed by other engineers in the DCE&S group. Besides this, it is worth mentioning that the system was modeled at the standard operation condition,

the values of such condition are shown in Table 4.7 (see Figure 2.14 for nomenclature), while the modeled circuit can be seen in Figure 4.34.

Table 4.7: Main parameters for 50 kW overall IPT circuit model

	Value	Unit
V_{in}	1,348	VDC
V_{out}	1,328	VDC
C_1	21.65	nF
C_2	22.95	nF
R_1	173	m Ω
R_2	163	m Ω

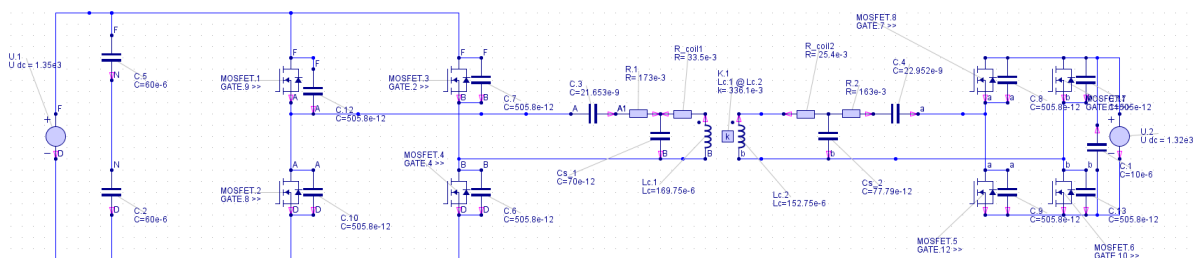


Figure 4.34: Circuit model built at *GeckoCircuits* for the overall 50 kW IPT system

After running the model, the voltage across the parasitic capacitances is obtained, which is 6.453 kV for the parasitic capacitance in the primary coil, and 6.044 kV for the parasitic capacitance in the secondary coil (see Figure 4.36). If this same simulation is run with zero parasitic capacitance, the voltage across the coil terminals results to be 6.502 kV and 6.09 kV for the primary and secondary coils respectively (see Figure 4.35). It can be noticed that the voltage difference between the two scenarios is negligible at standard operation frequency (85 kHz), this, however, might not be the case at higher frequencies when the influence of the capacitor is greater, as can be seen in Figure 4.37, where the electric energy increases as the frequency increases, until the resonance frequency is reached.

Finally, from the Electromagnetic Fields FEM simulation, it is possible to locate where the electric fields are concentrating. Figure 4.38 shows that the main concentration of the electric fields is located (as expected) between the segments of wire with the highest electric potential difference, which are the first and last segments of the coils. Figure 4.39 shows the gradient of electric fields located in the plane between the coil and the terminal, showing that, in fact, the highest electric field is located between the first outer turn and the last segment of the wire. Figure 4.40 and Figure 4.41 show that there is also a concentration of electric fields in the space between the coils and the cores. The electric field magnitude in these regions (and hence the voltage across the parasitic capacitance) is low at the standard operation frequency, with values of around 0.15 kV/mm evaluated at 500 kHz, but, as mentioned before, the voltage and electric field across the parasitic capacitance could increase with the frequency, reaching values of around 14 kV/mm evaluated at 1.46 MHz, for this reason, it is highly recommended not to operate close to the resonance frequency of the coils.

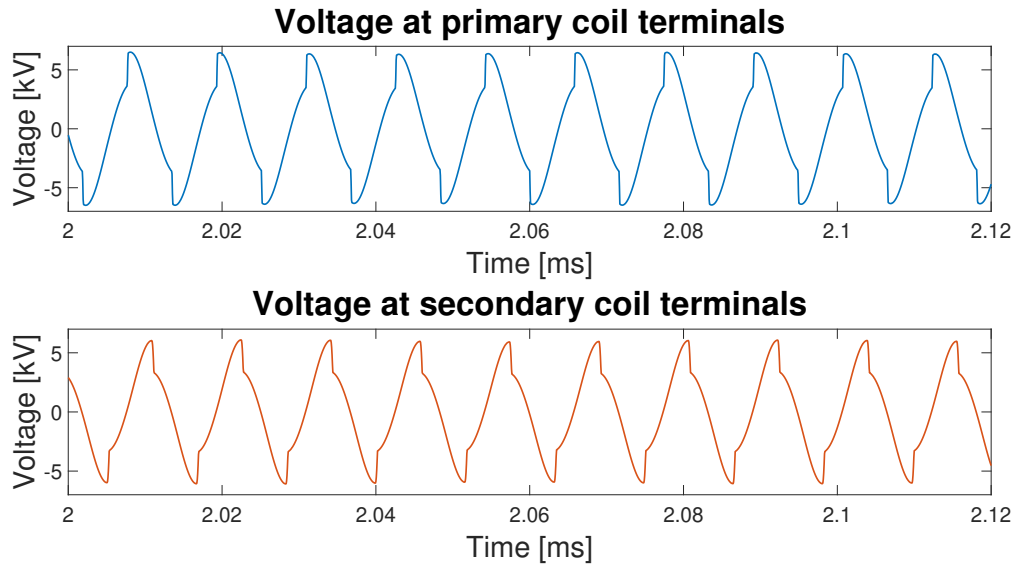


Figure 4.35: Voltage across the coil terminals (without parasitic capacitance) for the 50 kW IPT system

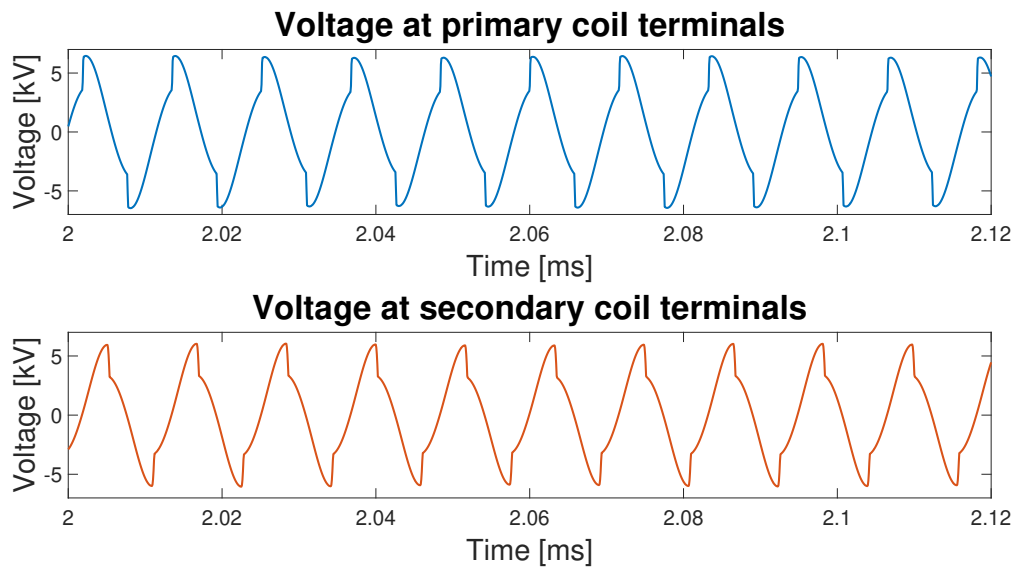


Figure 4.36: Voltage across the coil terminals (with parasitic capacitance) for the 50 kW IPT system

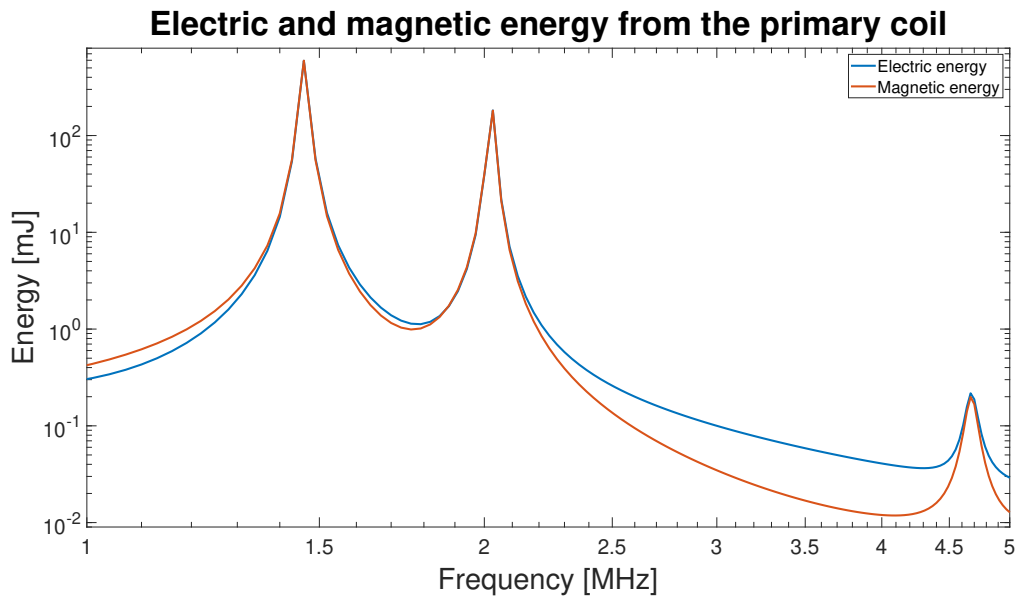


Figure 4.37: Electric and magnetic energy comparison from the primary coil of the 50 kW IPT system, evaluated at 500 kHz

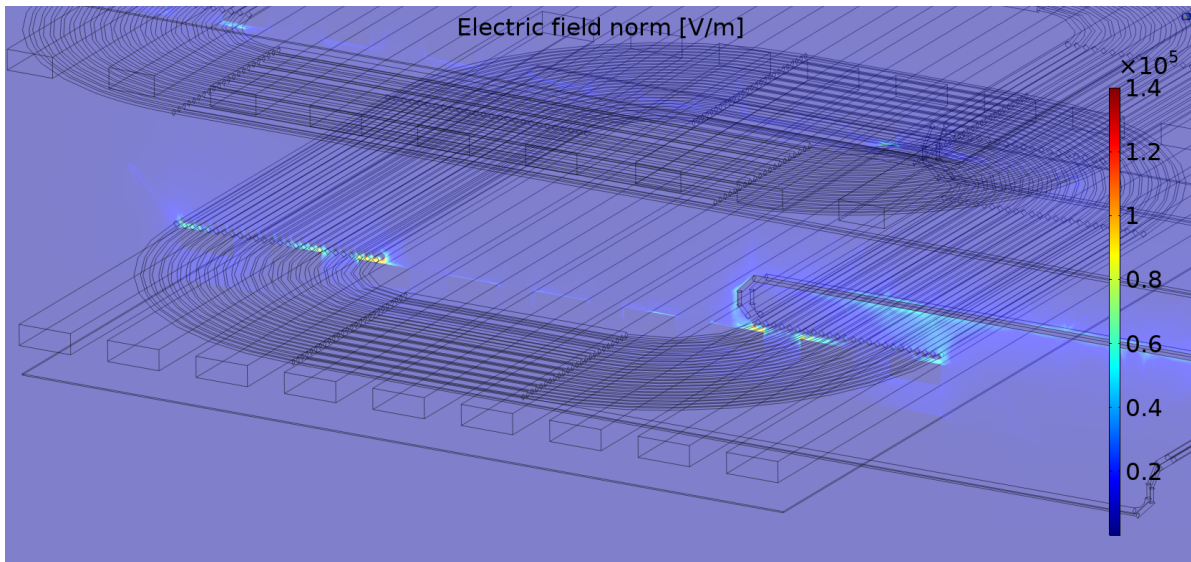


Figure 4.38: Electric field visualization between the coil and the terminal of the 50 kW IPT primary pad, evaluated at 500 kHz

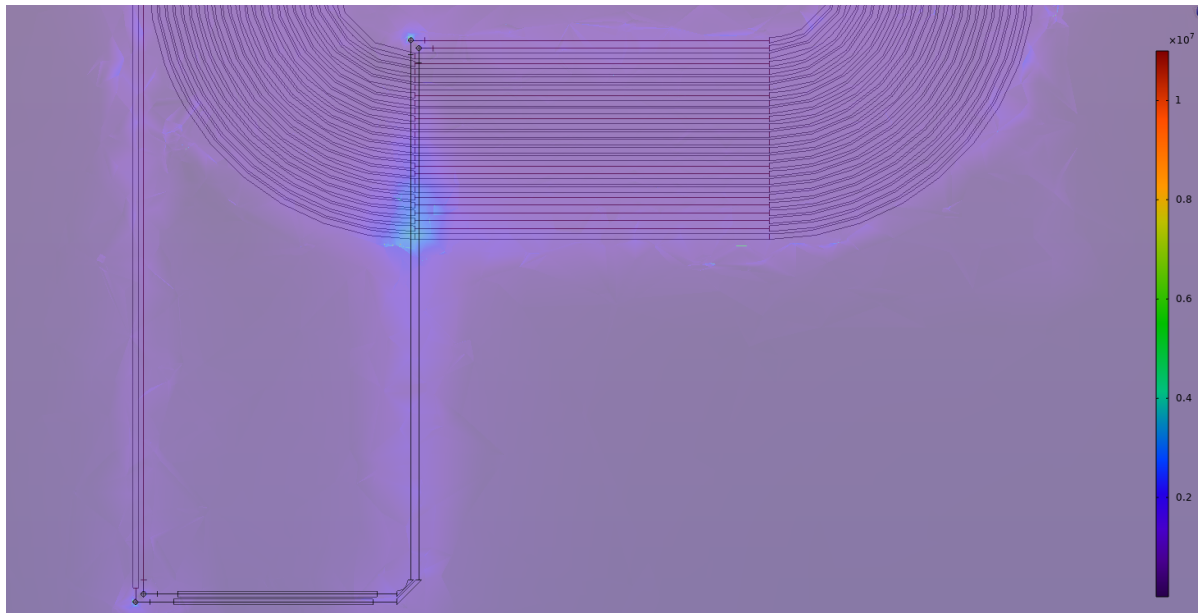


Figure 4.39: Electric field [V/m] visualization in the plane between the coil and the terminal of the 50 kW IPT primary pad, evaluated at the resonance frequency (1.45 MHz)

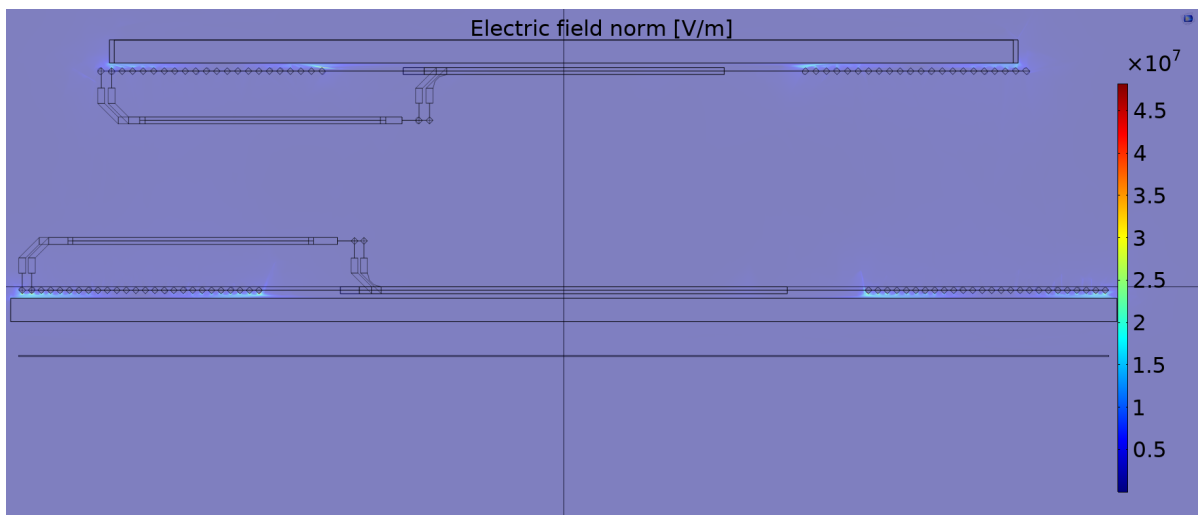


Figure 4.40: Electric field visualization between the coil and the cores of the 50 kW IPT primary pad, evaluated at 500 kHz

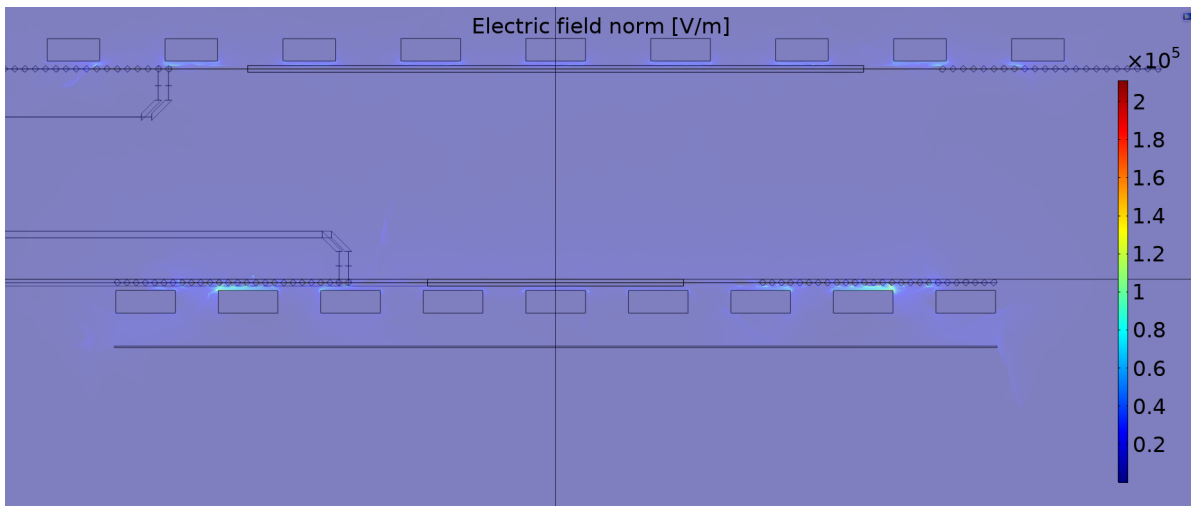


Figure 4.41: Electric field visualization between the coil and the cores of the 50 kW IPT primary pad (transversal view)

5

Conclusions & Future Work

The first purpose of this thesis was to design a proper casing for the charging pads of a 50 kW IPT system that was able to keep the active elements of the pads (coils, ferrite cores, and metal shields) within the dimensions specified by a multi-objective optimization study. To do so, the first step of the design process was to do the CAD model of the active elements of the pads. Once these elements were modeled, a selection process for the cooling system fans was performed. Then, the active elements of the pads and the fans were integrated into a 3D assembly and finally, the CAD design of the casings was done, by taking into account the following design criteria: accurate dimensions, easy and fast to manufacture and assemble, modular-designed, light, adequately cooled, and robust. The final designs can be seen in Figure 5.1 and Figure 5.2.

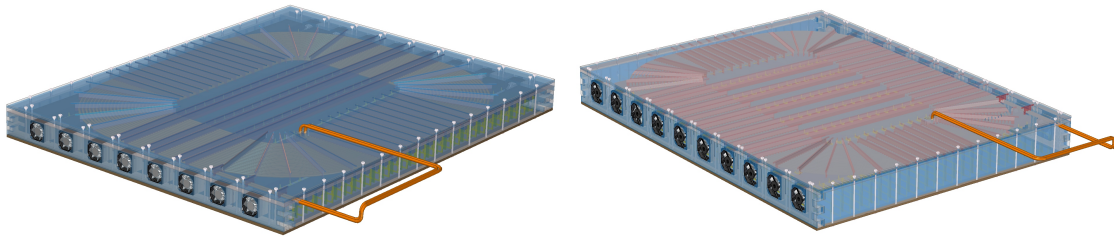


Figure 5.1: Final design of the casing for the primary pad Figure 5.2: Final design of the casing for the secondary pad

The accomplished design of the casing allowed for a smooth manufacturing and assembly process of the real casing, proving that the design met these requirements. Besides this, the casing provided a robust fixture for the active elements and the fans, which means that the coils will perform as predicted by the multi-objective optimization study. Finally, since the casing design was modular, it is possible to disassemble the casing in such a way that the active elements are accessible and prone to changes or upgrades.

The second purpose of this thesis was to evaluate the parasitic capacitance (C_s) of the coils, and understand how this capacitance could affect their electromagnetic behavior. To do so, an electromagnetic fields FEM simulation was performed on the coils. With such simulation, it was possible to determine the magnitude of the parasitic capacitance of each coil. The parasitic capacitance of the primary and secondary coils are 70 pF and 77.79 pF respectively. In order to derive these values, it was also required to derive the resonance frequency of the coils (f_0), their resonance impedance (Z_0), their AC resistance at the resonance frequency (R_{AC}), and their inductance (L). The equivalent circuit of the primary and secondary coils can be seen in Figure 5.3, while the derived values can be seen in Table 5.1. It is important to note as well that this thesis provides the methodology for the setup of a FEM simulation applied to IPT pads, which includes important information such as how to do a correct meshing, and which features to use at *COMSOL*. Still, it is proposed as future work to perform a sensitivity study to comprehend how the mesh size in the elements influences the results, this will allow us to come up with an optimal mesh size with the best balance between the error and the computational time.

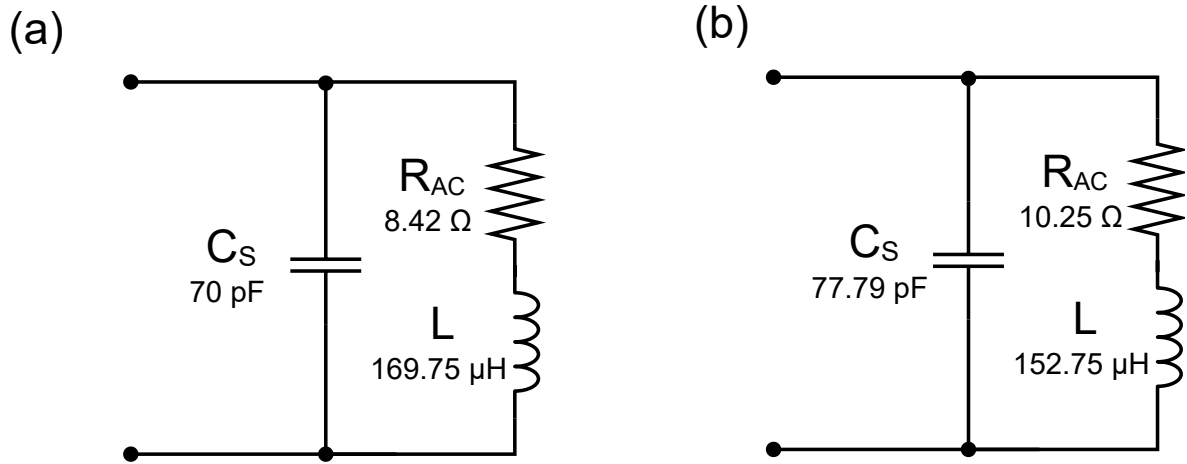


Figure 5.3: (a) Equivalent circuit of the 50 kW IPT primary coil. (b) Equivalent circuit of the 50 kW IPT secondary coil

Table 5.1: Derived values for the primary and secondary coils

	Primary	Secondary
Resonance frequency (f_0)	1.46 MHz	1.46 MHz
Resonance impedance (Z_0)	287.94 k Ω	191.62 k Ω
Coil inductance (L)	169.75 μ H	152.75 μ H
AC resistance (R_{AC})	8.42 Ω	10.25 Ω
Parasitic capacitance (C_S)	70 pF	77.79 pF

From the electromagnetic fields FEM simulation, it was found that electric energy is stored in the electric fields across the parasitic capacitance of the coils. Such parasitic capacitance is mainly concentrated between the first and last segments of the coils, as shown in Figure 5.4, and also between the coils and the ferrite cores, as shown in Figure 5.5. Nonetheless, it was concluded that the electric field across the parasitic capacitance at standard operation frequency (85 kHz) is low, with values of around 0.15 kV/mm, which don't represent a risk of over-voltage. It is still important to know that at higher frequencies (close to the resonance frequency of the coils), the electric field's magnitude increases, reaching values of around 14 kV/mm, which could imply a risk of electric discharge, for this reason, it is recommended to put special attention to the gap between the coil terminals, and the gap between the coil and the ferrite cores, only in the cases where the operating frequency is close to the resonance frequency of the coils, since these are the regions where the electric energy is usually concentrated.

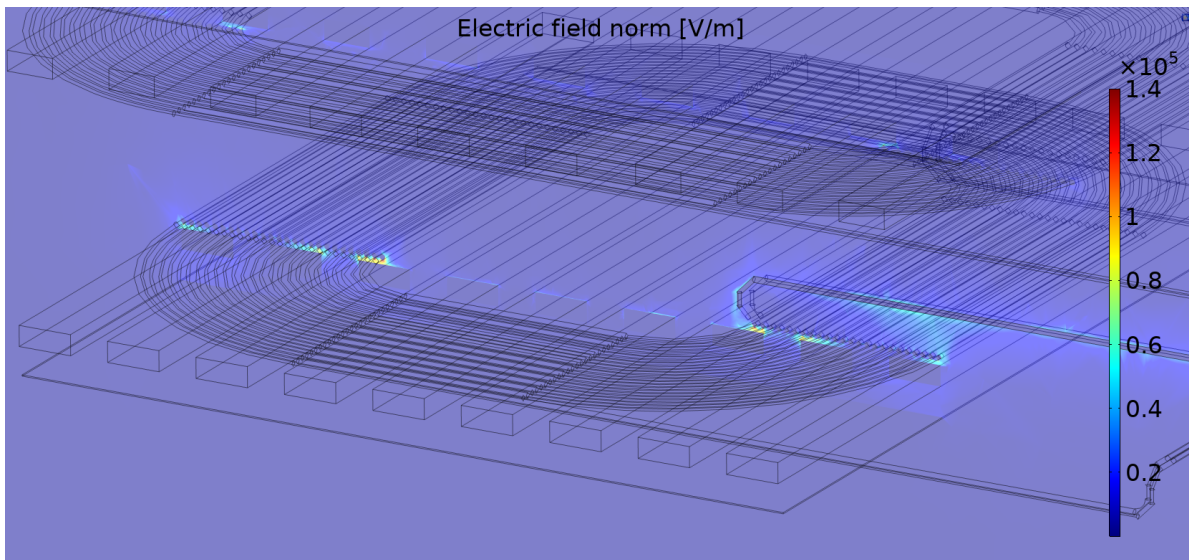


Figure 5.4: Electric field visualization in the terminals of the 50 kW IPT primary pad, evaluated at 500 kHz

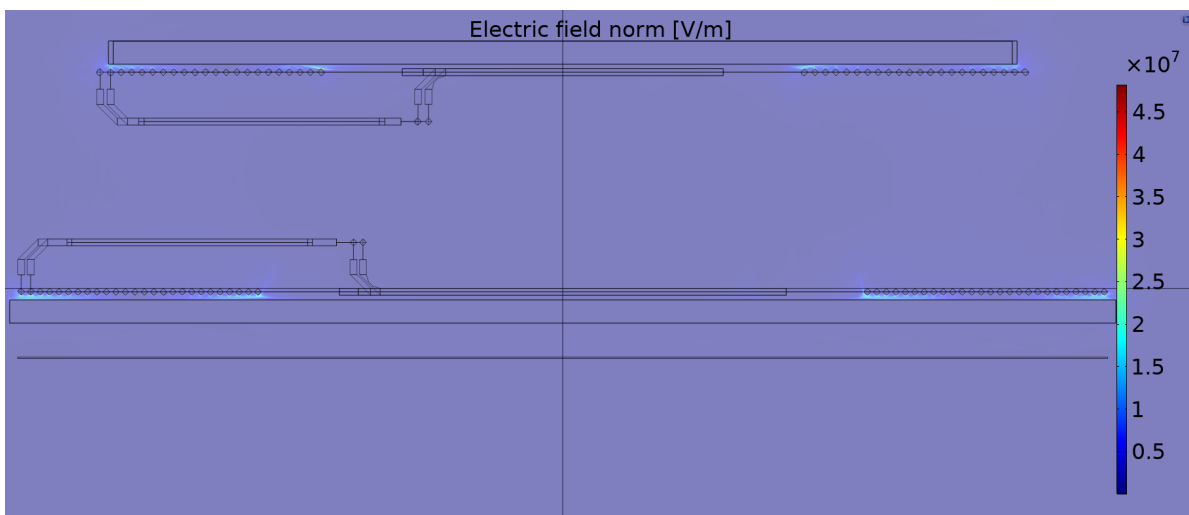


Figure 5.5: Electric field visualization between the coil and the cores of the 50 kW IPT primary pad, evaluated at 500 kHz

It is recommended for future work to improve the FEM simulation setup in order to obtain more accurate values. This can be accomplished in several ways: (1) Model a Litz wire (which is the one used at the real coil) in the FEM simulation setup, instead of modeling a regular copper wire as it was done for this study, (2) Refine the mesh size of the model for a more accurate simulation, and perform a sensitivity study, (3) Assign accurate material properties for the ferrite cores, since the current properties are essentially idealized and finally (4) use the *Infinite Elements* feature in order to emulate an infinite surrounding for the simulation, instead of using an isolated sphere as surrounding as was done for this study.

Bibliography

- [1] S. Bandyopadhyay, P. Venugopal, J. Dong, and P. Bauer, "Comparison of magnetic couplers for ipt-based ev charging using multi-objective optimization," *IEEE Transactions on Vehicular Technology*, vol. 68, no. 6, pp. 5416–5429, 2019.
- [2] C. Baguley, S. Jayasinghe, and U. Madawala, "Theory and control of wireless power transfer systems," in *Control of Power Electronic Converters and Systems*, Elsevier, 2018, pp. 291–307.
- [3] O. H. Stielau and G. A. Covic, "Design of loosely coupled inductive power transfer systems," in *PowerCon 2000. 2000 International Conference on Power System Technology. Proceedings (Cat. No. 00EX409)*, IEEE, vol. 1, 2000, pp. 85–90.
- [4] K. Knaisch, M. Springmann, and P. Gratzfeld, "Comparison of coil topologies for inductive power transfer under the influence of ferrite and aluminum," in *2016 Eleventh International Conference on Ecological Vehicles and Renewable Energies (EVER)*, IEEE, 2016, pp. 1–9.
- [5] R. Bosshard, "Multi-objective optimization of inductive power transfer systems for ev charging," Ph.D. dissertation, ETH Zurich, 2015.
- [6] F. Grazian, P. Van Duijzen, T. B. Soeiro, and P. Bauer, "Advantages and tuning of zero voltage switching in a wireless power transfer system," in *2019 IEEE PELS Workshop on Emerging Technologies: Wireless Power Transfer (WoW)*, IEEE, 2019, pp. 367–372.
- [7] M. Amirpour, S. Kim, M. P. Battley, P. Kelly, S. Bickerton, and G. Covic, "Coupled electromagnetic-thermal analysis of roadway inductive power transfer pads within a model pavement," *Applied Thermal Engineering*, vol. 189, p. 116710, 2021.
- [8] Transfer Multisort Elektronik. "9gv3612g301 sanyo denki." (2022), [Online]. Available: <https://www.tme.eu/es/details/9gv3612g301/ventiladores-de-cc-12v/sanyo-denki/> (visited on 07/07/2022).
- [9] CWC Groups. "Delta auc0512db-af00 50mm pwm fan." (2022), [Online]. Available: <https://store.cwc-group.com/auc0512dbaf00.html> (visited on 07/07/2022).
- [10] Cadence. "How to remove parasitic capacitance in high-speed designs." (2022), [Online]. Available: <https://resources.pcb.cadence.com/blog/2021-how-to-remove-parasitic-capacitance-in-high-speed-designs>.
- [11] I. Lope, C. Carretero, and J. Acero, "First self-resonant frequency of power inductors based on approximated corrected stray capacitances," *IET Power Electronics*, vol. 14, no. 2, pp. 257–267, 2021.
- [12] ElectronX Lab. "Self resonance frequency of an inductor." (2022), [Online]. Available: <https://www.electronx.ca/self-resonance-frequency-inductor/>.
- [13] ElectronX Lab. "Self resonance frequency of an inductor." (2022), [Online]. Available: <https://www.electronx.ca/self-resonance-frequency-inductor/>.
- [14] COMSOL. "Comsol documentation." (2022), [Online]. Available: <chrome-extension:%20/efaidnbmnmnibpcajpcgltclefindmkaj/https://doc.comsol.com/5.4/doc/com.comsol.help.acdc/ACDCModuleUsersGuide.pdf>.
- [15] M. Assad and M. A. Rosen, *Design and Performance Optimization of Renewable Energy Systems*. Academic Press, 2021.
- [16] G. A. Covic and J. T. Boys, "Inductive power transfer," *Proceedings of the IEEE*, vol. 101, no. 6, pp. 1276–1289, 2013.
- [17] G. A. Covic and J. T. Boys, "Modern trends in inductive power transfer for transportation applications," *IEEE Journal of Emerging and Selected topics in power electronics*, vol. 1, no. 1, pp. 28–41, 2013.

- [18] F. Grazian, W. Shi, J. Dong, P. van Duijsen, T. B. Soeiro, and P. Bauer, "Survey on standards and regulations for wireless charging of electric vehicles," in *2019 AEIT International Conference of Electrical and Electronic Technologies for Automotive (AEIT AUTOMOTIVE)*, IEEE, 2019, pp. 1–5.
- [19] W. Shi, J. Dong, T. B. Soeiro, *et al.*, "Design of a highly efficient 20 kw inductive power transfer system with improved misalignment performance," *IEEE Transactions on Transportation Electrification*, 2021.
- [20] T. Diekhans and R. W. De Doncker, "A dual-side controlled inductive power transfer system optimized for large coupling factor variations," in *2014 IEEE Energy Conversion Congress and Exposition (ECCE)*, IEEE, 2014, pp. 652–659.
- [21] SAEJ2954, in *Task Force on Wireless Power Charging*, [Online], Available: <http://www.sae.org>.
- [22] C. R. Sullivan, "Optimal choice for number of strands in a litz-wire transformer winding," *IEEE transactions on power electronics*, vol. 14, no. 2, pp. 283–291, 1999.
- [23] K. Kadem, M. Bensetti, Y. Le Bihan, E. Labouré, and M. Debbou, "Optimal coupler topology for dynamic wireless power transfer for electric vehicle," *Energies*, vol. 14, no. 13, p. 3983, 2021.
- [24] New England Wire Technologies. "Litz wire benefits and applications." (2022), [Online]. Available: <https://www.newenglandwire.com/litz-wire-benefits-and-applications/> (visited on 06/10/2022).
- [25] M. S. Haque, M. Mohammad, J. L. Pries, and S. Choi, "Comparison of 22 khz and 85 khz 50 kw wireless charging system using si and sic switches for electric vehicle," in *2018 IEEE 6th workshop on wide bandgap power devices and applications (WiPDA)*, IEEE, 2018, pp. 192–198.
- [26] Elektrisola. "Efolit taped high frequency litz wires." (2022), [Online]. Available: <https://www.elektrisola.com/en/Products/Litz-Wire/Products/EFOLIT>.
- [27] Ferroxcube. "3c95 3c97." (2022), [Online]. Available: <https://www.ferroxcube.com/en-global/download/download/94>.
- [28] Laserbeest. "Materials." (2022), [Online]. Available: <https://www.laserbeest.nl/materialen/> (visited on 11/07/2022).
- [29] K. Dai, X. Wang, S. Niu, *et al.*, "Simulation and structure optimization of triboelectric nanogenerators considering the effects of parasitic capacitance," *Nano Research*, vol. 10, no. 1, pp. 157–171, 2017.
- [30] Britannica. "Capacitor electronics." (2022), [Online]. Available: <https://www.britannica.com/technology/amplifier>.
- [31] W. Li, "Wireless considerations in ocular implants based on microsystems," in *Handbook of Mems for Wireless and Mobile Applications*, Elsevier, 2013, pp. 424–462.
- [32] J. Mai, Y. Wang, X. Zeng, Y. Yao, K. Wu, and D. Xu, "A multi-segment compensation method for improving power density of long-distance ipt system," *IEEE Transactions on Industrial Electronics*, 2021.
- [33] High Voltage Engineering by MG Niasar. "Impedance measurement in matlab simulink (using impedance measurement block and state-space model)." (2022), [Online]. Available: <https://www.youtube.com/watch?v=Nuxra4UmYzQ>.
- [34] COMSOL Learning Center Resources. "Modeling electromagnetic coils." (2022), [Online]. Available: <https://www.comsol.com/support/learning-center/article/Introduction-to-Modeling-Electromagnetic-Coils-8251/112>.